2-1-2012

Use of expanded polystyrene in developing solid and hollow block masonry units

Youmna Alaa Yahia Ali

The American University in Cairo

School of Sciences and Engineering

Use of Expanded Polystyrene in Developing Solid and Hollow Block Masonry Units

BY

Youmna Alaa Yahia Ali

A thesis submitted in partial fulfillment of the requirements for the degree of

Master of Science in Construction Engineering

Under the Supervision of:

Dr. Ezzat H. Fahmy
Professor and Dean
School of Sciences and Engineering
The American University in Cairo

Dr. Mohamed N. Abou Zeid
Professor and Chair of the Department of Construction and Architecture Engineering
The American University in Cairo

Dr. Mohamed Abdel Mooty
Professor, Department of Construction and Architecture Engineering
The American University in Cairo

Dr. Yousry B. I. Shaheen
Professor, Faculty of Engineering
Menoufia University

Fall 2011

Acknowledgement

In the name of Allah, The Most Gracious and The Most Merciful

I would like to thank my family for their constant and relentless support, especially my father who is always my rock, my mother who is my guiding light and my brother who is also my best friend. I would like to thank all my friends for their constant cheers, especially Hiba, Maha, Marium, Mary, and Soha. I would like to extend my appreciation to all my advisors, especially Dr. Ezzat Fahmy who always supported me and taught me far beyond the written words and numbers of these pages. His advice will always guide me in life and I am really honored of always being his student. I would like also to extend my gratitude to Dr. Abou Zeid, Dr. Abdel Mooty and Dr. Yousry Shaheen for always believing in me and giving me the confidence to conquer and advance.

I would like to extend my gratitude to all the engineers, technicians and workers in the Materials and Structures Laboratories of the American University in Cairo (AUC). I would like also to thank Eng Khaled Fadel and his team in the Work Shop of the Mechanical Engineering Department for assisting me in the alterations to the block moulds. In addition, I would like to express my gratitude to Dr. Salah El Haggar, Chair of the Mechanical Engineering Department for allowing me use all the means in the Environmental Laboratory and I would like to heartily thank Mr. Mohamed Said and Eng Ahmed Saad for their invaluable expertise and help in the procuring and testing of abrasive compounds for the durability test program.

I am heartily thankful to Dr. Emad Ewais, Head of Cermaic Materials Division of the Central Metallurgical Research & Development Institute (CMRDI) for allowing me use his laboratory for conducting the hot wire tests and for giving me his precious knowledge and time in analyzing the results. I also extend my appreciation to Dr Haytham El Gazzar, Science and Technology Research Center (STRC) of AUC, for all his help in facilitating testing at the CRMDI. In addition, I owe my deepest gratitude to Dr. Mohamed El Morsi, Assistant Professor, Mechanical Engineering Department, AUC, for sharing with me his invaluable time and expertise in thermal FE modeling. He taught me how to build and analyze thermal models and for that I will always be indebted to him for granting me such a

powerful tool and I am proud to be his student. I extend my appreciation to Dr. Ahmed Ibrahim, Physics Department, AUC for his guidance in studying heat transfer fundamentals and identifying the thermal problem of the hollow blocks. Finally, I would like to thank Michael Rizk who is a fine engineer, a scientist and a true friend with a diamond heart.

Last but not least, I would like acknowledge that this thesis was supported by award No. UK-C0015 made by King Abdullah University of Science and Technology (KAUST)

Abstract

Light weight mortar of various densities are developed using Expanded polystyrene (EPS) to partially substitute sand. Lightweight mortars are used herein to develop three types of lightweight hollow blocks: 1-plain, 2- steel wire mesh reinforced (ferrocement) and 3- GFRP mesh reinforced (fibro-cement) as well as lightweight solid bricks. The objective of this research is to obtain lightweight masonry units of sufficient mechanical, long-term and thermal characteristics for low-rise building applications in arid environments.

Different tests were conducted to assess the mechanical strength; durability and thermal conductivity. Five mixtures were prepared; four EPS mortar mixes with average density range 1748, 1498, 1258, 988 kg/m^3, depending on the EPS content and a control mortar mix with average density 2118.4 kg/m^3. The mechanical test program included the measurement of the compressive strength of cubes, cylinders, hollow blocks and solid bricks, in addition to the measurement of the static modulus of elasticity, the stress-strain curve, and splitting tensile strength of cylindrical specimens. The durability test program was conducted wholly on hollow blocks and involved 48-hour water absorption test as well as subjecting them to wet-dry cycles of saturated salt solution and of 5% concentration sulfuric acid solution. The thermal conductivity test was conducted with the hot wire method on solid bricks. A finite element numerical model was developed on the GAMBIT-FLUENT package to assess the equivalent thermal conductivity of the plain hollow blocks. The effect of the three mode of heat transfer, namely, conduction, convection and radiation was reported and the interaction between them was analyzed.

The results showed that the addition of EPS aggregates to mortar reduced the density as well as the mechanical properties. For a density range between 2200 and 980 kg/m^3, the compressive strength of the cubes ranged between 32.6 and 3.5 MPa, and the net compressive strength of the hollow blocks ranged between 9.5 and 2.4 MPa. For the same density range the modulus of elasticity and the split tensile ranged between 15.5 and 1.2 GPa, and 2.87 and 0.55 MPa respectively. The presence of EPS in the cement matrix tremendously improved the failure pattern of all the EPS mixes. On the other hand, the durability cycles proved that EPS hollow blocks were resilient to acid and salt exposure. The weight loss and compressive

strength loss of the hollow blocks due to ettringite leach decreased significantly with the addition of EPS aggregates. The salt wet-dry cycles adversely affected the compressive strength plain, ferrocement and GFRP mesh reinforced hollow blocks. The plain hollow blocks suffered from efflorescence and salt crystallization that adversely affected the compressive strength. Moreover, the compressive strength of the GFRP mesh reinforced hollow blocks was the most affected and the ferrocement EPS hollow blocks were less affected. Furthermore, the thermal conductivity tests showed that the inclusion of EPS aggregates decreased the thermal conductivity of mortar remarkably. The average thermal conductivity of the control bricks was 1.8 W/m. K. and ranged between 1.53 and 0.16 W/m. K. for the EPS mortar bricks. However, the thermal conductivity obtained numerically for the hollow blocks considering all heat transfer modes was 1.43 W/m. K. for the control blocks and ranged between 1.27 and 0.25 W/m. K. for the densest and lightest EPS mortar hollow blocks respectively. The equivalent thermal conductivity determined from the thermal model suggested that lighter EPS hollow blocks of density range 1258 and 988 kg/m^3 would be more thermally efficient if they were solid. This is because, thermal conductivity of the hollow blocks inflated when the radiation heat transfer mode was accounted for.

Finally, the results show that EPS mortar hollow blocks and bricks are suitable for non-load bearing application of exterior walls within the limits presented by ASTM C 129 and the Egyptian Standards (EOS 2005/42 2005), maintain their integrity while resisting salts and acids and have superior thermal insulation.

Table of Contents

List of Figures

List of Tables

Nomenclature

F_c:	Compressive strength in (MPa)
E:	Static modulus of elasticity (GPa)
F_{st}:	Split tensile strength in (MPa)
EPS_c :	EPS aggregate content (kg)
e:	Surface emissivity constant at 0.94
g:	Gravitational acceleration constant 9.81 m/s^2
H:	Height of the cavity in the gravitational direction (m)
Ks:	Thermal conductivity of solids (W/m K)
K_{cond}:	Thermal conductivity due to pure conduction phase (W/m K)
K_{conv}:	Thermal conductivity due to pure convection phase (W/m K)
K_{rad}:	Thermal conductivity due to pure radiation phase (W/m K)
K_{tot}:	Thermal conductivity due to the interaction of the three heat transfer phases (W/m K)
$K_{cond-conv}$:	Thermal conductivity due to the interaction between the conduction and convection phases (W/m K)
Nu_x:	Dimensionless Nusselt's number in the 2-D boundary conditions
$\overline{Nu}$:	Mean dimensionless Nusselt's number in the 3-D boundary conditions
P:	Pressure of air inside the cavity (Pa)
Pr:	Dimensionless Pandtl's number constant at 0.7
Q:	Heat flux (W/m^2)
q:	Heat transfer rate (W)
$q_{r,k}$:	Net radiative heat flux at surface k
Ra:	Rayleigh number
T:	Temperature in (K)
T_c , T_h:	Cold and hot temperature respectively in (K)

u: Velocity component in the x-direction (m/s)

v: Velocity component in the y-direction (m/s)

w: Velocity component in the z-direction (m/s)

x, y, z: Coordinates (m)

Greek Symbols

α: Thermal diffusivity (m^2/s)

β: Coefficient of volume expansion of air constant at 0.003356 (K^{-1})

ρ: Density (kg/m^3)

ρ_c: Reference density of air—at an iteration incident (kg/m^3)

σ: Stephan-Boltzmann constant (W/m^2K^4)

ν: Kinematic viscosity of air (m^2/s)

Chapter 1

Introduction

1.1 Introduction

Masonry units are used as load bearing or non load bearing building envelopes and interior partition walls. There are several materials, shapes and sizes of masonry units worldwide. The American Concrete Institute's 530.1 Report (ACI 530.1R) defined four prevalent types of masonry units: 1) concrete masonry units (CMU), 2) clay or shale masonry units, 3) stone masonry units and 4) hollow glass masonry units. Similar types of masonry units are prevailing in the Egyptian market. This research focuses on CMU types and its applications.

CMU are made from cement and fine and coarse aggregates. There are two types of CMU as depicted by ACI 530.1 R, Type I entails concrete masonry units that are moisture controlled and Type II entails concrete masonry units that are not moisture controlled and is divided into three types according to the weight of the units: lightweight, medium, and normal CMU. Two types of CMU are available in the market namely; solid concrete brick and hollow concrete blocks. The standard specifications of the two types are stated by ASTM C 55, ASTM C 129 and ASTM C 90. The standard mechanical testing methods and absorption limits for CMU are provided by ASTM C 140, 1552 and 1314. The Egyptian Standards state the CMU dimensions, density and strength used in Egypt. The density is categorized into light, medium and dense CMU. Also the CMU are divided by the Egyptian code into load-bearing and non-load bearing according to the compressive strength (EOS 2005/42 2005).

In the past, CMU was used to be cast in moulds like normal concrete which necessitated good workability of the mix and possessed limited production rate. However, with the advances in technology and increasing demand, vibro-compaction mechanization that involved instantaneous de-moulding and stocking became the conventional method in CMU production (Gunduz, 2008; Dawood and Ramli, 2010; www.cement.org). There are several attractions to the use of CMU in construction. The main attraction of concrete masonry units lies in the convenience of the availability of its materials and the method of production. The availability of the components of CMU means that it does not require special orders, minimizes delays and out of stock instances (www.cement.org). Masonry construction is

predominantly a labor intensive job; it requires only experienced masons and trowels (Mosalam, 2009, USACERL, 1997, www.cement.org). The construction of masonry walls do not require sophisticated methods of construction and design and most of the adopted methods for existing structures were based on empirical data extracted from years of practice and testing (Mosalam et al, 2009; ACI 530.1R). Additionally, the presence of holes in hollow block concrete units renders them as very versatile construction elements. The holes allow for using thermal insulation inserts and acoustic isolation fibres (Van Green, 1986). Also, hollow block concrete units have better thermal performance than solid concrete bricks (Albikary, 2003; www.cement.org) as the thermal conductivity of solid concrete is much higher than that of air. To overcome this drawback in using solid concrete brick units, introducing air gaps is recommended to reduce its thermal conductivity drastically (Al-Jabri, 2005).

Although CMU have many advantages, challenges called for the improvement of CMU manufacturing materials. The average range of the weight of concrete hollow block is between 18 and 22 kg, which cripples both masons physically and affects their production rate and continuation in this industry (USACERL, 1997). Also, the efficient thermal performance of concrete hollow blocks is highly affected by thermal bridges due to the presence of ribs and joints (Al-Jabri et al, 2005). These challenges gave way to the production of lightweight aggregate (LWA) and more thermal efficient materials in production of concrete hollow blocks and solid bricks units. The most commercially available LWA concrete hollow blocks, yet still researched worldwide, is made with light weight expanded clay aggregates (LECA) which is also mentioned in the Egyptian code though it is unavailable now in the Egyptian markets (www.cement.org; www.cellularconcreteinc.com; Albikary, 2003; Khatib, 2006; Gunduz, 2006).

The utilization of lightweight aggregates (LWA) in CMU is a research topic till today in terms of mix design, mechanical properties, and thermal characteristics. Some researchers reported that the addition of LWA proportion equivalent to 1/3 of the volume of concrete decreased the strength of the mortar by ½ (Chandra and Berntsson, 2002). This is why the mix design of LWA CMU always involves the addition of mineral admixtures such as fly ash and silica fume (Chandra and Berntsson, 2002; Khatib, 2006; Gunduz, 2008). The thermal conductivity of LWA CMU was also an investigation topic by some researchers. However, most of the studies involved assessing the thermal performance of sampled materials from the

LWA CMU rather than estimating the thermal conductivity or the U-value of the whole hollow block or assembly of blocks respectively. With the availability of modern simulation techniques using finite element modeling, the thermal conductivity and thermal transmittance of LWA concrete hollow blocks and assemblies could be accurately estimated.

With today's environmental awareness, the urge to recycle more wastes and reduce the carbon foot print of the construction industry became a call everywhere in the world. Wastes are available worldwide, unlike manufactured and natural LWA that require certain technologies and geography respectively. Wastes are available almost for free, as it usually gains some value after being introduced as usable material, and recycling wastes in a recycling scheme such as mixing it with cement or replacing the natural aggregates will save the environment and result in a more economic construction. It is worth noting that most of the processed LWA such as expanded slag, fly ash and LECA are made from recycled wastes. However, virgin wastes do not always possess the qualities for producing LWA concretes. These facts have channeled most of the new research in LWA to investigate the use of wastes such as expanded polystyrene waste (EPS), rubber tires, glass and wood chippings (Khatib, 2006). As the compressive strength of recycled aggregates concrete decreased rapidly with the type and percentage of the utilized waste material, the use of some of the produced LWA mixtures may be limited to specific construction applications.

Expanded Polystyrene (EPS) are light closed cell microstructures made of discrete air voids dispersed in a polymer matrix (Kan and Demirboga, 2009; Chen and Liu, 2004). The density of EPS ranges between 10 and 50 kg/m^3(Kan and Demirboga, 2009; Chen and Liu, 2004). Recycling the unmodified EPS wastes (crushed EPS wastes) as lightweight aggregates in concrete is considered the cheapest and most environmentally rewarding methods as compared to the other recycling methods proposed by Kan and Demirboga, 2009. Expanded Polystyrene (EPS) concrete is one of the lightweight aggregate concretes that has proven its high thermal insulation and acoustic insulation properties (Perry et al, 1991). There are different attractions of EPS concrete, among which, the easiness of its production, availability and cost effectiveness (Godwin, 1982; Gaggino, 2006). The easiness of EPS concrete mixing and the aggregate's availability and economy made it a more attractive material to be used in housing applications. EPS concrete's superior thermal and acoustic insulation as well as its lightweight made it attractive for non-structural building applications such as: 1-thermally

insulating wall and roof panels (Perry et al, 1991), 2-core materials for sandwich panels (Perry et al, 1991) and lightweight thermally insulating blocks (Godwin, 1982; Perry et al, 1991; Al-Jabri et al, 2005; Gaggino, 2006).

Hollow blocks and solid bricks made of EPS mortar are applications of the use of recycled LWA in manufacturing masonry units. EPS masonry units (EPS MU) could be utilized for construction of above ground exterior walls as well as interior walls. Due to the constituents of the mortar matrix, EPS MU are expected to possess superior thermal characteristics. For structures that require high strength and ductility, the EPS hollow block load bearing walls would have reinforcement and suitably grouted to increase their compressive strength and toughness (USACERL, 1997). As grouting would jeopardize the thermal insulation of the blocks, lightweight grout could be used to prevent the formation of thermal bridging. EPS MU are expected to be cost efficient. The materials required to produce EPS MU are off the shelf and cheap. Cost reductions would also be projected on the construction industry as light weight EPS MU would reduce the dead load on the foundations and other structural elements. Additionally, the less bulky structural elements would further reduce the cost of foundations. In addition, the nature of EPS MU would reduce the necessity of implementing expensive thermal insulation materials on external walls (Al-Jabri et al, 2005). Furthermore, EPS mortars are proven to have good quality in terms of water absorption, chloride ion penetration and sulphur attack (Ravindrarajah and Tuck, 1994; Babu and Babu, 2003).

1.2 Work Objectives and Scope

The main objective of this research is to investigate the use of expanded polystyrene (EPS) in producing lightweight mortar solid brick and hollow block units that have superior thermal insulation relative to the existing masonry units in the Egyptian market. A parallel objective is to examine the confinement effect of ferrocement technology and polypropylene fiber wrap on EPS mortar hollow blocks. The following masonry units are produced and tested in the present research to realize these objectives:

1. Plain EPS mortar hollow blocks with no reinforcement or polypropylene fibers.
2. Ferrocement EPS mortar hollow blocks in which the block were reinforced with welded wire mesh or fiberglass wire mesh.

3. Polypropylene Wrap EPS mortar hollow blocks in which polypropylene fibers were added to mortar mix.
4. Plain Solid EPS concrete bricks

The hollow blocks have dimensions of 400x200x 200mm and have two cylindrical holes each of 125mm in diameter. The plain solid bricks are of size 245x110x65 mm. The EPS hollow blocks and solid bricks have dense, medium and light densities according to the amount of EPS used in the block production.

The research parameters are:

1. The EPS content in mortar is varied to produce EPS mortars with different density
2. The reinforcement type is varied in the EPS mortar hollow blocks; plain (no reinforcement), steel wire mesh reinforced, GFRP mesh reinforced

During this research several tests and examinations are performed as follows:

1. The mechanical properties of cubic and cylindrical specimens made of several EPS mortar mixes are determined
2. For each of the tested mixes solid bricks, ferrocement EPS mortar hollow blocks, polypropylene wrap EPS mortar hollow blocks and plain EPS mortar hollow blocks are produced
3. The mechanical and thermal properties of solid EPS mortar bricks are determined
4. The mechanical properties of the three types of EPS mortar hollow blocks are determined
5. The durability aspects of the three types of EPS mortar hollow blocks are determined
6. A finite element model is constructed to estimate the thermal conductivity of EPS mortar hollow blocks.

The outcome of the mechanical and physical tests is be reported. The effect of the inclusion of EPS mortars on the mechanical and thermal properties of mortar will be reported and analyzed. Also the failure pattern of EPS mortars will be cross-compared according to the changing parameters.

The mechanical properties of the three types of EPS mortars hollow blocks is cross compared with the mechanical properties of cubic and cylindrical specimens. More importantly, the effect of ferrocement and polypropylene wrap confinement will be assessed in terms of the

effect on compressive strength, failure pattern and durability aspects. The behavior of the proposed ferrocement and fiber wrap EPS mortar hollow blocks and solid EPS mortar bricks will be interpolated based on the mechanical, physical and failure pattern of EPS mortar, CMU, ferrocement and encased ferrocement CMU under compression highlighted in literature.

1.3 Thesis Organization

This Thesis is composed of six chapters. In addition to this Chapter, the introduction, the remaining five Chapters are organized as follows:

Chapter 2: Introduces a review of the available literature. It intertwines the different subjects discussed in this thesis. It explains in details the mechanical characteristics of EPS mortar and the parameters affecting its strength and ductility. It also presents the work of previous researchers on EPS hollow blocks and bricks. In addition, the confining effect of ferrocement will be addressed. References that studied the durability of mortars generally and EPS mortar specifically will be also discussed. Finally, studies done on the thermal characteristics of EPS mortar and thermal numerical modeling are furnished in details.

Chapter 3: Contains the details of the experimental program carried out to fulfill the objectives of this thesis. Mixture proportions and design of EPS mortar used in the experimental program are reported. A discussion of the sample size and number of mechanical tests applied on EPS mortar specimens, hollow blocks and bricks is presented as well. In addition, descriptions of the durability and thermal tests are included.

Chapter 4: Presents an analysis and discussion of the test results. Effects of different test parameters on the behavior of the test specimens are investigated in the light of available previous research.

Chapter 5: Presents the numerical model for calculating the equivalent thermal conductivity of the developed EPS hollow block units and elaborates on the analytical results of this model.

Chapter 6: Summarizes the study, followed by the main conclusions drawn from experimental and analytical investigations. Furthermore, recommendations for future study are suggested.

Chapter 2

Literature Review

2.1 Introduction

The presented literature review in this chapter covers the research areas related to the objective of this thesis. The current thesis research focuses on the use of expanded polystyrene for production of lightweight mortar and manufacturing thermally efficient lightweight hollow blocks and bricks. Lightweight mortar and concrete has attracted engineers and environmentalists. The mechanical properties of several types of lightweight mortar and concrete were the subject of investigation by some researchers. However, very little information is available in the literature on its use for the production of a final building element. As the ferrocement concept was utilized in the production of the hollow blocks proposed in this thesis, this chapter will also the cover the related ferrocement research. The proper explanation of the mechanical, physical, and thermal behavior of such complex building element requires crossing several references. The main topics addressed in this chapter are mechanical properties of EPS cement composites, ferrocement confining behavior under compression, previous research related to EPS blocks and bricks, physical properties of cement composites and EPS mortar subjected to aggressive environments, thermal properties of cement and EPS mortar, and equivalent thermal conductivity of blocks through thermal numerical modeling.

2.2 EPS Cement Composites

2.2.1 Mechanical characteristics

The primary attractions of EPS cement composites are their lightness and energy absorption. Despite their low-strength, EPS cement composites proved versatile enough to attract more researchers to launch a full-scale study of the rest of its mechanical and physical properties. This section recites the attempts researchers spent trying to explore and engineer the mechanical, physical, durability, and thermal characteristics of EPS mortar and concrete.

Perry et al. 1991 experimentally studied the mix preparation and mechanical behavior of three EPS mortar mixes. They reported mixtures in which replacement of 40, 50 and 60 per

cent by volume of the mortar mix by beaded EPS. The reported mixes had 1.2, 1 and 0.8 specific gravities. In the reported mixes, the cement-to-sand ratio was unity, water-cement ratio (w/cm) ranged between 0.35 and 0.45 and fine sand of maximum size of 1.2 mm was used. the volume of sand ranged from 350 kg/m^3 for the lightest mix and 550 kg/m^3 for the densest one. The diameter of the EPS balls ranged from 2.5 mm to 5.5 mm with a mean diameter of 3.8 mm and ball density of 20 kg/m^3. The strength of EPS mortar was controlled by varying the mix proportions. They reported the compressive strength, stress-strain curves and proposed a modification to Pauw's equation for the calculation of the static modulus of elasticity, E. They mixed EPS mortar by mixing sand and cement first then adding water with super plasticizer if needed. After sufficient mixing of the mortar, EPS beads were added and mixed thoroughly. They also reported that hand tamping rather than vibration to avoid segregation. Despite using superplasticizer, poor workability and surface finish were observed in their work. They tested cylinders of 100 mm diameter and 200 mm height to obtain the compressive strength and stress-strain curves. The obtained compressive strength ranged between 4 and 12 MPa for corresponding air-dried densities 850 and 1250.kg/m^3. They concluded that the relationship between compressive strength and density of EPS mortar was approximately linear. The plotted stress-strain relationship showed that EPS mortars have a maximum strain at maximum stress equal to 2000 microstrains which is similar to that of conventional concrete but at much lower maximum stress. However, EPS mortars exhibited a more-or-less linear stress-strain behavior which was attributed to the nature of internal micro-cracking of lightweight concrete that allowed it to exhibit higher strains capacity at maximum stresses. The transition towards linear stress-strain behavior increased with the increase in the EPS content. They measured the secant static modulus and proposed the following formulae to predict E for the proposed density range:

$$E = 0.07\rho^{1.53} f_c^{0.25}$$

$$E = 5.1\rho^{0.835} f_c^{0.5}$$

Where, E is the static modulus of elasticity in MPa, ρ is the air-dried density in kg/m^3 and f_c is the compressive strength in MPa of 100 x 200 mm cylinders.

Ravindrarajah and Truck 1994 performed experimental investigations on the mechanical and physical properties of EPS mortar and concrete made with treated EPS beads. They presented in this research the only available discussion about chemical resistance of EPS mortar and concrete. The mix design was formed of Portland cement (PC), silica fume (SF), 10 mm coarse aggregates and commercially available EPS spherical beads that are coated with a hydrophilic coat. Their work covered two research topics, EPS mortar and EPS concrete keeping a constant nominal density of EPS cement composite at 1350 kg/m^3 and a constant cement content of 400 kg/m^3. In the first topic, they varied water cement ratio between 0.35 and 0.45 while in the second one they introduced coarse aggregates, substituted a constant 10 per cent of PC with SF and kept w-cm ratio constant at 0.4. The EPS bead content was targeted to occupy 40 per cent of the cement composite. 90 per cent of the EPS spherical beads had a maximum diameter of 2.36 mm and particle density was 67 kg/m^3. They adopted mixing technique similar to the one adopted by Perryet al. 1991. For compressive strength, they tested cylindrical specimens of dimension 100 mm diameter and 200 mm height as well as 100 mm cubes. For tensile strength the tested cylinders of the same size as those tested for compression. 150 mm diameter and 300 mm height cylinders were used to determine the static modulus of elasticity testing. Also 100x100x380 mm prisms were tested to determine pulse velocity and shrinkage. They reported that despite their precautions, the EPS cement composite mixes were dry and lumpy, full compaction was impossible and maximum air content mounted to 13.1 %. However, segregation was not seen in slices they prepared to examine visually and beads were uniformly distributed. They also reported that the compressive strength increased from 5.6 to 11.9 MPa when w/c ratio decreased from 0.6 to 0.35. They noted that the ratio between the 7-day and 28-day compressive strength of EPS cement composited decreased with the increase in w/c ratio and that all mixes showed a continuous increase in compressive strength gaining between 28 and 90 days. They found that indirect tensile strength of EPS cement composites ranged between 13.6% and 15.3% of its the compressive strength and it exhibited a decreasing trend with the increase in w/c ratio. They proposed a modified equation for the determination of E and stated that it increased with the decrease in w/c ratio where w/c of 0.35 produced E of 11.9 GPa.

$$E = 1.146\ \rho^{1.1} F_c^{0.5}$$

Where E is the modulus of elasticity in MPa of 150 x 300 mm cylinders, ρ is the dry density in kg/m^3; F_c is the compressive strength in MPa of 100 x 200 mm cylinders. They reported that the EPS concrete specimens exhibited relatively higher shrinkage due to the lack of restrain EPS have on the surrounding matrix.

Babu and Babu 2003 studied the strength and durability of EPS concrete and mortars using silica fume (SF) as partial replacement of Portland cement (PC) in a study that aimed at developing structural EPS concrete of minimum compressive strength of 17 MPa and density range of 1450 to 1850 kg/m^3. Ten mix designs were obtained by varying the percentage of PC replacement with SF, types of sand and coarse aggregates, volume and bead size of EPS. Three percentages of SF were used; 3%, 5% and 9%, two types of sands were varied; finer than 2.36 mm and finer than 1.18 mm, and two sizes of coarse aggregates were varied; 10 mm and 16 mm. Finally two sizes of EPS beads were used, 6.3 mm and 4.75 mm. The total volume of cementitious materials varied between 360.5 and 659.45 kg/m^3 and w/c ratio varied between 0.44 and 0.273. Compressive strength tests were performed on 100mm cubes at 1, 3, 7, 28 and 90 days, also absorption test was performed on the same specimens after 90-days. Split tensile tests were performed on 100x200mm cylinders. EPS mortars and concrete showed very good workability and finishing which was attributed by the authors to the combination of SF, sufficient volume of cementitous, materials and super plasticizers.

They reported that the compressive strength development of EPS cement composites increased with the increase in the percentage of SF and strength gain after 90 days was negligible. The 7-day compressive strength was 75%, 85% and 90% of the 28-day compressive strength for 3%, 5% and 9% SF respectively. Also, they found that the compressive strength of EPS concrete increased linearly with the density increase and EPS volume decrease. They reported also that the strength of EPS concretes made with small sized beads was higher than the ones made with a combination of the two bead sizes for the same mix proportions. They also reported that for similar mix proportions and densities, EPS mortars yielded similar compressive strength to EPS concretes made with 10 mm coarse aggregates.

For relevance, only the EPS mortar mixes will be discussed. The three EPS mortar mixes had fresh density of 1503 kg/m^3, 1748 kg/m^3 and 1546 kg/m^3, with corresponding compressive strength 10.2MPa, 18.5 MPa and 15 MPa, and corresponding tensile strength of 2.10 MPa,

2.20 MPa and 2.15 MPa, and corresponding water absorption percentage of 4.596%, 3.140% and 2.570. The strongest mixes achieved compressive strengths of 16.2 and 20.8 MPa. They attributed the relatively low strength of the mixes to the zero strength of the EPS aggregates. They studied the failure mechanism of EPS concretes under compressive load and reported it to be gradual and that specimens retained load even after failure without disintegration. They attributed this near ductile behavior to the high energy absorption characteristics of EPS concrete and mortar. The split tensile strength was 1.53MPa and 2.32 MPa for wet densities 1552 kg/m^3 and 1873 kg/m^3. They found that the split tensile strength increased with the increase in the compressive strength and formulated an empirical equation that relates between the two mechanical properties in the form:

$$F_{st} = 0.88\ \mathbf{log}\ (F_c) - 0.37$$

Where, F_{st} is the split tensile strength and F_c is the compressive strength all in MPa. The split tensile failure mechanism of EPS concrete was very different from that exhibited by conventional concrete.

Laukaitis, et al. 2005 studied the mechanical characteristics of crumbled, and large and small spherical EPS aggregates included in aerated cement matrix. By far this is one of the very few research done on the utilization of irregularly shaped EPS wastes as lightweight aggregates. However, this research covers only very light EPS cement composites of density below 350 kg/m^3. The mix design constituted of cement, surfactant (foaming agent), and EPS aggregates. The sieve analysis of large spherical EPS aggregates revealed 43.93% of size 10.2mm and 55.92% of size 5mm, the rest are of sizes 2.5mm and below. The size distribution of the small spherical EPS aggregates was: 1.45%, 60.89%, 37.62 % of respective sizes 10.2mm, 5mm, 2.5mm and the rest are below 2.5mm. The sieve distribution of the crumbles particles was 1.02%, 28.27%, 63.85% and 6.86% for sizes 10.2mm, 5mm, 2.5mm, and smaller than 2.5mm. Three ratios of foam cement to EPS aggregates were studied, namely, 1:1, 1:2 and 1:3. The tested specimens were 100mm and 400mm cubes. The compression tests revealed that the compressive strength of EPS cement composites depended on its density and the EPS granular shape. They found that EPS foam cement made with fine EPS spheres had 40% higher compressive strength than when made with large spheres and 68% higher than when made with crumbles. They correlated the decrease of the

compressive strength to the shape of matrix extracted from the ESM photographs. The lowest compressive strength achieved for crumbles EPS cement was 0.2 MPa at a density of 220 kg/m^3 and the highest was 0.55 MPa at a density of 300 kg/m^3 (these values are approximate as they were extracted from a plot presented in that publication). They presented three equations, one for each EPS granular shape, to predict the compressive strength of EPS foam for different light densities:

Fine spherical EPS: $F_c = 0.0298\ \rho^{0.0101X}$

Large spherical EPS: $F_c = 0.0744\ \rho^{0.0084X}$

Crumbled EPS: $F_c = 0.0104\ \rho^{0.0132X}$

Where, F_c is the compressive strength in MPa and ρ is the density in kg/m^3. Also the researchers measured the modulus of elasticity (E) and found that EPS foam cement made with EPS crumbles had the lowest values. The values of E obtained for crumbled EPS foam cement ranged between 150 MPa and 300 MPa for corresponding densities 250 kg/m^3 and 300 kg/m^3. The authors used electronic scanning microscope (ESM) to help study the interfacial zone between the foam cement matrix and the EPS aggregates. The ESM revealed that the cement matrix of EPS cement made with large spherical granules took the shape of small honeycomb cavities separated from each other by thin film or pellicles. The surface of the matrix of crumbled EPS cement revealed a more complex and irregular shape of honeycombs that are connected together by thin damaged pellicles. Fine granules gave the cement matrix the shape of very regular arrays of bubbles without any cavities or pellicles. After compressive tests, they analyzed the failure planes based on the ESM photographs and fount that after crushing, foam cement made with large EPS spheres; the granules which are covered with thin film of cement broke apart but were not pulled out of the matrix. Crumbled EPS cement showed that when crushed, the EPS crumbles break apart but remain intact within the matrix which indicated very good cohesion. Fine EPS cement showed insufficient cohesion when crushed and EPS granules pulled out of the binder leaving shell shapes.

Babu et al 2006 experimentally investigated the effect of EPS particle size on the strength and moisture migration of EPS concrete. In this study they used two types of polystyrene aggregates; expanded EPS and unexpanded UEPS and used two types of pozzolanic

materials; fly ash (FA) and silica fume (SF). The experimental program investigated a range of densities between 1000 and 1900 kg/m^{3}plus control specimens made of normal weight concrete (NWC). All the EPS concrete and mortar specimens contained a constant cementitoius ratio of 563 kg/m^3, 30% of which is formed of fly ash, and constant w/c ratio of 0.35. In addition, one UEPS series of specimens were designed with 35 % FA substituting PC and another with 10% SF substituting PC. Sand finer than 2.36mm and coarse aggregates finer than 8mm were used. Two sized of spherical EPS aggregates were used; 1.18mm and 6.3mm with particle density of 23.6 kg/m^3 and 9 kg/m^3 respectively. One size of UEPS aggregates was used which was 1.18mm to with a particle density of 66.5 kg/m^3. The compressive strength tests were performed on 100 mm cubes at 1, 3, 7, 28 and 90 days. The absorption test was performed on the same specimens after 90-days and the split tensile on 100x200mm cylinders. The absorption test specimens were prepared as in Babu and Babu 2003 and moisture migration was measured through an indigenous test set up of the author's design. The results of moisture migration and absorption tests were cross—compared. The significance of this research is that it compiled the various experimental data extracted from different sources and formulated two general equations, one that relates compressive strength to EPS concrete and mortar density and the second relates the spit tensile strength of EPS concrete and mortar to the compressive strength.

They reported that the compressive strength of all EPS mortar and concrete specimens increased with the decrease in EPS size and noted that this observation was more prominent in less dense mixes. They also reported that the compressive strength gain in EPS concrete and mortar made with FA continued till the 90th day. The 90-day compressive strength exceeded the 28-one by a range of 27% to 14% for the corresponding range of densities of 1050 kg/m^3 to 1820 kg/m^3 and the range of compressive strength increase fell down to 9% to 5% for the same corresponding densities when smaller EPS aggregates were used. When compared the compressive strength of specimens made with the more rigid UEPS, they found that the latter yielded 70% higher compressive strength and attributed this finding to the higher density of UEPS aggregates than that of EPS.

On the other hand, the failure of EPS was gradual and specimens retained load after peak stress without disintegrating, unlike its UEPS concrete counterparts which exhibited brittle failure similar to that of NWC. The failure of EPS concrete specimens was in a shearing off

manner (spalling) and EPS aggregates were seen bonded firmly to the concrete matrix even after failure, unlike UEPS which got de-bonded from the matrix.

They proposed the following general equation based on their work and the work of several researchers that related the compressive strength (F_c in MPa) to the density (ρ in kg/m^3) of fresh EPS concrete and mortar:

$$F_c = 10.3\ \rho^{1.918}\ 10^{-6}$$

A similar equation was also proposed to relate the compressive (F_c in MPa) and split tensile strengths (F_{st} in MPa) of EPS concrete and mortar:

$$F_{st} = 0.2416\ F_c^{0.7933}$$

This equation was developed based on the EPS concrete and mortar empirical data which showed that the split tensile strength increases with the increase in the corresponding compressive strength. They noted that the split tensile strength increased with decreasing the aggregate size of EPS concrete. They reported that EPS concrete split tensile failure was gradual failure and specimens did not split into two halves. The most ductile failure noted was for EPS concretes with EPS volume range between 35 and 50%. The maximum compressive strength achieved by EPS concrete was 20 MPa and its UEPS counterpart was 35 MPa.

Bouvard, et al. 2007 experimentally investigated and numerically modeled mechanical characteristics of high performance cement mixed with millimeter sized EPS spheres. They mixed high performance cement of compressive strength around 150 MPa with different sizes and ratios of EPS spheres. Two types of distribution of EPS spheres were used; one-size and two-size distribution (bimodal). The monosize distribution had a diameter range between 0.75mm and 1.1mm. The bimodal distribution had 30% of its volume consisting of diameter range between 0.75mm and 1.1mm and 70% of diameter range between 1.5mm and 2.6mm. Eight mixes with a density range between 432 kg/m^3 and 961 kg/m^3 that corresponded to cement volume ratio of 0.204 and 0.415 were achieved by changing the EPS content. The mechanical properties and micro structural observation by means of 3D imaging were performed on 4cm cubes. The 3D imaging enabled the identification of different phases in the composite. The extracted images were reconstructed and a series of radii and centers were

obtained to depict numerically the distribution of EPS spheres in the cement matrix. The 3-D images were used to build a model that depicts the microstructure of EPS cements. Based on the radii and centers of the EPS spheres, a tessellation of polyhedral convex cells was produced in space. Each edge of the polyhedral represented a beam structure made of the cement matrix. The finite element analysis of this 3-D model allowed the authors to determine the stress-strain behavior of the composite under simple compression at the microstructure level. They tested the numerical model and agreed reasonably with the experimental results.

The authors reported the compressive strength and plotted the stress-strain curves of the different EPS cement mixes. The maximum compressive strength was 11.4 MPa and correlated with the highest density while the minimum compressive strength was 0.03 MPa and correlated with the lowest density. They reported that the compressive strength of EPS cement could be readily modeled by Gibson and Ashby's model, which assumes a power relationship between the strength and density. They concluded that the relative density of the conductive phase—the cement matrix density—was responsible for the thermal conductivity and strength results. In addition, they indicated that the size and distribution of EPS particles in the cement matrix tremendously alters the thermal and mechanical results. Therefore, they suggested that further 3-D analysis should be adopted to engineer and optimize the properties of EPS cement composites.

2.2.2 Improved failure characteristics of EPS cement composites

Many researchers have identified the ductile failure of EPS mortar and concrete. However, few went into details of quantifying this phenomenon through identifying its affecting parameters. Two characteristic phenomena of EPS mortars will be discussed in this section, namely, the particle size effect and specimen size effect on nominal compressive strength.

Miled, et al. 2007 investigated experimentally and numerically the effect of EPS particle size on the compressive strength of high performance EPS mortars of different densities. They also analyzed the EPS mortar failure mode at different EPS volume fraction (macro porosity). They investigated five EPS mortar mixes with different macro porosity and a control mix. The set EPS volume fractions were 0%, 10%, 20%, 30%,40% and 50% which corresponded

to densities 2289.1kg/m^3 (control matrix), 2000 kg/m^3, 1800 kg/m^3, 1600 kg/m^3, 1400 kg/m^3 and 1200 kg/m^3. The volume fraction of EPS mix was calculated following this formula:

$$p = \frac{\rho_{matrix} - \rho_{concrete}}{\rho_{matrix} - \rho_{EPS}}$$

Where, p is the macro porosity, ρ_{matrix} , $\rho_{concrete}$ and ρ_{EPS} are densities of the control mix, the EPS mortar mix and the EPS beads respectively. The cement content ranged from 961.9 to 500.22 kg/m^3, the w/c and SF ratios were kept constant at 0.26 and 0.3 respectively. Three sizes of spherical EPS beads were tested, namely, 1mm, 2.5 mm and 6.3 mm. They tested fifteen mixes; five different porosities for each bead size. The experimental program comprised the evaluation of static modulus of elasticity and compressive strength. The modulus of elasticity was tested on 110x220mm cylinders. Two different cylindrical mould sizes were used for testing the compressive strength, 110x220mm and 44x88mm, in order to assess whether the particle size effect associated with EPS mortars is independent from specimen size effect.

They reported that the elastic modulus of elasticity was independent from any particle size effect and depended only on the macro porosity of EPS mortar mix. They also noted that a near linear decrease in E was associated with the increase in the macro porosity of EPS mortar mix. The obtained results from the compressive strength test confirmed the influence of particle size effect on the compressive strength of EPS mortar mix. For example for EPS mortar mix of macro porosity 0.24, the mixes made with 1mm beads yielded 60% higher compressive strength than the ones made with 6.3 mm beads and mixes made with 2.5 mm were 30% stronger than the ones made with 6.3 mm beads. They also reported that the particle size effect vanished at higher macro porosities (p>0.5).

In addition, they associated the failure mode of EPS mortar to its macro porosity. Low porosity EPS mortars exhibited a quasi-brittle failure mode characterized by longitudinal and localized splitting macro cracks that existed around the EPS beads zones. On the other hand, EPS mortars with high porosities exhibited a ductile failure mode characterized by dispersed micro cracks all over the mortar matrix around EPS beads. In addition, EPS mortars specimens of higher porosity were able to retain load without full disintegration. In attempt to

generate a numerical model that relates compressive strength to particle size and macro porosity, the authors divided the failure pattern of EPS mortars into two phases. The first phase depends only on the macro porosity of the mix and this phase is the elastic region, since E is independent of the particle size effect. The second phase is characterized by the evolution of cracks from micro-cracks to macro-cracks and is dependent on both the macro porosity and the particle size based on the analysis of failure mode. They proposed a numerical model that predicted the normalized EPS mortar compressive strength based on its macro porosity and EPS bead size. The particle size effect is a power law, and the numerically obtained results agreed well with experimental findings.

Haidar and Pijaudier-Cabot 2002 varied the inclusion volume of EPS aggregates in mortar mixes in order to model the porosity effect on the mechanical and fracture characteristics of leached mortars subjected to acidic hazards. They followed the experimental procedures proposed in Bazant's size effect theory to assess whether the nominal strength of EPS mortars, i.e. porous mortars, is influenced by the size of tested specimens (structural size effect). The size effect theory assumes that quasi-brittle materials, such as concrete, abridge two fracture mechanics theories, namely, the plastic limit and linear elastic fracture mechanics. The former assumes that the nominal compressive strength of a material is not affected by the specimen's size while the latter assumes that a crack grows when the stress near the crack tip is more than the fracture toughness of the material (theory of elasticity). Because, the fracture process zone in concrete contains diffused cracks that coalesce and grow before reaching the nominal strength of concrete, the size effect theory presents the most suitable description of its failure and strength. It merely bridges the material strength and linear elastic fracture mechanics to capture the influence of the specimen's size on its nominal compressive strength.

The size effect theory is studied by the authors by plotting the nominal compressive strength of different specimens of similar geometry but different sizes. The results are compared against the two extreme theories, as presented in Figure 2.1. When the plotted results approach the constant limit on the left, this means that the size effect does not apply to the material. On the other hand, when the results approach the descending line on the right imply that the material follows the linear elastic fracture mechanics and that the structure's size affects the nominal strength.

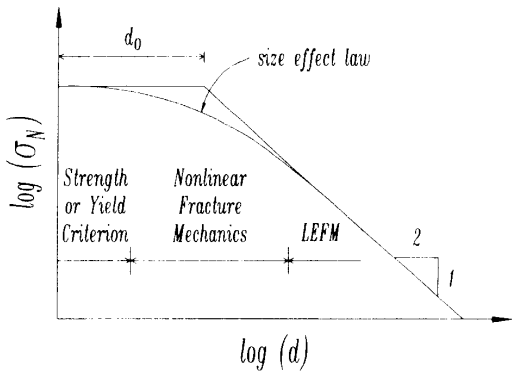

Figure 2.1: The size effect law basic plot is used to assess whether the nominal strength of the material is influenced by the size of the tested specimens (Bazant, et al. 1994)

The authors studied four different EPS mortars of densities 2000, 1800, 1600 and 1400 kg/m^3 with corresponding EPS volume inclusion of 13%, 22 %, 31%, and 39% in addition to a control mix. The EPS beads of size range 3 to 7mm and sand with 20mm particle size were used in a mix designed with constant OPC to sand and w/c ratios of 0.46 and 0.4 respectively. OPC content ranged between 640 and 389 kg/m^3 for the control and lightest EPS mortar mix respectively. The compressive strength was tested on cylindrical specimens of diameter 110mm and height 220mm, the size effect was tested on four notched beams that were geometrically similar but varied size wise. The beams had four depths (D) of 40, 80, 160 and 320mm, a constant width of 40mm, a constant length to depth and span to depth ratios of 8:3 and 2.5 respectively. One notch of width 1.5mm and depth of D/6 was positioned on all four beams.

It was found that the compressive strength and modulus of elasticity decreased significantly with the increase in the inclusion volume of EPS beads. The maximum obtained compressive strength and E were 36.8 MPa and 25.9 GPa for a density of 2000 kg/m^3, while the lowest values were 16.1 MPa and 14 GPa for a density of 1400 kg/m^3. They reported that with reference to the control cylinders, the compressive strength decreased by 40, 54, 61 and 72 % and E decreased by 22, 31, 49 and 58 % for corresponding EPS mortar mixes of corresponding densities 2000, 1800, 1600 and 1400 kg/m^3. The size effect tests revealed that the EPS mortar became more ductile with the increase in EPS volume inclusion. The plot proposed by Bazant, et al.1994 was regenerated for the control mix and the lightest EPS mortar mix (Figure 2.2). The authors pointed out that the strength of the EPS mortar beams

tended to fall more near the strength criterion, which was evidence of the increased ductility of lighter EPS mortars of the size effect. On the other hand, the control specimens followed clearly the size effect law.

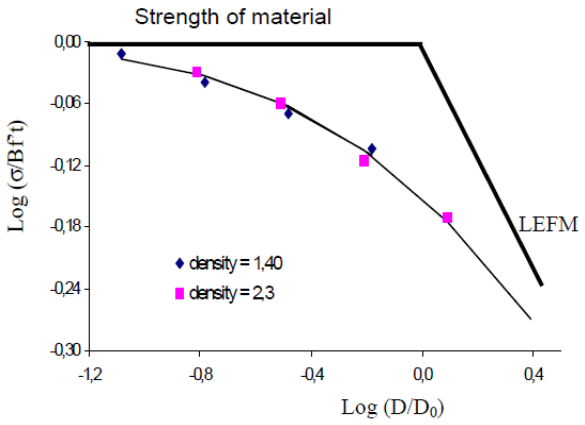

Figure 2.2: The regeneration of the size effect plot using the nominal strength obtained from the four control beams and their counterparts made with lightest EPS mortar (Haidar and Pijaudier-Cabot 2002)

Moreover, the authors used acoustic emission to evaluate fracture localization in the control and EPS mortar specimens after failure. They found that the width of the fracture process zone, where the initiation and diffusion of micro-cracks in concrete occur before coalescing into macro cracks, increased with the decrease in the density of EPS mortars. This implies that the localization of failure diminishes with the decrease in the density of EPS mortars.

2.2.3 Fiber reinforced EPS cement composite

The properties of plain EPS mortars and concretes attracted many researchers especially because of its higher toughness. Comparatively, fiber reinforced mortars and concretes are known for their higher toughness and improved failure mechanism. Some researchers combined fibers with EPS mortar composites in attempt to examine the interaction between the crack diffusion offered by EPS inclusion in the matrix and crack bridging offered by the reinforcing the matrix with fibers.

Chen and Liu 2004 studied the inclusion of steel fibers in EPS concrete mixes made with silica fume and partial substitution of coarse and fine aggregates with two sizes of EPS beads, super plasticizer was used to improve workability. Two series of mixes were developed, each

contained six different EPS volumes and a control mix, the first series was made with OPC and the second one had 10% of OPC substituted by SF. The cementitious material and the steel fibers volumes were kept at a constant volume of 472 and 70 kg/m^3 respectively, and the w/c ratio was 0.37. The fineness modulus of sand and the maximum coarse aggregate size was 2.85 and 20mm respectively, the steel fibers were 25mm long with aspect ratio equal to 60 and the two EPS bead sizes used were 3mm and 8mm. The compressive strength, split tensile strength and shrinkage tests were performed on a density range of EPS concrete mixes between 800 and 1800 kg/m^3 in addition to the control mixes. The compressive strength of 100mm size cubes were tested at 3, 7, 14, 28 and 60 days. The split tensile was tested on 100 mm cubes as well and the shrinkage specimens had dimensions 100x100x515mm and were tested at 3, 7, 14, 28 and 60 days.

The authors found that the compressive strength of specimens made with SF showed more development at early age. For example, they reported that the ratios of the 7-day compressive strength to the 28-day compressive strength ranged from 70 to 75% and 85 to 90 % for EPS concretes made with OPC and 10% substitution by SF respectively. They also found that the compressive strength increased linearly with the increase in the EPS concrete density, the compressive strength of the control mix was 59.2 MPa at a density of 2435 kg/m^3. They reported that at a density equivalent to 75%, 55%, and 35% of that of the control's EPS concretes exhibited 35%, 30% and 20% of the control's compressive strength respectively. The compressive strength of EPS concretes ranged between 10 and 25 MPa.

In addition, the failure mode was gradual and specimens retained load without full disintegration. They reported that SF increased the compressive strength of EPS concretes by 15% and attributed this increase to the influence of SF on dispersing the EPS beads equally in the matrix and improving the interfacial bond between the EPS and the cement matrix. However, they reported that this strength increase is lowered to 8% at higher EPS volumes (55%) and advised the utilization of additional bonding agents at lower EPS concrete densities. On the other hand, the steel fibers improved tremendously the split tensile strength of EPS concrete, and the combination of SF and steel fibers increased its split tensile strength by up to 25%. In addition, the split tensile failure of the EPS concrete specimens made with steel fibers was gradual. Since that EPS aggregates provide negligible hindrance to concrete shrinkage, the increase in the volume of EPS in concrete increased the shrinkage of the

matrix. The authors reported that the when the volume content of EPS was 55%, the 90-day shrinkage strains were 1121 micro strains, which is a disadvantage. On the other hand, they found that steel fiber reinforced EPS concrete with EPS volume 55% showed 90-day shrinkage strains equivalent to 610 micro strains. Therefore, the effect of steel fibers on the properties of EPS concretes was prominent in increasing the split tensile strength, improving the tensile failure mechanism, and resisting the surface straining due to shrinkage.

Trussoni 2009 investigated the fracture properties of fiber reinforced and plain concrete lightened by the partial replacement of coarse and fine aggregates with EPS beads in his Ph.D. dissertation. He used the two fracture tests, namely, three point bending (TPB) and the wedge splitting (WS) tests. He discussed the test results using the ANOVA analysis to assess the effect of EPS partial replacement on fiber reinforced and plain concretes. He analyzed the parameters of fracture mechanics and presented further illustrative evidence on the improved ductile failure of EPS concretes and to prove that EPS absolutely alters that fracture behavior of concrete when it is used as replacement to fine aggregates.

The test program commenced with trial batches of EPS concrete (EPSC) were first designed to achieve a target wet unit weight of 1880 Kg/m^3 and a target compressive strength of above 20.7 MPa. The EPS beads were 1mm in diameter and w/c ratio was more or less 0.5. the normal weight concrete (NWC) mix ingredients were OPC, water, sand, coarse aggregates that constituted a corresponding volumes of 14% (317.5 kg), 21.5% (154.2 kg), 39.5% (725.7 kg), and 25% (453.6 kg). Two sizes of coarse aggregates varied in the EPSC and NWC, 19 mm and 10 mm. Fibers were introduced at 0.3% of the volume of batches. EPSC was made by replacing 33% of sand by 1mm EPS beads, which produced an overall volume inclusion of 13%. The test program included 12 batches, 3 NWC batches made with 19 mm coarse aggregates; one batch was plain, the second was polypropylene fiber PPF reinforced and the third was steel fiber SF reinforced. The same arrangement was repeated for 10 mm coarse aggregates. The 6 batches made for the NWC was repeated for EPSC to produce 6 EPSC batches. The compressive strength test was conducted on 100 mm cylinders and cubes at 28-day maturity, and the fracture tests were conducted on notched 100x100x425mm beams. For the fracture tests, the author estimated the critical stress intensity factor K_{IC} and the fracture energy G_f. The K_{IC} is a parameter that defines the stress intensity around the crack tip at the initiation of its extension and G_f determines the energy absorbed by the

material when the crack is extending. Also the characteristic length (l_C) was estimated which is a parameter that defines the fracture process zone FPZ the region in front of the crack tip in which the fracture energy is absorbed.

The author found that the addition of EPS decreased the static modulus of elasticity by 38% for mixes made with 10 mm coarse aggregates and 44% for ones made with 19 mm coarse aggregates. In addition, the inclusion of EPS decreased the compressive strength by 56% for mixes made with 10 mm coarse aggregates and 55% for ones made with 19 mm coarse aggregates. On the other hand, he reported that EPSC exhibited a more ductile failure through the load-deflection curves. A long period of non-linear behavior was noticed before reaching the peak load for EPSC made with 10mm aggregates and a long period yielding plateau was noticed at the peak load of EPSC made with 19 mm aggregates. In addition, the author found that the specific fracture energy G_f and the characteristic length increased by a respective 13% and 44% than that obtained by NWC. He reported that, the (l_C) of EPSC was 37.4% and 25.4% higher than that of NWC for mixes made with 10 mm and 19 mm aggregates respectively. A larger (l_C) signified a more ductile failure. When the volume FPZ is large, stresses are redistributed and fracture becomes gradual. Large FPZ allow the formation of micro-cracks that coalesce into macro-cracks through a mechanism of releasing the stored elastic energy and conducting stresses to other regions. This mechanism is known as strain softening which is characterized by the controlled dissipated of energy in the matrix resulting in a ductile failure.

Although it was expected that the lower peak load of EPSC would reflect in a lower G_f and l_C, as expected, it was reflected on the results of K_{IC} of EPSC were 48.2% and 34.3% lower than that of NWC for mixes made with 10 mm and 19 mm aggregates respectively. On the other hand, the author reported that generally the inclusion of SF and PPF reduced the ultimate load carried by NWC and EPSC and increased the load-retaining capacity past the initiation of cracks. This too was reflected on K_{IC} of EPSC which was 44.8% and 45.6% lower than that of PPF reinforced NWC for mixes made with 10 mm and 19 mm aggregates respectively. Also the values of G_f were lower by 12.5% and 20.8% from that of PPF reinforced NWC for mixes made with 10 mm and 19 mm aggregates respectively. The l_C was reduced by 24.7% and 26.8% from that of PPF reinforced NWC for mixes made with 10 mm and 19 mm aggregates respectively. For the SF reinforced EPSC, K_{IC} obtained were 52.7%

and 31.6% lower than that of SF reinforced NWC for mixes made with 10 mm and 19 mm aggregates respectively. Also the values of G_f were lower by20% and 20.9% from that of SF reinforced NWC for mixes made with 10 mm and 19 mm aggregates respectively. The l_C was reduced by 20.9% for mixes made with 10 mm and increased by 5.9% for mixes made with 19 mm aggregates when compared to their respective SF reinforced NWC.

The author found that the analysis of the load vs. deflection curves for SF reinforced EPSC displayed that the SF and EPS work together in two different mechanism to enhance the fracture behavior. The first mechanism was induced by the EPS aggregates that increased the volume FPZ and the second mechanism was transferring stress through crack bridging induced by SF. It is worth noting that the FPZ volume increase was also evident in the load deflection curves measured by Trussoni 2009, which indicate a smooth transition between the peak load and the post-peak strain softening behavior. The largest l_C was 570.6 mm which belonged to SF reinforced EPSC made with 19 mm aggregates. The author also reported that SF reinforced EPSC had the highest average (l_C). On the other hand, PPF reinforced EPSC produced the lowest l_C made with 19 mm aggregates (296 mm). The author concluded that the inclusion of EPS (without fibers) in concrete increased the FPZ, which resulted in a rather plastic and gradual failure as compared to the brittle and sudden failure of NWC. In addition, the inclusion of SF and EPS in concrete has a dual mechanism of strain softening and crack bridging. The inclusion of PPF in EPS concretes increased the load-retaining capacity after crack initiation.

2.3 Thermal Properties

2.3.1 Experimental investigation of thermal conductivity of EPS cement composites

Accurate estimation of the thermal mass of building envelopes is essential for the calculation cooling and heating loads. The most widely implemented building envelope units are hollow blocks and bricks because of their availability and low-cost. The research conducted on estimating the thermal characteristics of EPS mortars and concrete is scarce and undedicated. Research and analysis on the thermal conductivity (k-value) is very insufficient. However, this section provides the research done that contained thermal analysis of EPS cement composites.

Bonacina, et al. 2003 conducted one of the very rare studies on the heat transfer properties of EPS mortar. This research experimentally measured and analytically discussed the effect of moisture content on the thermal transmissivity (the total k-value) of autoclaved and EPS mortars. However, its significance lies in the fact that it is one of the few studies that analyzed the heat transfer in porous materials due to the three modes; conduction, convection and radiation. EPS is essentially formed of 98% gas entrapped in thin shells of polystyrene while concrete is 100% solid. The microstructure of EPS cement composites could be simulated by conductive concrete shell surrounding gaseous cavities. Heat transfer in such a structure occurs by conduction in solids and gases, convection in the gaseous volumes and radiation between the interfacial zones of concrete and EPS. The evaluation, interaction, and simulation of these three modes were studied by the authors in the presence of moisture inside the pores of the composites. They formulated a mathematical model to predict the total transmissivity by ignoring the convection and accounting for the other two heat transfer modes. The total thermal transmissivity is the summation of the transmissivity due to conduction (conduction k-value) in mortar and EPS and transmissivity due to radiation (radiation k-value) at the EPS-mortar interface.

The authors formulated a set of mathematical equations that solves for the total transmissivity then validated the mathematical model experimentally. They measured the total k-value of autoclaved and EPS concrete with respective densities 477 kg/m^3 and 458 kg/m^3 with the heat flow meter method. They conditioned the 100 mm test samples at 20 degrees Celsius at three different relative humidities; 35%, 50% and 80%. Then the k-value was measured at temperature difference between the hot and cold surface of 5, 10 and 20 degrees Celsius. They found that the transmissivity due to radiation in autoclaved and EPS concretes contribute to only little percentage and that their mathematical model agrees with the experimental results with a margin of error of 0.5%. The total transmissivity varied with temperature gradient as well with relative humidity. The model evaluated the total k-value of EPS and autoclaved concretes at different moisture content. They concluded that their model could be a very good tool in estimating the total k-value of porous materials without the need to experimental measurements.

Laukaitis, et al. 2005 performed thermal conductivity tests, in addition to their experimental program discussed earlier in section 2.2.1. The thermal conductivity test was conducted with

the heat flow meter method on a specimen size of 305x305mm and thickness range 30 to 80 mm. The thermal conductivity ranged from 0.1 W/mK to 0.045 W/mK for corresponding densities 150 kg/m^3 and 350 kg/m^3 (these values were extracted from the presented graph in this paper). They found that the k-value was more affected by the density of the composite than by the shape of EPS granules. However, for the same density, composites made with EPS crumbled granules revealed the lowest k-value. The thermal conductivity ranged from 0.1 W/mK to 0.045 W/mK for corresponding densities 150 kg/m^3 and 350 kg/m^3 (these values were extracted from the presented graph in this paper). The authors presented three equations that correlate the thermal conductivity to the composite's density; an equation is dedicated for each EPS granular shape.

Fine spherical EPS: $K = 0.0002\rho + 0.0363$

Large spherical EPS: $K = 0.000284\rho + 0.0243$

Crumbled EPS: $K = 0.000168\rho + 0.035$

Where, K is the k-value in W/m. K and ρ is the density in kg/m^3.

Bouvard, et al. 2007 experimentally investigated and mathematically modeled the thermal characteristics of high performance cement mixed with millimeter sized EPS spheres in the same study too (section 2.2.1). The thermal properties were measured using the hot wire method and specimen size was 4x4x16cm. The thermal conductivity of EPS cement mixes were found to increase with the increasing the density of the composites. The k-value ranged between 0.13 and 0.314 W/mK. The authors fitted the experimental thermal results against several models and found that the best model to predict the k-value is Differential Effective Medium (DEM) known as asymmetric Bruggemann's estimation. This model assumes that the cement matrix remains connected no matter how much is the EPS volume fraction and is solved iteratively to obtain the effective thermal conductivity that is a function of the k-value of EPS and cement matrix as well as their corresponding volume fraction.

2.3.2 EPS concrete blocks and bricks strength and thermal insulation

Godwin, 1982, announced the release of the first load bearing, thermally insulating building bricks made with expanded polystyrene concrete after 12 years of research. The 100 mm EPS concrete bricks were economic and were primarily proposed to function in load-bearing wall

panels intended to be built in poor areas in cement producing countries. He proposed the construction of anti seismic houses using these blocks and their utilization in building shelters in disaster areas. The cost, labor, and equipment analysis of constructing EPS bricks production factory of 40, 000 bricks daily production capacity was also hashed over in this research. He claimed that villagers and house owners could build houses themselves using panels produced from EPS blocks and assumed the next step should be in producing EPS concrete hollow blocks for load-bearing applications.

Hago, et al. 2002; 2004 and Al-Jabri, et al. 2005 developed a comprehensive study of the structural and thermal properties of lightweight aggregate concrete hollow blocks. They developed a comparative study between hollow blocks made from NWC, vermiculite and EPS lightweight concretes to optimize strength and thermal insulation. The experimental parallel programs aimed at producing several mixes of EPS concrete and vermiculite of several densities by varying the volumes of water, sand, 10 mm coarse aggregates and lightweight aggregates. The w-cm ratio used in EPS concrete was kept at 0.6 and the OPC volume was kept constant. The EPS beads had a diameter range between 1 and 6 mm. The cement content was kept constant. The vermiculite concrete mixes density ranged between 2242 and 1405 kg/m^3, and the EPS concrete density ranged between 1555 and 850 kg/m^3. They tested 100mm cubes for compressive strength and hollow blocks of dimensions 200x200x400mm with cubical holes of dimensions 110x75x200mm. Another type of lightweight concrete blocks was formed of an EPS plate molded, sandwiched, between two normal-weight concrete faces and was also tested. The experimental tests comprised compressive tests on cubes and hollow blocks, masonry column tests and thermal conductivity tests on hollow blocks. The thermal conductivity test was performed by means of guarded hot box built specifically for the blocks' size by the authors following the guidelines of ASTM-C236-89.

The compressive strength and thermal conductivity tests were conducted on all the mixes of the hollow blocks made with vermiculite concrete, the optimum criteria corresponded to 18.68 kg weight, 1168 kg/m^3 gross density, 2.2 MPa block compressive strength, and k-value corresponding to 0.76 W/m.K. On the other hand, the compressive strength of the EPS concrete cubes ranged between 7.05 MPa for the highest density and 0.92 MPa for the lowest one. The authors selected an optimum mixture of 1320 kg/m^3 density which produced 5.52

MPa cube compressive strength, and hollow blocks of 12.77 kg weight, 798 kg/m^3 gross density, 3.53 MPa block compressive strength, 2.24 MPa masonry column compressive strength, and k-value corresponding to 0.60 W/m.K. The properties of the sandwich concrete-EPS block, which the authors dubbed PolyBlock2 were 22.68 kg weight, 1418 kg/m^3 gross density, 10.2 MPa block compressive strength, 7.56 MPa masonry column compressive strength, and 0.616 W/m.K. thermal conductivity. The results were compared against the properties of ordinary hollow block concrete of weight: 19.06 kg, gross density: 1193 kg/m^3, compressive strength range: 5-15 MPa, masonry column compressive strength: 5.48 MPa, and k-value of 1.60 W/m.K. The authors concluded that the EPS beads concrete produced an optimum lightweight concrete hollow blocks of low thermal conductivity and suitable strength for non-load bearing applications. They further extended their research to build three rooms, one with ordinary hollow blocks and the other two were built with EPS concrete hollow blocks (PolyBlock1) and PolyBlock2 (Al-Jabri, et al. 2005). The authors monitored the temperature of its interior walls during winter and summer and reported that the inside walls temperature in the room built with PolyBlock1 was the lowest.

Gaggino, 2006, agreed with Godwin's announcements, and more, she put them in numbers and market comparisons. She reported the mechanical and physical properties of the plates made with EPS mortar bricks—as she referred to them instead of panels—were used in low-income ecological housing in Argentina and Uruguay. EPS mortar bricks replaced traditional earth-cooked ones that were produced from a polluting desertification-causing industry. She, too, believed that EPS mortar bricks can be produced domestically by house owners in impoverished areas and went further by presenting the mix design, tools and final products. The EPS mortar bricks and plates were produced from EPS waste crumbles, cement and water. The plates were longitudinally and transversally reinforced with 6 mm diameter iron bars at the mortar joints.

A comparative strength, durability, thermal conductivity and cost analysis of the EPS concrete plates and other building systems and materials available in the market were presented in this research. The proposed EPS mortar brick was molded by means of a mechanical press and had a bead size of 5-7 mm range. The EPS mortar brick plate had dimensions of 20 cm width, 240 cm length and 7.5 cm thickness and unit weight of 600 kg/m^3. Its compressive strength, thermal conductivity and water absorption values were 3.92

tons, 0.15 W/m.K., 9% to 15.7% respectively and the plate cost $27. Gaggino, 2006 compared between the 5 cm thick traditional concrete brick walls and found that EPS mortar plates are 4 times lighter, 6.4 times more thermally insulating, 6.3 times less compression resistant, and 1.2 times cheaper. She performed the same comparison with other commercially available block and brickwork. She concluded that reinforced EPS mortar plates serve as thermally insulating external wall system for non-load bearing applications.

2.3.3 Numerical evaluation of the equivalent thermal conductivity of hollow blocks

The instrumentation required to measure the thermal conductivity of hollow block units is very limited in Egypt. Only one environmental chamber operating by means of guarded hot box method is available and it measures the U-value, which is the overall thermal conductivity of walls. The only obvious solution was to either construct a guarded hot box, which requires strict quality control and expertise or opt for numerical modeling of the hollow blocks.

Numerical analysis of heat transfer problems through convection and a combination of convection and radiation in square cavities have been extensively researched (De Vahl Davis 1983; Fusegi, et al. 1991; Barakos and Mitsoulis 1994; Kumar and Eswaran 2010). Recently, the numerical analysis of the heat transfer problem inside the cavities of hollow blocks has attracted many civil and architectural engineers. The easiness by which the number and geometry of the cavities could be simulated, in addition to the advanced computational power made possible the accurate simulation of the heat transfer rate flowing through a building envelope made of hollow blocks. Many researchers proved that complex interactions between the three modes of heat transfer occur in blocks and bricks that contain cavities. The numerically obtained equivalent thermal conductivity of hollow blocks and bricks considering the three modes of heat transfer very much simulates the obtained experimental results.

J. del Coz Diaz, et al. April, 2008 developed a capstone numerical and experimental study the of conduction, convection and radiation phenomenon in walls made of hollow bricks. The experimental phase of their research yielded five compositions of different densities of lightweight concrete and the corresponding k-value. Three types of mortars, insulating, light and ordinary, were also experimentally developed and tested for their thermal conductivities.

They proposed four different configurations of hollow bricks of dimensions 0.20x0.30x0.35m and numerically analyzed each shape for the five lightweight concrete cases. Four 2-D models, one for each hollow brick type, were developed to compute the equivalent thermal conductivity of an assembly of five bricks to account for both the cavities in the brick and the recesses between them. At this stage, the best hollow brick configuration was selected based on optimization between the weight of the brick (for laborers comfort and productivity) and thermal efficiency. A 3-D model was built using the optimum hollow brick configuration with the variation of the thermal conductivity of the lightweight concrete (5 cases) and the mortar type. They concluded that they have met the Spanish Building Standard Code (CTE project) requirements with the proposed lightweight hollow bricks. they also concluded that the overall equivalent thermal conductivity of the walls increased with the increase of K-value of both the material of the brick and mortar. They suggested although the thermal efficiency of the proposed hollow brick wall is high, and its weight is light, it is expected to carry smaller dead-loads. Finally the accuracy and versatility of finite element models in depicting the equivalent thermal conductivity of complex wall structures were praised.

In another research, J. del Coz Diaz, et al. June, 2008 proposed other hollow brick configurations of by varying the size and holes configurations. The same process was repeated for five and three different types of lightweight concretes and mortars respectively. The increase of the width, size and distribution of holes in the hollow bricks gave them more versatility and more options for optimization.

Baig, 2008 studied the coupled effect of conduction-convection and conduction-convection-radiation in FEM of a representative module of size 0.2x0.2x0.15m of a concrete hollow block. His thesis dissertation presented a complete study of the parameters affected by the accommodation of two and three modes of thermal transfer. The parameters that he chose to study were: different number of partitions in the width direction to create several cavities while maintaining same void ratio, staggering the cavities, filling cavities with insulation, and different values of emissivities for the conduction-convection-radiation scenario. He assessed in his analysis the effect of the above varying parameters on the flow pattern and temperature distribution in the centerline of the modeled hollow blocks, the velocity in the direction of thermal gradient, and the heat transfer rate across the hollow blocks. He also studied the effect of radiation in general on the heat transfer rate of the different hollow blocks and the

effect of the variation of radiation with wall emissivity on the convection mode in the conduction-convection-radiation scenario. He concluded that in the conduction-convection scenario: increasing the cavities to two significantly decreased the total heat flux by 21.1% while three cavities only decreased the flux by 28.3%. The effect of six cavities yielded a heat flux equivalent to that obtained by insulation-filled core hollow blocks. On the other hand, when radiation was included, the total heat transfer rate increased by 30%, which demonstrates the importance of its computation. Also, changing the emissivity from e=1 to e=0.1 reduced the R-value from 41% to 7%. Similarly to J. J. del Coz Diaz, et al. April, 2008, he concluded also that reducing the thickness of the conductive shell—within safe limits—reduced thermal bridges and conduction heat leaks. And, increasing the aspect ratio of cavities reduces significantly the effect of the convection mode.

Sun and Fang 2009 employed 3-D numerical model for the thermal analysis of 0.240x0.115x0.090m concrete hollow blocks of different 71 configurations maintaining a constant void fraction volume of 37.80%. The simulation aimed at estimating the equivalent thermal conductivity for three different scenarios: 1-conduction only (K_{cond}), 2-conuction-convection ($K_{cond-conv}$), and 3- conduction-convection-radiation (K_{tot}). The configuration of the blocks changed by adding enclosures parallel and perpendicular to the direction of heat transfer (width and length respectively) and staggered enclosures. They found out that the increase in number of enclosures in the direction of heat transfer decreases significantly the equivalent total K-value (K_{tot}). On the contrary, the increase in number of enclosures in the direction perpendicular to the heat transfer has an adverse effect on the K_{tot}. The contribution of the k-value relevant to each mode was calculated and discussed. The conduction had the dominating contribution followed by the radiation in second place and the least contribution was done by convection. They concluded their research by indication than the equivalent thermal conductivity of hollow bricks depended largely on the interaction of the three modes of heat transfer.

2.4 Ferrocement

The past thirty years comprised extensive research on the ductile failure of ferrocement. The inclusion of narrowly spaced wire mesh works as lateral and longitudinal reinforcement to the confined mortar. This research utilizes the confinement effect of ferrocement in hollow

blocks subjected to compressive load. Therefore, it is only relevant to discuss in this section the confinement characteristics of ferrocement.

2.4.1 Ferrocement confinement of concrete and EPS-Core under compression

Johnston and Mattar 1976 studied the effects of the wire mesh type, geometry, orientation, and number on uni-axial tension and compression of ferrocement. They also provided an original study of assessing the confinement effect of a ferrocement hollow column confining a soft EPS core. The materials used were: expanded metal diamond grid with dimensions (EXMA), expanded metal diamond grid with dimensions (EXMB) and galvanized welded wire mesh (EWM). The expanded metal EXMA with steel strands in the shape of flat diamond grid with dimensions 29 mm X 13 mm and orientation 24 and 66 degrees with the direction of stress. The expanded metal EXMB with steel strands in the shape of flat diamond grid with dimensions 22 mm X 13 mm and orientation 31 and 59 degrees with the direction of stress. In addition to the galvanized welded wire mesh EWM had 13 mm square grid with wires parallel and perpendicular to the applied stress (0/90) or wires at 45 degrees to the applied stress (45/45). Two types of mortars were used; the mortar used in tension test had a cylinder compressive strength of 69 MPa while the mortar used in compression tests had a cylinder compressive strength of 38 MPa.

The test program included tension and compression tests on ferrocement specimens. The uni-axial tension tests comprised 914 mm long by 102 mm width by 13mm to 38 mm thickness specimens, lateral and axial strains were recorded by 20 mm foil strain gages. The uni-axial compression tests comprised twenty five specimens of dimensions 305mm X 102mmX 102mm, half the specimens were solid mortars and the other half had polystyrene core of dimensions 305x64x64mm, lateral strains were recorded by 76 mm foil strain gages and average axial strain was recorded by means of 76 mm transducers.

The parameters studied in the uni-axial tension tests were the type, orientation, and number of reinforcement mesh and the thickness of the specimens. They reported that the thickness of the mortar did not play a significant role in uni-axial tensile tests since it was cracked long before reaching the ultimate failure of the section and did not contribute to load resistance. The authors recommended that for accounting for reinforcement steel in uni-axial tension, the effective area of steel should denote the effective area of steel per unit loaded width of the

section or per unit area of the finished surface of the specimen. The orientation of steel reinforcement in ferrocement is essential to its efficiency in resisting tensile stresses. The authors reported that based on the content of the used steel, the expanded metal was more economic and effective for uni-axial tensile load applications as it gave 75% more uni-axial tensile load resistance than that provided by welded mesh because of the steel content in the longitudinal direction of stresses was more in the former. However, welded wire mesh with its square openings provided consistent resistance to both uni-axial and bi-axial tensile stresses. Ferrocement made with expanded metal was characterized by higher stiffness, cracks were invisible and if existed would only appear before failure and would be very fine and closely spaced. On the other hand, ferrocement made with welded wire mesh were less stiff and developed cracks that were visible before the failure of specimens. The spacing and intensity of these cracks decreased when the specific surface of reinforcement was increased. The authors found that the strength of the reinforcing steel was not an important parameter and was not the governing factor in the crack spacing and deformation stiffness of ferrocement under uni-axial tension; the key parameters were the orientation of reinforcement and its material characteristics.

The parameters they studied in the uni-axial compression tests were the type, orientation, and number of reinforcement mesh used in the absence and presence of polystyrene core. The distinguishing characteristic of ferrocement is its two-direction reinforcement which plays a major role in increasing the tri-axial confinement of the involved mortar. The authors drew a very interesting analogy of ferrocement composite under uni-axial compression. The longitudinal reinforcement act as standard bars and the transverse one act as helical reinforcements to the columns of mortar in the ferrocement composite, this combination of reinforcement confined the included mortar column structure and exploited its tri-axial strength during compressive loading. In ferrocement under compression, the mortar strength influenced deeply its strength, unlike in tension. The authors found that welded wire mesh were superior to expanded wire mesh for reinforcing concrete under compression because of the lateral confinement provided by the transverse steel to the mortar. The load-carrying components in ferrocement under compression were: the mortar, longitudinal steel (resisted 5%-14% of the load) and lateral steel (resisted 17%-42% of the load). The failure of

ferrocement under uni-axial compression was a complex phenomenon that was affected by various factors.

On the other hand, the confinement behavior of ferrocement composite under compression was explored. They studied the behavior of solid and polystyrene core columns confined with ferrocement under compression and noticed that the higher the volume reinforcement of welded wire mesh in cored columns the higher the compressive strength, which was not the case for solid columns. The authors estimated the reinforcement volume at which compressive strength increased with adding more welded wire meshes was 192 kg/m^3 and a threshold reinforcement volume of 272 kg/m^3 at which the lateral confinement provided by the reinforcement ceased to be effective. The explanation was that ferrocement composites failed under compression by mortar dilation outwards, which was restrained by the effect of lateral reinforcement. However, in soft cored columns, mortar dilated both inwards and outwards and the core was responsible in retraining the inward dilation and the reinforcement was responsible in restraining the outward dilation. At a certain extent after which the soft core was rendered ineffective in restraining inward dilation, the increase in reinforcement also was rendered ineffective and the specimen failed.

Another remarkable finding by the authors was that in heavily reinforced cored ferrocement prisms, beneath the threshold reinforcement, the longitudinal welded steel contributed to 20% of the load-carrying capacity as compared to the 5%-14% in solid prism. They attributed this phenomenon to the failing core ability to restrain the mortar dilation. Also, they pointed out that the lateral steel carried a range from twice to six-times the load carried by longitudinal steel. They also related the behavior of cored ferrocement columns in failure and their response to the increased amount of reinforcement to the amount of confinable mortar in cored specimens. The confinable mortar in cored ferrocement columns was attributed to 80% while for solid cores was 88%. They suggested that the amount of reinforcement in ferrocement cored columns should be studied to balance between the amount of confinable mortar and the buckling strength of longitudinal reinforcement. They concluded that there was a limit strength to cored ferrocement composites and rendered the topic as volatile to many variables and fertile for future research. This phenomenon is very important to the study at hand.

2.4.2 Ferrocement-confined aerated concrete blocks

Memon, et al. 2006; 2007 utilized the advantages of ferrocement confinement by encasing an aerated concrete block in a high performance ferrocement box. They investigated the unit weight, ultimate compressive strength, flexural strength, water absorption, and failure mode of the sandwich block. The materials used were OPC, ground granulated blast furnace slag (GGBFS), aluminum powder, wire mesh and super plasticizer. The aerated concrete ingredients were: binder to sand (passing through 600 μm sieve) ratio was 1:1, water ratio to dry mix was 0.23, aluminum powder ratio to dry mix was 0.1%, a super plasticizer to binder ratio of 0.55%, and the GGBFS replaced 50% of cement. The ferrocement mortar ingredients were: binder to sand ratio was 1:2, the binder to water ratio was enough to produce a flow value of 136+/-3% with a super plasticizer ratio of 0.2%, and the GGBFS replaced 50% of cement. Two types of wire meshes were used; square mesh of 1mm diameter and 12mm and hexagonal mesh of 0.5mm diameter and 18 mm x 14 mm wire spacing. The pouring procedures took effect on two days; on the first day, aerated concrete was poured in a mould that was 376 mm x 200 mm x 76 mm size. On the second day, the wire mesh was wrapped in a cage-like shape around the block and mortar was poured on it in a space of 12 mm implementing efficient vibration.

The experimental program comprised 24 units of 400 mm x 200 mm x 100 mm ferrocement-aerated blocks divided into nine batches two of which were one control batch cast only with aerated concrete and another cast with a 12 mm plain mortar encasing aerated concrete block. The design density of the aerated concrete block was 1200 kg/m^3. Each batch contained three specimens and the varying parameter was the type and number of wire mesh layers. The produced sandwich composite had more compressive strength than the plain block. The authors noticed that the composite block made with square welded wire mesh ferrocement increased the compressive strength of plain aerated concrete block by 101% and that of mortar encased aerated composite by 43%. Also, ferrocement encasement made with square wire mesh gave 20% more compressive strength than that made with hexagonal wire mesh.

In a parametric study, they noticed that the rate of strength enhancement falls by including more than one layer of square wire mesh in the ferrocement skin and suggested that one layer of square wire mesh in the ferrocement face was adequate. The failure pattern of the composite block was ductile and first crack appeared at about 60%-80% of the failure load,

unlike the mortar confined block which showed first crack at 90%-96% of the failure load and then collapsed suddenly. Failure was noticed by the initiation of fine cracks at the first crack load, which widened with the increase in the applied load. The final failure occurred due to cracks in the ferrocement skin. The ductile failure exhibited full composite action, the layer of ferrocement was cracked and sometimes chipped off but complete or sectional detachment of the ferrocement skin never occurred. On the other hand, the application of the ferrocement skin enhanced the physical characteristics of aerated concrete. The average water absorption of aerated concrete block was 16.72 and dropped to 3.79 with the encasement of the ferrocement skin. The density of the proposed sandwich block was 1600 kg/m3 with and compressive strength range of 15.5-20 MPa.

2.5 Durability of Concrete

Ravindrarajah and Tuck, 1994 were the only researchers who conducted comprehensive durability tests on EPS mortar and concrete specimens, although their report was conclusive that EPS mortar showed signs of resistance to acid and salt attack, the signs of deterioration were not inclusively discussed. On the other hand, Babu and Babu 2003 showed that EPS concrete had good quality in terms of absorption values and very low chloride permeability. Therefore, it is assumed that EPS is resistant to acidic and salt attack but the mortar matrix may not be as resilient. This section discusses some deterioration characteristics of plain and reinforced mortars when subjected to sulfuric acid and sodium chloride salt attack.

2.5.1 Sulphuric Acid Attack

It is obvious that the research done on the durability assessment of ferrocement is rather limited, especially those involving subjecting ferrocement to acidic environments. Although it is quite an approximation, the research performed on mortars could be utilized to partially assess and predict the deterioration of ferrocement under abrasive and acidic service conditions.

Fattuhi and Hughes 1988 studied the effect of sulphuric acid on cement pastes and concrete samples. Their parametric study included varying the w/c ratio, cement content and specimen's age. The experimental program comprised two series. Series I represented the paste mixes with varied w/c ratio between 0.26 and 0.417. Series II represented concrete and contained five mixes, four of which had varied w-cm ratio 0.4, 0.5, 0.6 and 0.7, the fifth mix

had w-cm ratio of 0.47. The authors prepared five 100 mm cubes, three for testing density and compressive strength of the concrete mixes and two for testing the effect of sulfuric acid for each condition under investigation. The test set up was formed of a flowing channel of 2% concentration of sulphuric acid, worst case scenario, and an average pH value of 1.78. The acid concentration was checked regularly by means of Na(OH) of predetermined strength and depleted acid was refilled to maintain the 2% concentration. Once a refill was done the channel was brushed of any debris. The test was run at 22 to 26 degree Celsius. The cubes were immersed in the channel at different ages between 1 and 30 days and were removed for periodic weighing, photographing and repairing. Prior to the weighing process Series I cubes were vigorously brushed under tap water to clean any debris while Series II was lightly brushed.

The authors reported that for Series I, the age of cement pastes before acid immersion affected their weight loss. They reported that w-cm ratio of 0.471, cement paste cubes immersed in acid after 28 days of maturity suffered 75% less weight loss when compared the cubes immersed in acid at 7 days maturity. In addition, they attributed the weight loss to the brushing scheme of the surface. They noticed that 7-day mature cubes tend to cease losing weight after a four week immersion in the acidic solution when they were kept un-brushed. The authors attributed this cessation due to the formation of a thick whitish-yellowish layer of gypsum that reduced the permeability of acidic water. The weight loss exhibited by 7-day old brushed and un-brushed cubes after 48 day acid immersion 45.9% was and 26.3% respectively. The lower w-cm ratio, except for w/c = 0.26, the higher the weight loss. This is because lower w-cm produced higher content of calcium hydroxide which reacted with the sulfuric acid. On the other hand, the lower weight loss in cubes with higher w/c ratio was explained by the formation of a very thick layer of impermeable gypsum that was difficult to be removed. Cubes of 32 day maturity and acid immersion of 46 days recorded 50% and 22.5% weight loss by cubes made with w-cm ratio 0.3 and 0.4 respectively. All cement paste cubes showed cracks after 24 days of acid immersion, some cubes were split and held together by the passive gypsum layer.

On the other hand, the weight loss exhibited by the concrete cubes of Series II was slightly affected by the age, maturity, of the cubes prior to their 49 day immersion in the acidic channel. Also, the brushing scheme had little effect on the weight loss as the weight loss in

brushed cubes was 7% higher than the weight loss in un-brushed cubes. In addition, the weight loss exhibited by cubes made with lower w-cm ratio was higher than that exhibited by cubes made with higher w-cm ratio. They also reported that the weight loss of concrete cubes made with w-cm ratio of 0.4 was 25% which is three times more than the 7.9% weight loss exhibited by cubes made with w/c ratio of 0.7 after 49 days of acid immersion. They attributed this large gap to the fact that cubes made with lower w-cm ratio had more cement content to react with the sulfuric acid flow. The deterioration of the concrete cubes recorded after 27 days of immersion was characterized by surface erosion of the cement layer and the exposure of the aggregates. The authors concluded that, contrary to the conventional, concretes subjected to environments where sulphuric acid might exist should have low cement content.

Sulphate attack also causes mortars and concrete to deteriorate. Shannag 2008 investigated flexural strength of ferrocement plates subjected to sulfate environments. The materials used were three types of galvanized woven wire mesh of 0.63 mm diameter and three different wire spacing 3.15 mm, 6.3 mm, and 12 mm. The mortar was prepared with the mix proportions 1:1:0.5:0.02 corresponding to OPC, sand, water and super plasticizer which yielded a compressive strength a 28-day compressive and tensile strengths of about 60 MPa, and 5 MPa, respectively. The test program comprised 54 specimens of size 300x75x12.5mm prepared with two and four layers of square wire mesh. The parametric study included varying the number of wire mesh layers, wire mesh spacing, and curing environments. After 28 days, the ferrocement specimens were submerged for a year in three different solutions 5% magnesium sulphate solution, 5% sodium sulphate solution or tap water.

The author tested the specimens under flexure and reported the first crack load, ultimate load and load deflection value and the degree of mesh deterioration. He reported that the specimnes stored under tap water exhibited increase in flexural strength with the increase in the number of wire mesh layers and decrease in wire spacing. He explained this increase because more wire layers increased the volume fraction of reinforcement and increased the depth of mesh layer from the neutral axis which resulted in an increased moment arm and flexural strength. Further he used the specimens immersed under tap water as a reference for comparing the results of the other specimens against. Shannag 2008 attributed the behaviour of ferrocement plates immersed in sodium sulfate solution to mainly the effeciency in their

preparation. He reported that ferrocement of 2 wire meshes and small, medium and large spacing exhibited an increase in flexural strength of 24%, 7%, and 20% respectively, which corresponded to an increase of 178%, and a decrease of 33% and 11% in energy absorption respectively. the author explained that the period was insuffeceint for sulphate reaction to take place because of the good quality of the mortar which was well compacted. On the other hand, spacimens with four layers of wire mesh were not as compacted and deterioration in flexural strength and energy absorption was noticed. He reported that ferrocement of 4 wire meshes and small, medium and large spacing exhibited a decrease in flexural strength of 28%, 19%, and 3% respectively, which corresponded to a respective decrease 11%, 18%, and 28%. The specimens immersed in magnesium sulphate solution showed similar trend but with more adverse effects because magnesium sulphate degrades hydrated calcium silicates, $Ca(OH)_2$ and hydrated C_3A while sodium sulphates degrades $Ca(OH)_2$ and C_3A only.

2.5.2 Sodium Chloride Salt Attack

Koniorczyk and Gawin, 2008; and Koniorczyk 2010 studied the damaging effect of salts on porous building materials such as cement bricks and mortars. There are two damaging effect of salts when present in the pore structure of porous building materials, namely, 1-corrosion and 2- salt crystallization. Corrosion is triggered by chlorides that exist in two forms; the first is free chlorides in the pore structure and is responsible for corrosion while the second is bound chloride. On the other hand, salt crystallization occurs in supersaturated salt solutions, as the one used in this research.

Koniorczyk 2010 presented experimental analysis, mathematical derivations and numerical modeling of the damaging effect of salts on mortars when subjected to different scenarios such as salt solution, super saturated salt solution, wet-dry cycles, and hot-cold cycles. The experimental investigation comprised analyzing mortar specimens using Mercury Intrusion Porosimetry (MIP) which is a technique used to characterize the distribution of pore sizes in cement-based materials, and scanning electron microscopy (SEM), which observes the micro structural porosity including capillary pores. They tested 40x40x160mm mortar specimens to investigate the effect of salt precipitation in the gel pores of mortars on the mortars' porosity. The specimens were cured for 30 days then specimens were dried and later saturated in NaCl solutions of concentrations: 0%, 15%, 20%, and 25% (kg of NaCl to Kg of water). The saturation process was done on three stages, firstly, 1/3 of the sample was covered with the

saline solution, secondly, 2/3 of the sample was covered and finally the whole specimen was submerged in the saline solution. The first and second stages lasted for 2 days while the third lasted for 30 days. The drying regimen was then followed by allowing the samples to dry in ambient temperature of 105 degrees Celsius. The fast drying allowed the evaporation of water and precipitation of salts. MIP and SEM tests were conducted on 1 cm^3 specimens extracted from the surface zone of the mortars.

The authors found that the amount of precipitated salt depended on the initial amount of salt in the saline solution. They found that in saline solutions with higher slat concentration, the macro-pores inside mortars were clogged and the mortars' porosity decreased. Also, the diameter of the inner surface pores decreased at higher salt concentration owing to the same pore clogging phenomenon. The MIP analysis showed that at salt precipitation of 0% (control), 6.12%, 10.95%, and 12.88% the mortars porosity decreased from 23.72% (control) to 19.33%, 15.69%, 14.03% respectively. The authors formulated a mathematical derivation and a numerical model to simulate salt precipitation and water migration phenomena and the results from the simulation agreed well with experimental results. They simulated the capillary suction and migration of salt water inside the gel pores of mortars and found that, because water molecules are 3 to 5 times smaller than Na+ and Cl- molecules, salts precipitated in the gel pores and allowed water to migrate through the pores to the mortars' surface—where higher concentrations of salt existed.

Further, the authors used the numerical model to simulate the drying of three walls subjected to salt solution; the first was simulated considering the pore-clogging phenomenon (change in permeability). The second wall was subjected to the salt solution and the model accounted for a change in porosity (permeability) in addition to the effect of sorption isotherms, which assumes that as the concentration of soluble salts increase in the mortar pores, the higher is the water content at a certain relative humidity and thus the slower the drying process gets. On a side note, Spragg, et al. 2011, reported the delayed drying and weight-retaining phenomena of mortars soaked in cycles of 23% NaCl, 32% $CaCl_2$, and 30% $MgCl_2$ saline solutions in an extensive experimental investigation and demanded further research. The third wall was wetted with clear water and was used as a datum. The simulation period was set to 3 years and the drying mechanism of water was monitored. The authors found that the moisture content of the second wall decreased by 1.95 kg/m^2, which is 55% higher moisture content

than the 3.57 kg/m^2 recorded for the control. They concluded that the effect of retaining moisture inside of the pores of mortars subjected to saline solutions was more dangerous and prominent than the effect of clogging pores with salts. The authors subjected the second wall to seasonal effect during drying and reported that the concentration of salts inside the walls remained constant and varied on the external surface of the walls which would result in efflorescence in the summer-spring seasons, when moisture content is at its lowest.

Lubelli and de Rooij 2009 studied the deterioration of plasters and renders due to NaCl (halite) salt crystallization. They investigated the location and shape of halite crystals and discussed the corresponding deterioration. They prepared fire clay specimens of dimensions 5x5x5 cm^3 and added a plaster layer on it of approximately 2 cm thick. The specimens were sealed on lateral sides with epoxy-resin and left to dry in dried in an oven at 60 C until constant mass. The specimens were then left to reach room temperature and then were contaminated with 10% NaCl solution by capillary rise till the evaporation of 80% of the saline solution. Afterwards, rewetting procedure through capillary rise was repeated. To accelerate the drying cycles the specimens were dried in two different environments 8 h at 35 C and 20% RH followed by16 h at 20 C and 65% RH. The test was terminated either when plaster was damaged or after five wet cycles.

The authors used SEM in studying the salt crystallization of halite inside the plaster and found that the location of salts was directly determined by the moisture transport properties of the plastering layer. Also, the pore system of plasters was responsible of rate of crystallization and shape of halite. For example, thin whiskers of halite crystals were seen on fine porous plasters that had low moisture transport while regularly shaped bigger crystals were noticed on plasters that had large pores and high moisture transport. They reported that the type of damage due to salt crystallization was related to the location where salt crystals accumulated. Plasters that had high moisture transport and bigger pores had salt crystallization near the evaporation surface and were subject to loss of the plaster's cohesions. On the other hand, salt accumulating plasters that are characterized by low permeability and smaller pore size had salt accumulation in deeper substrates and cracks initiated parallel to the evaporation surface.

Research done concerning the corrosion of ferrocement is scarce, however Mansur, et al. 2008, provided guidelines and analysis of different corrosion assessment and remedy

techniques of ferrocement. They researched three defense mechanisms, each one separately, in attempt to produce corrosion resistant ferrocement, the first was coating the steel mesh with corrosion inhibitor, the second was increasing the quality of cement mortar, and the third was coating the ferrocement composite with corrosion inhibitor. The aim was to devise the optimum procedure for corrosion delaying or inhibiting in ferrocement. A total of 65 specimens with dimensions of 330 mm length, 100 mm width and 20 mm thickness each was reinforced with four welded wire mesh square grids of 12.7 mm spacing and 1 mm diameter were prepared. The specimens were divided into 13 groups of fives. A control mix (CM) was made cement content of 661 kg/m^3, sand to cement ratio of two, w-cm ratio of 0.43 and a concrete cover of 5mm. The specimens were divided into three main groups: specimens that had direct protection to steel, improved matrix quality and ferrocement surface protection. Table 2.1 summarizes the parametric study conducted by Mansur, et al. 2008.

Table 2.1: Summary of the accelerated corrosion test program (Mansur, et al. 2008)

Type of protection	**Parameter**	**Description**	**Mortar Mixture Designation**
Direct protection to steel	Corrosion inhibitor	Prescribed dose	CM+
	Concrete cover	6mm	CM
		3mm	CM
Quality of mix	W/c ratio	0.35	0.35
		0.5	0.5
	Sand/cement ratio	1.5	1.5
		2.5	2.5
	Fly ash to cement	25%	FA-25
		50%	FA-50
	Silica fume to cement	10%	SF-10
Ferrocement surface protection	Surface coating	Elastomeric paint	CM

Two of each five specimens were kept under natural conditions, and the rest were subjected to accelerated corrosion by being exposed to wet-dry cycles of 3% NaCl solution. During the wetting cycles the specimens were kept immersed in an upright position in a galvanostatic cell with 3% NaCl solution. Electrical current was impressed through the embedded reinforcement (anode) by applying a fixed potential across it and a cathode. The cathode was represented by the same type of wire mesh and equivalent surface area wrapped around the specimen. The drying cycles were achieved by pumping out the cell's solution. The exposure

continued for 58 days and each wet cycle lasted for a day then followed by a drying cycle that lasted for 2.5 days. They evaluated the proposed protective schemes by assessing the maximum crack width, loss of steel, and deterioration of flexural strength that would result from the corrosion of embedded wire meshes.

They reported that corrosion was noticed as early as 16 days into the experiment due to the development of expansive corrosion products around the wire mesh that caused in a pressure strong enough to crack the mortar. Specimens made with 10% SF did not develop such early cracks. Corrosion cracks did not follow a consistent pattern but propagated with prolonged exposure and rust stains poured out of them. Comparing the cracks developed by all the specimens to the control one, the best protective scheme was using 10% silica fume, then surface coating followed by 25% FA that generated corresponding maximum crack width of 0 mm, 0.02 and 0.02 mm. The lowest steel loss percentage was recorded by the SF specimens that lost 1% of the diameter of its steel, followed by stainless steel reinforcement and surface coating which lost a respective 2.5 and 3 %. The control specimen lost 8% and the specimens made with sand to cement ratio of 2.5 was the worst performance and lost 15.5%.

Furthermore, Mansur, et al. 2008 reported that the accelerated corrosion test adversely affected both the strength and ductility of ferrocement. The failure pattern was sudden into two halves, unlike the more prolonged and distributed failure pattern displayed by the naturally preserved specimens. They reported that again 10% SF gave a 14.7 % strength loss, which was the least strength loss in all the groups. The control specimens lost 57% of its strength and the highest strength loss was recorded by specimens made with 2.5:1 sand to cement ratio which lost 69.7% of their strength. The authors concluded that the best corrosion protection schemes for ferrocement in decreasing order of performance were using 10% SF, surface coating, 25% FA, 50% FA, and deep mortar cover (5 mm or more).

The work done by Almusallam and Yousef, 2006 presents one of the scarce studies on the effect of cyclic exposure and ponding of GFRP concretes in NaCl solution. They aimed at studying the long-term durability of GFRP reinforced beams under sustained load and subjected to various adverse conditions. The experimental program comprised 36 concrete beams of 100 X100X2000mm^3 each reinforced with one GFRP bar of 10mm diameter. The beams were designed to sustain shear load without the extra support of stirrups and that the

sustained load would use only 20 to 25% of tensile strength of the GFRP bars. The bars were coated with high alkali cement paste at the middle (a distance 40 X40X700mm^3) to increase the alkalinity content around of the bar and to facilitate the bar's removal from concrete during testing. The materials used were concrete of 120-day average cylindrical compressive strength of 43 MPa, GFRP bars of tensile strength, maximum tensile strain and static modulus of elasticity corresponding to 743MPa and 0.0187 and 39 GPa.

The test program comprised 36 beams tested in three different exposure conditions. The first exposure condition was continuous immersion in tap water at 40 degrees Celsius (T1), 12 beams were tested, 6 loaded and 6 not loaded. The second exposure condition was continuous immersion in seawater at 40 degrees Celsius (T2), 12 beams were tested, 6 loaded and 6 not loaded. Finally, the third exposure condition was wet/dry cyclic immersion in seawater at 40 degrees Celsius every two weeks (T3), 12 beams were tested, 6 loaded and 6 not loaded. Local seawater was brought from the Arabian Gulf to represent service conditions the eastern province of Saudi Arabia. Three strain gages were embedded in the middle portion of the beam for strain recording during testing; for each exposure condition 4 beams (2 loaded and 2 unloaded) were tested at 4, 8, and 16 months. GFRP bars were extracted at the scheduled time of testing and tensile test was conducted on the bars.

The authors reported that the GFRP bars embedded in unstressed and stressed beams subjected to continuous immersion of marine environment (saline ponding) lost 19.7% and 47.9% respectively after the exposure of 16 months. On the other hand, GFRP bars embedded in unstressed and stressed beams subjected to wet/dry cyclic immersion of marine environment lost 21.8% and 55% respectively after the exposure of 16 months. The strength loss was mainly due to moisture exposure and little was the effect of chloride ion corrosion. This is because, GFRP bars embedded in unstressed and stressed beams subjected to continuous tap water immersion lost 16.3% and 47.1% respectively after the exposure of 16 months. The authors prepared additional GFRP beams—same design and exposure program—and tested them for flexure after 8 months. The reduction in failure loads of the unstressed beams was 12.5, 26.4, and 20.8% for beams subjected to exposure T1, T2, and T3, respectively and the reduction in failure loads of the stressed beams was 30.6, 25.0, and 33.3% for beams subjected to exposure T1, T2, and T3, respectively.

Further, they reported that the stressed and unstressed GFRP bars subjected to the three exposure conditions showed reduction in ductility as indicated by the load deflection curve. An important observation was that during testing the unstressed GFRP concrete beams kinks due to slippage of bars were observed at low rate of stress, after which the test continued until failure. The reduction in ductility as recorded by the reduction in deflection at ultimate load was 31.6% and 43.4% for stressed and unstressed beams subjected to T1 conditions respectively, was 32.9% and 46.1% for stressed and unstressed beams subjected to T2 conditions respectively, and was 22.4% and 39.5% for stressed and unstressed beams subjected to T3 conditions respectively. The results reported by the Almusallam and Al-Salloum 2006 suggest that GFRP is severely affected by wet and dry cycles more than the effect of salts in the saline environment.

Chapter 3

Experimental Program

3.1 Introduction

The experimental program was designed to investigate the mechanical characteristics of the lightweight mortar lightened with different dosages of expanded polystyrene (EPS) wastes and the viability of its application for producing EPS mortar hollow block and solid brick units of suitable mechanical, long-term and thermal characteristics to arid environments. The experimental program was divided into two phases, the first phase aimed at determining the mechanical and thermal properties of the expanded polystyrene mortar (EM). Hydraulic mortar was selected rather than concrete in this investigation to produce a lighter weight matrix. EPS was used as partial replacement of the sand in the mortar mixture. The varying parameter in this phase was the weight of EPS per cubic meter of the mixture. Five mixes were prepared with five dosages of EPS namely; 0 kg/m^3 (control mix), 10, 15, 20 and 26 kg/m^3. Cubes of dimension 150x150x150 mm and cylinders of dimensions 150X300 mm were cast and tested to determine the uni-axial compressive strength, modulus of elasticity, stress-strain curves and splitting tensile strength of each mixture. In the second phase, hollow blocks made of the EPS lightweight mortars were cast and tested for uni-axial compressive strength and cyclic exposure to abrasive environments. More variables were introduced in this phase, namely, the type of reinforcing mesh (plain without reinforcing mesh, wire mesh, and fiber mesh) in addition to the EPS dosage variation. Moreover, solid bricks were also tested for the variation of uni-axial compressive strength and thermal conductivity with EPS dosage. A total of forty five cubes, forty cylinders, hundred and forty hollow blocks and twenty five bricks were tested in this experimental program for mechanical properties, and environmental abrasion. The details of the experimental program are explained and discussed in the following sections of this chapter.

3.2 Mix Design

Four Expanded polystyrene Mortar (EM) mixes were designed in addition to the control mix. The mix design is based on partial replacement of fine aggregates (sand) by polystyrene crumbles known commercially as “Addipore 55” to produce lighter mortars. Table 3.1 shows

the proposed mix design. Silica fume was used in the mix as replacement of cement to enhance the properties of the mortar. High range water reducing admixture (HRWR) was used to improve the workability of the mixes and its proportion in kg/m^3 of the mix was adjusted so that a slump of 20 cm was achieved. The designation given to the proposed mixes was based on the nominal weight in kilograms of "Addipore 55" used together with other constituents to produce a cubic meter of the mixture. Table 3.1 shows also the percentage reduction in weight of the hardened mix as compared to the control mix.

Table 3.1: Mix proportions of the control mix and the expanded polystyrene mortar mixes

Mix Designation	Cement kg/m^3	Silica Fume kg/m^3	Sand kg/m^3	EPS kg/m^3	Water kg/m^3	HRWR kg/m^3	Theoretical Density kg/m^3	Dry Density Kg/m^3	Weight reduction %
C	455	45	1613	0	225	5	2343	2118	0
EM10	455	45	1078	10.0	225	10	1822	1747	17.5
EM15	455	45	833	15.1	225	7.5	1581	1497	29.3
EM20	455	45	605	20.4	225	6.25	1357	1257	40.6
EM26	455	45	408	26.2	225	10	1169	988	53.3

3.3 Test Specimens

The test program comprise 45 cubes of size 150 mm, 40 cylinders of 150 mm diameter and 300 mm height, 25 bricks of dimensions 235x115x65mm and 140 hollow blocks of dimensions 200x200x400mm with two cylindrical holes each of 125mm in diameter. For the EPS hollow blocks, three types of blocks were designated for each of the four mixes and the control according to the type of reinforcement in the block. These types are: plain, steel wire mesh reinforced and fiber mesh reinforced (Table 3.2).

Table 3.2: Designations for the three types of blocks and bricks

Type of Reinforcement	**Mix Designation**				
	C	**EM10**	**EM15**	**EM20**	**EM26**
Plain (blocks)	CBP	EMBP10	EMBP15	EMBP20	EMBP26
Wire Mesh (blocks)	CBW	EMBW10	EMBW15	EMBW20	EMBW26
Polypropylene Mesh (blocks)	CBF	EMBF10	EMBF15	EMBF20	EMBF26
Plain (bricks)	CBR	EMBR10	EMBR15	EMBR20	EMBR26

Where C: control mix, EM10: mix with 10 kg EPS content, EM15: mix with 15 kg EPS content, EM20: mix with 20 kg EPS content, EM26: mix with 26 kg EPS content, B: block, P: plain blocks (no reinforcement), W: wire mesh reinforced blocks, F: GFRP mesh reinforced blocks and BR: brick.

Three main characteristics were determined: 1-mechanical, 2- durability/serviceability and 3-thermal conductivity. The mechanical tests performed are compression testing, modulus of elasticity, stress-strain measurement and splitting tensile strength. The experimental program along with the samples sizes and numbers and the testing machines are summarized in Tables 3.3 and 3.4. Tests are conducted in the Materials Laboratory and Structural Laboratory of the American University in Cairo.

Table 3.3: Summary of the conducted mechanical and thermal tests, specimen type and sample size

Characteristics assessed	Test	Testing Machine/set up	Specimen	Sample size
Mechanical Properties	Compressive strength	Universal Testing Machine (UTM) and Test Frame (TF)	Cubes (150 mm)	9 cubes per mix 3 after 7, 14 and 28 days
			Cylinders (150x300 mm)	3 cylinders per mix after 28 days
			Hollow blocks (200x200x400mm)	3 to 4 blocks per mix for each block type after 28 days
			Bricks (65x115x235mm)	3 bricks per mix after 28 days
	Static Modulus of Elasticity (E)	Universal Testing Machine (UTM)	Cylinders (150x300mm)	2 cylinders per mix after 28 days
	Stress-strain Curve	MTS	Cylinders (150x300mm)	3 cylinders per mix after 28 days
	Splitting Tensile Strength	Universal Testing Machine (UTM)	Cylinders (150x300mm)	3 cylinders per mix after 28 days
Coefficient of Thermal Conductivity	Hot wire method	Unitherm TM. Model 3141	Bricks (65x115x235mm)	2 bricks per mix after 28 days

Table 3.4: Summary of the conducted durability tests, specimen type and sample size

Characteristics Assessed	Test Description	Cycle description	Specimen	Sample Size
Durability/Serviceability Properties	48-hr water absorption	48 hours of immersion in water and 48 hrs drying in room temperature and atmosphere. A sole cycle.	Hollow blocks (200x200x400mm)	2 blocks per mix after 28 days
	Cyclic ponding in super saturated sodium chloride (NaCl) salt solution.	7 days in brine pond and 7 days drying in room temperature and atmosphere. A total of 4 cycles	Hollow blocks (200x200x400mm)	2 blocks per mix after 28 days
	Cyclic ponding in 5% sulfuric acid (H_2SO_4) solution.	4 days in acidic pond and 3 days drying in room temperature and atmosphere. A total of 4 cycles	Hollow blocks (200x200x400mm)	2 blocks per mix after 28 days

3.4 Material Properties

3.4.1 Cement

Ordinary Portland Type I cement was used in the current research. The chemical composition of the cement is shown in Table 3.5. Typical results of cement testing according to the manufacturer's specifications and in accordance with ASTM C187-86, ASTM C191-82, ASTM C204-84, ASTM C150-68 and ASTM C109-88 are shown in Table 3.6. The weight of cement was kept constant during the research program at 445 kg/m^3. The average cement fineness and specific gravity was 330 m^2/kg and 3.15 respectively.

3.4.2 Fine Aggregate (Sand)

Natural siliceous sand was used as fine aggregate throughout the current research. The fine aggregates used were obtained from the new Cairo district. The gradation of fine aggregates is presented in Table 3.7 and Figure 3.1. A summary of the characteristics of fine aggregates is presented in Table 3.8. The selected sand was characterized by its coarse particles, high fineness modulus and low percentage of particles finer than sieve No. 200 which resulted in its low absorption. The amount of sand varied in the five mixes in accordance to the amount of added "Addipore 55''.

Table 3.5 Chemical composition of ordinary Portland cement as obtained from manufacturer (Torah)

Constituents	Concentration in Weight (%)
Silica as Si O_2	19.8
Alumina as AL_2 O_3	5.6
Iron as Fe O_3	2.4
Potassium as k_2 O	0.58
Calcium as Ca O	65.9
Sodium as Na_2 O	0.29
Sulphur as SO_3	2.8
Loss in ignition	1.2
Insoluble residue	0.4
Free lime	0.9
Lime Saturation Factor	100.4
Lime Combination Factor	98.9
Silica ratio	2.48
Alumina ratio	2.33
Tricalcium Cilicate (C_3 S)	65.1
Dicalcium cilicate (C_2S)	7.6
Tricalcium Aluminate (C_3A)	10.8
Tetracalcium Aluminate Ferrite (C_4 AF)	7.3

Table 3.6: Typical results of cement testing as obtained from manufacturer (Torah)

Test Name	Test results (1)	Test results (2)	Test results (3)	ASTM Standards
Standard consistency ASTM C 187-86	26%	26.5%	27%	Between 26% and 33%
Setting (initial) ASTM C 191-82	Hrs min. 2 25	Hrs min. 2 30	Hrs min. 2 35	Minimum 1hr
Setting (final) ASTM C 191-82	Hrs min. 3 35	Hrs min. 3 0	Hrs min. 3 20	Maximum 10hrs
Fineness (cm^2/g) ASTM C 204-84	3400	3250	3350	Minimum 2800
Cube strength (N/mm^2) ASTM C 109-88	3 days: 22.7 7 days: 29.0	3 days: 23.0 7 days: 29.2	3 days: 22.0 7 days: 29.6	3 days:12.4 7 days:19.3

Table 3.7: the gradation of the fine aggregates

Sieve No. (mm)	**Sieve Size (mm)**	**Cumulative percentage passing**
No. 4	4.75	99.25
No. 8	2.36	96.15
No. 16	1.18	86.10
No. 30	0.6	63.40
No. 50	0.3	22.65
No. 100	0.15	3.75
No. 200	0.075	0.75

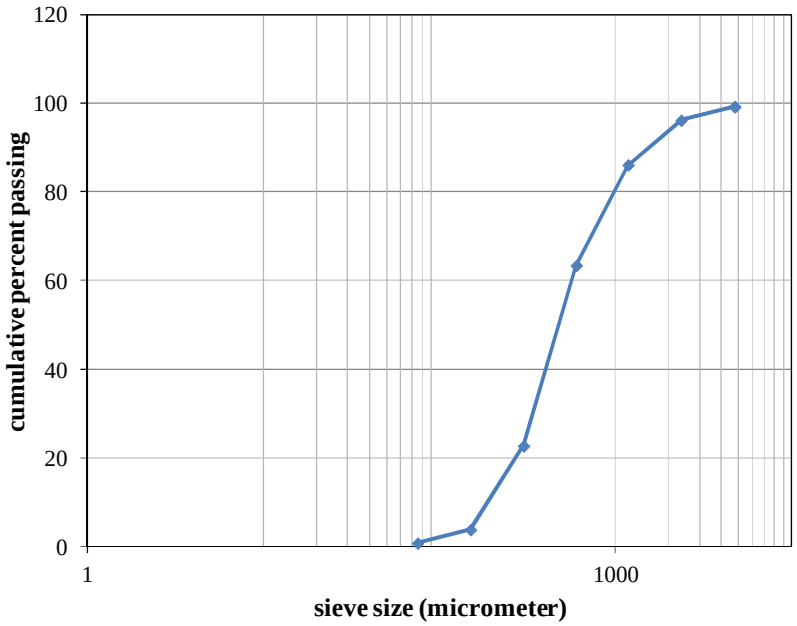

Figure 3.1: Sieve analysis results of the fine aggregate

Table 3.8: The characteristics of fine aggregates

Fineness modulus	3.28
Specific gravity	2.6
Absorption	0.81%

3.4.3 Silica Fume

To improve the strength of the mortar, condensed silica fume was used to partially substitute cement. Silica fume was obtained locally in 50 kg bags from the Egyptian Ferroalloys Company (EFACO). Based on the results of the previous research (Korany 1996) and (Abdel Naby 2006), the weight of silica fume was approximately 10% of the cement weight in all mixes. The chemical composition of silica fume as obtained from the manufacturer is given in Table 3.9. A constant 9.89% silica fume was used to partially substitute cement by weight in the expanded polystyrene matrix.

Table 3.9 Chemical composition of silica fume as obtained from the manufacturer (the Egyptian Ferroalloys Company "EFACO")

Element/Properties	Contractual Limits (%)
Amorphous Silicon Dioxide (SiO_2)	Min. 92%
Carbon (C)	Max. 1%
Iron Oxide (Fe_2O_3)	Max. 1.5%
Aluminum Oxide (AL_2O_3)	Max. 1%
Calcium Oxide (CaO)	Max. 0.75%
Magnesium Oxide (MgO)	Max. 1%
Potassium Oxide (K_2O)	Max. 1.2%
Sodium Oxide (Na_2O)	Max. 0.8%
Phosphorous Pent-oxide (P_2O_5)	Max. 0.05%
Sulphur Trioxide (SO_3)	Max. 0.5%
Chloride (Cl)	Max. 0.1%
Moisture (when packed)	Max. 0.5%
Loss on ignition 750° C	Max. 2 %
Loss on ignition 950° C	Max. 3 %
Coarse particles ; $\geq$ 45 µm (No. 325 mesh)	Max. 2%
PH – value (fresh)	5.5 – 7.5
Bulk density (when packed)	250 – 350 kg/m^3
Specific surface area (m^2 / g)	Min. 15 %

3.4.4 Expanded Polystyrene

Low-density expanded and extruded recycled polystyrene was obtained commercially from the Chemicals for Modern Building International (CMBI) Group with the brand name "Addipore 55" which is a mix of crumbles and shreds of different size, density and color as shown in Figure 3.2. The following is the manufacturer published information about the product:

Description: expanded polystyrene beads of non uniform shape (non spherical).

Size: the minimum size is 2.38 mm and the maximum size is 19 mm

Specific Weight: 20 - 22 kg/m^3

Water Absorption: 2.7 %

Gradation analysis was done on three randomly selected "Addipore 55" bags. The average of the percentage of "Addipore 55" particles retained on various sieve sizes is presented in Table 3.10 and Figures 3.2 a, 3.2 b, and 3.3. The table also illustrates the percentage prevailing of each "Addipore 55" particle shape.

Table 3.10: Average "Addipore 55" gradation as taken from a sample of three bags

Seive size (mm)	Percent Retained	% Flakes	% Crumbles	% Twirls
19.05	0.87%	3.57%	69.80%	26.63%
12.7	19.60%	35.14%	43.56%	21.29%
9.52	20.93%	46.48%	31.25%	22.27%
4.75	23.36%	34.27%	46.82%	18.90%
2.38	19.71%	11.83%	77.82%	10.35%
dust *	15.53%	dust *	dust *	dust *

Figure 3.2 a: EPS particles of different shapes and color

Figure 3.2 b: EPS as they occupy 1000 cc cylinder in proportion of gradation

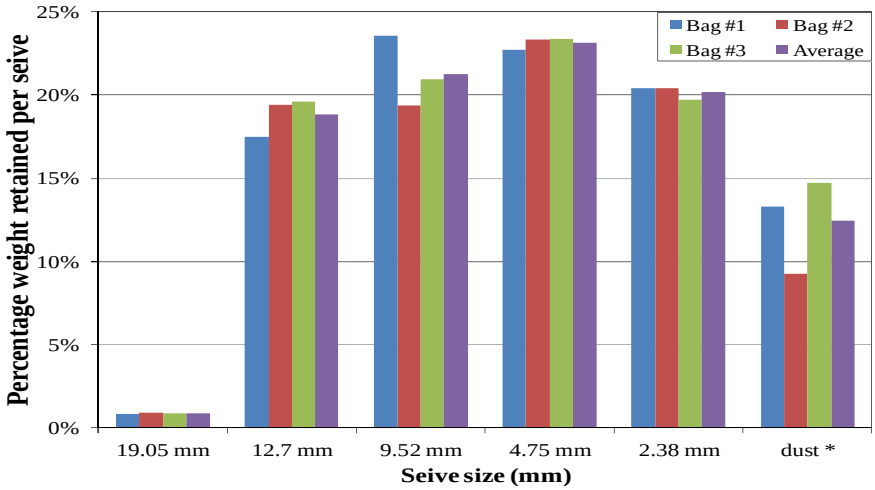

Figure 3.3: gradation of the "Addipore" samples

3.4.5 High Range Water Reducing Admixture (HRWR)

High range water reducing admixture (HRWR) was used to improve the workability of the mortar mixes. The commercial name of the admixture is "Sikament 163M" and was obtained from Sika industries. It is a chloride-free super plasticizer with a synthetic type dispersion base and density of 1.200 ± 0.005 kg/l in 20 degrees Celsius. According to the manufacturer, Sikament 163 M induces up to 3% air bubbles in concrete when it is used. The formed air bubbles were of a defined spherical shape and were distributed both in the mortar matrix as well as the surface of the prepared specimens as illustrated in Figure 3.4. The admixture dosage ranged between 1.5% and 2.5% of the weight of the cementitious materials. The optimum dosage, Table 3.1, was the one that produced flowable mix and facilitated the casting process of the blocks.

High range water reducing admixture (HRWR) was proportioned in kg/m^3 of the mix to achieve a slump of 20 cm. However, Table 3.1 shows that there was not a specific trend of increase or decrease of HRWR with EPS content in the mix. This is because the HRWR varied according to the following factors: 1-quantity and size distribution of EPS aggregates (and also sand content), 2-ease of casting EPS mortar in narrow spaces in reinforced hollow blocks, 3- time taken to cast the hollow blocks through which the mix should maintain its workability and not harden.

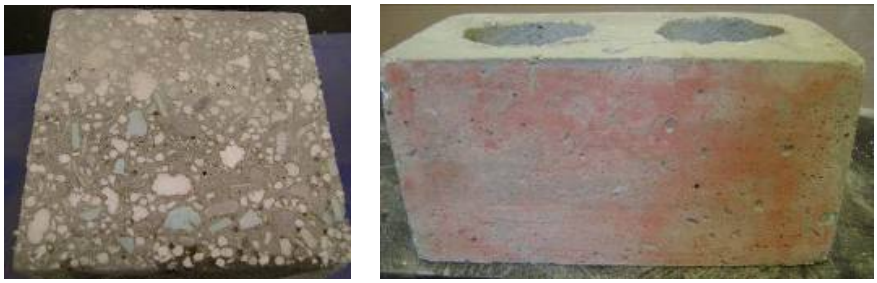

(a) (b)

Figure 3.4: the shape and distribution of the HRWR induced air bubbles in the mortar matrix appear on the surface of (a) grinded cube cross section and (b) on the block's surface

3.4.6 Block Reinforcement

a) Wire Mesh Reinforcement

Galvanized wire mesh is used for reinforcing the thin webs of the hollow expanded polystyrene mortar blocks and the control ones. The diameter and spacing of the wire mesh

are presented in Table 3.11. The yield and ultimate strengths of the wire mesh tested by Gaafar, 2004, who did previous research on the same type of wire mesh in previous research, are presented in Table 3.12. Values of minimum yield strength and effective modulus of elasticity of the welded wire mesh as obtained from ACI 549.1R-93 guide for the design, construction, and repair of ferrocement are also included in Table 3.11

Table 3.11: Specifications of Galvanized wire mesh as obtained from Gaafar, 2004.

Galvanized Wire Mesh	Data
Wire spacing	12.7 mm X 12.7 mm
Wire diameter	0.8 mm
Yield Stress (Gaafar, 2004)	490 MPa
Ultimate Strength (Gaafar, 2004)	570 MPa
Minimum Yield Strength (ACI 549.1R-93)	450 MPa
Minimum Effective Modulus of Elasticity (longitudinal) (ACI 549.1R-93)	200 GPa
Minimum Effective Modulus of Elasticity (transverse) (ACI 549.1R-93)	200 GPa

b) Fiber Mesh Reinforcement

Alkali resistant fiber glass mesh was used for reinforcing walls of the EPS hollow blocks and the control ones. The GFRP mesh was imported from Italy by a local distributor. The specifications of the fiber mesh as obtained from the manufacturer are given in Table 3.12.

Table 3.12: Specifications of Fiber glass mesh as obtained from the Manufacturer (GEOX)

Composition	Fiberglass	Approx. 84%
	Alkali resistant finish	Approx. 16%
Weight SP 04/02/12 (ISO 3374)	Raw mesh	75 g/m^2 +/- 5%
	Finished mesh	90 g/m^2 +/- 5%
Mesh width (SP 04/02/12)	Measured between yarn	Approx. 4X5 mm
Tensile Strength	Warp	Average value 1450 N/5
	Weft	Average value 1550 N/5
Elongation	Warp and Weft	4.5 % +/- 1

3.5 Specimen Preparation

3.5.1 Casting and Curing Conditions of the EPS Mortar (EM) Specimens

The OPC, silica and sand were given a dry rotation in the planetary drum mixer. The HRWR was added to the mixing water and then added to the dry mix in the mixer. A homogeneous

mortar was reached before adding the “Addipore 55” to mixer while rotating for several minutes (3 to 5 minutes). Because the EPS particles tend to float, mixing was done on stages each comprised hand stirring and mixing till homogeneity was reached as shown in Figure 3.5. The average slump obtained was 200 mm as illustrated in Figure 3.6.

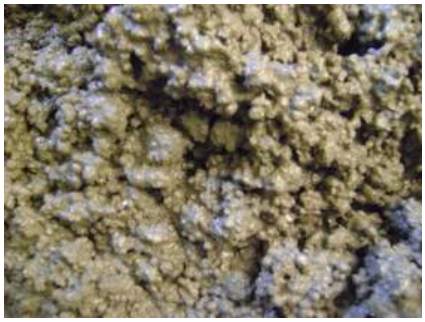

Figure 3.5: A shiny dark gray mix indicated good homogeneity and workability

Figure 3.6: HRWR enhanced workability up to a 200 mm slump

The homogenous mix was then poured in moulds placed on the vibrating table which is turned on maximum vibration. The vibrating table was used to get rid of the air bubbles formed due to the addition of the HRWR. The EM specimens were removed from moulds after 48 hours and cured in the curing room till tested.

3.5.2 Casting and Curing Conditions of EPS Mortar Hollow Blocks (EPS MU)

The moulds were specially designed and manufactured. A set of 12 moulds were manufactured of 2 mm thick steel and had internal dimensions of 200x400x200mm. Wire and

fiber meshes were formed into cages and loops respectively of dimensions 175x375x190mm. PVC pipes were cut into pieces of 250 mm length.

3.5.2.1 Wire Reinforced Blocks

The wire mesh and the PVC pipes were secured in place inside the mould as shown in Figure 3.7 and the inside of the moulds as well as the PVC pipes were covered with oil. The moulds were placed on the vibrating table. The EPS mortar was poured to fill the mould. The vibrating table was operated. An EPS mortar cover of at least 200 mm was ensured during casting. The PVC pipes were kept in place for 2 hours then removed as shown in Figure 3.8. The excess EPS mortar was removed and the surface was leveled, Figure 39.

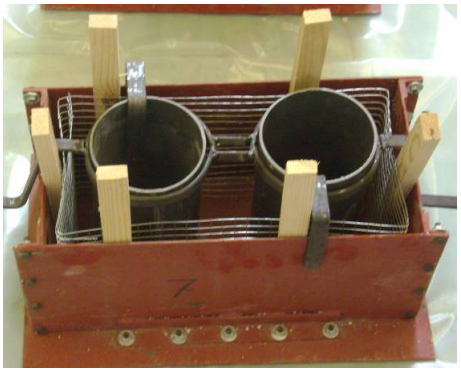

Figure 3.7: The wire reinforcement arrangement inside the block before casting

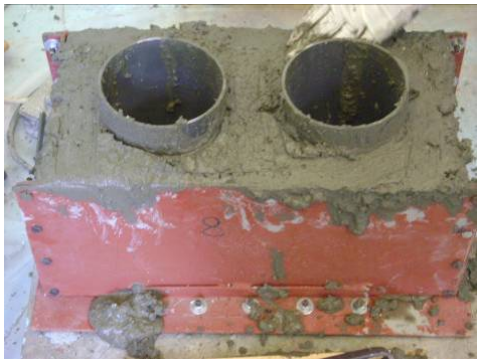

Figure 3.8: The blocks after casting the EPS mortar and before removing the PVC pipes

Figure 3.9: The blocks after removing the PVC pipes and leveling the surface

3.5.2.2 Fiber reinforced bricks

Due to the nature of the fiber mesh fabrics, the fiber mesh were wrapped around specially fabricated steel wire cage to form a hoop of dimensions 175x375x190mm as shown in Figure 3.10. The fiber loop was then stripped off the steel cage. The casting procedure was the same

as for wire reinforced blocks with the steel wire replaced by the fiber mesh hoop. The fiber mesh was maintained in place manually and by the wooden spacers likewise the steel mesh.

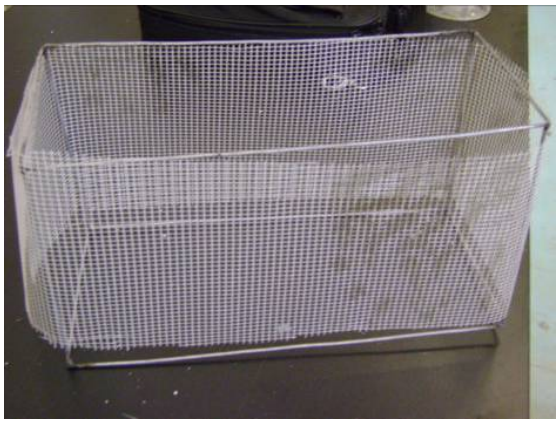

Figure 3.10: A schematic of the fiberglass hoop used to reinforce the blocks

3.5.2.3 Plain Blocks

The same moulds and casting procedure was used to cast the plain blocks but without placing any reinforcement in the block.

All types of blocks were removed from moulds after 48 hours and were cured in the curing room for 28 day then were removed to dry freely in the laboratory conditions before testing.

3.6 Test Program

Three types of tests are performed, mechanical tests, durability tests and thermal conductivity tests. The test specimens shape and number are presented in Tables 3.3 and 3.4. The mechanical tests are conducted first on EPS mortar cubes and cylinders and comprise compressive strength, static modulus of elasticity, stress-strain curve plotting and split tensile tests. Also failure pattern is reported and analyzed. These tests aimed at exploring the mechanical properties of the EPS mortar and deciphering its behavior as a material. The second batch of mechanical tests is done for assessing the compressive strength of single units of hollow blocks and bricks. The main aim is to test which batches of blocks and bricks comply with the ASTM and Egyptian Standards. Also, the compressive strength and failure pattern of the hollow blocks and bricks will be elaborated on in the light of obtained knowledge of the mechanical characteristics of the EPS mortars.

The durability tests are conducted solely on the hollow blocks and comprise wet-dry cycles of salt and acid exposures. The weight and strength loss will be monitored. The main aim is to determine the serviceability conditions of the proposed EPS mortar hollow blocks. Finally the thermal conductivity of the control and EPS mortar bricks is measured to be used later in developing the thermal model that estimates the equivalent thermal conductivity of all hollow blocks. This section explains the tests done in details.

3.6.1 Mechanical Tests

3.6.1.1 Compressive Strength

a) The cubes were tested for compressive strength after 7, 14 and 28 days under ELE Universal Testing Machine (UTM) of compressive loading capacity of 1000 KN at a loading rate of 8 KN/second as shown in Figure 3.11. The test complied with the British standards BS 8110. The universal testing machine is a non-automatic concrete compression/tension machine. The upper and lower platens have equal diameters of 220 mm and are assumed to be rigid. The boundary conditions of loading are friction where the loading platen and the cubes are in full contact without any lubricating or damping surface in-between. The compressive strength development with time and the 28-day compressive strength were determined for each mix, forty five cubes were tested, see Table 3.4. The results obtained from different mixes were compared to determine the effect different dosage of 'Addipore" on the mix relative to the control mix. The effect of EPS on the failure mode of the specimens was examined.

Figure 3.11: Universal testing machine testing cube under compression

b) The compressive strength of the cylinders of the samples containing EPS was determined using MTS universal testing machine while the control samples were tested using the ELE universal testing machine due to the capacity limitation of the MTS machine. The surface of the cylinders specimens was leveled by means of glass sheet immediately after casting to ensure a leveled surface and complete contact. Test was done in accordance with ASTM C39. The boundary conditions were frictional and the loading platens were assumed to be rigid.

c) The compressive strength of the EPS mortar hollow blocks was determined using the ELE universal testing machine as shown in Figure 3.12. The boundary conditions of the universal testing machine were frictionless and the loading platens were assumed rigid. Friction-reducing loading platens were obtained by applying soft-capping and rubber pad. The surface finish of the block was rough as shown in Figure 3.13. As a result, soft capping was implemented during testing as illustrated in Figures 3.14. The polymer grout cap was made out of modified mortar. Latex based bonding agent commercially known as 'Addibond 65' was added to replace 1/3 of the mixing water of the mortar mix of proportions 1:1 fine sand to cement and w/c ratio of 0.35. Accelerating agent obtained commercially known as 'Sika Rapid' was used to accelerate the process of cap hardening

and strength gaining. Friction-reducing systems were applied to the block by means of soft rubber cap of 20 mm thickness and dimensions of 250 mm X 450 mm. The blocks were tested under compression up to failure and the cracking during the test were visually detected. The effect of capping ensured that the stresses are uniformly distributed over the surface area of the hollow block. However, capping exerted some lateral confinement to the lateral dilation of the loaded area of the hollow block. It was noticed that capped specimens exhibited inclined cracks which indicate ductility but uncapped specimens exhibited more spalls and lateral dilation of the upper portion of the hollow block—underneath the loading platen. This is explained in details in Chapter 4.

Figure 3.12: Test setup for the EPS mortar hollow blocks

Figure 3.13: EPS Block before capping

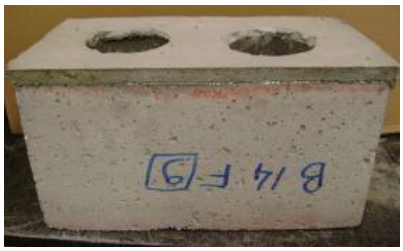

Figure 3.14: EPS Block after capping

d) The compressive strength of the EPS solid bricks was determined using ELE Universal testing machine after 28 days of wet curing. The boundary conditions were frictionless system and rigid steel platens. The frictionless system was obtained by using rubber pad between the loading platen and the test specimen.

3.6.1.2 Stress-Strain Relationship and Static Modulus of Elasticity

The stress-strain relationship was determined for the mortar using the cylindrical specimens. The MTS was used to test all EPS mortar cylindrical specimens to ensure that the strains resulting from the ductility of the mixes were properly registered. The MTS had a compressive capacity of 500 KN and was connected to a data acquisition system in the form of a PC. The test was strain-controlled, conducted at a constant strain pace, and was terminated by the collapse of the cylinder; therefore, the post-peak stress-strain relationship was determined. Some of the cylinders were capped while others were just grinded to ensure full contact with the loading head. Soft capping was done by latex mortar and not sulfur because the latter requires to be cast by heating it above 100 degrees Celsius which is not suitable for EPS particles that is known to shrink at about 70 to 100 degrees Celsius. Accordingly, sulfur capping would have altered the EPS mortar properties at the top and bottom of the test specimens. Capped specimens suffered from inclined cracks while grinded specimens exhibited more spalling and lateral dilation. The boundary conditions were frictional and the loading platens were assumed to be rigid. The test setup is shown in Figure 3.15. A total of forty cylinders were tested, refer to Table 3.4. The stress-strain relationship was determined directly from the readings of the data acquisition system attached to the MTS universal testing machine.

Figure 3.15: Test setup for the determination of the stress-strain relationship

The obtained stress-strain relationship from the MTS tests showed some initial slippage due to initial deformation of the specimen under the loading head. The stress-strain relationship of the control cylinders was also determined using different test arrangements

using compressometer. Due to limitation of the capacity of the MTS, The stress-strain relationship of control mix was determined only by using this test arrangement.

The compressometer was used also to accurately measure the static modulus of elasticity of the control and all EPS mortar mixes due to limitations that are explained in detail in Chapter 4. The cylinders were fitted with a compressometer accessory for determining the stress-strain relationship and the static modulus of elasticity according to ASTM C 469-02. The compressometer consisted of two yokes that form a gage distance of 150 mm as shown in Figure 3.16. The change in the length, shortening, was determined from the reading of the dial gage fitted between the two yoke as shown in Figure 3.16.

Figure 3.16: The test cylinder fitted with the compressometer

The cylindrical test specimens were loaded in compression using the ELE universal testing machine. The loading rate is maintained at minimum rate by gently tapping the loading lever. Strain measurements were obtained at increments of 10 KN for the control, EM10 and EM15 specimens till failure. The EM20 specimens' strain measurements were obtained at increments of 5 KN and the EM26 at 2 KN. The post peak stress-strain values of the control cylinders were not possible to measure due to limitations in instrumentation as this test is load controlled.

3.6.1.3 Splitting Tensile Strength

The ELE universal testing machine was used to determine the splitting tensile strength in accordance with ASTM C 496-96 as shown in Figure 3.17. A regression relation was developed to correlate the splitting tensile strength of each mix to its compressive strength as will be explained in Chapter 4.

Figure 3.17: Test setup for the Splitting tensile strength tests

3.6.2 Durability Assessment

The set of experiments adopted to assess the durability of the proposed EPS mortar blocks are presented in this section. The importance of the tests, measurements obtained from each test, as well as deterioration appraisal is also highlighted. The specimens tested are the different types and weights of EPS hollow blocks as illustrated in Table 3.4. The EPS hollow blocks are composite building units and the evaluation of its physical performance is based on the interaction of the blocks' components when subjected to a certain environmental aggression. It is merely unrepresentative to assess the deterioration of each of its components individually because the extent of the deterioration of one of its components when subjected to a certain aggression might be slowed down when another component is introduced, or vice versa. Also, the physical evaluation available in some of the standards, such as the Egyptian standards and ASTM, state the acceptable performance of the tested unit rather than that of the constituent material.

3.6.2.1 Absorption

Water absorption is an indirect and fast method to determine the permeability of materials. It is a well known parameter to indicate the durability and serviceability of concrete masonry units as indicated in ASTM-C90 and C129. The importance of assessing the absorption of hollow blocks is to consider their susceptibility to deleterious material migration inside the

pores. Deleterious material transported by the absorbed water varies from mild/aggressive salt solutions to mild/aggressive acids which react with the hydration products especially the portlandite ($Ca(OH)_2$).

Also, an immediate outcome of knowing the absorption percent of the EPS hollow blocks is to assess the water cement ratio and amount of water necessary for the joint mortar, render mortar and pre-wetting procedures respectively.

The absorption test was conducted on the control and EPS mortar hollow block specimens according to the guidelines provided by ASTM C642, but with some deviation. The dry mass of the hollow blocks was measured for blocks that were stacked in dry room conditions. The provisions of ASTM C642 require the dry mass to be oven dry mass after subjecting specimens to 100 or 110 degrees Celsius for 24 hours. This procedure was not followed because EPS wastes shrink and evaporate at about 70 degrees Celsius. Therefore, the 48-hour water absorption was calculated based on air-dry mass rather than oven-dry one.

The blocks were weighed in their dry state then were immersed in fresh water for 48 hours then weighed wet. The difference between the weights of the block at the two conditions was calculated and hence the percent absorption determined.

3.6.2.2 Acid/Sulphate Attack

One of the most common and detrimental chemical attack is caused by sulfate salts and acids (ACI 201.2R). It is rather rare that acids would be poured on the EM blocks, so the exposure would take place in the presence of an acidic solution. Sulphuric acid is not abundant naturally and exists only in a polluted or aggressive environment. Sulphurous gases resulting from fuel combustion react with moisture and form sulphuric acid (ACI 201.2R). Some types of soils such as peat, alum and clay contain iron sulfide (pyrite) that form sulfuric acid upon oxidation (ACI 201.2R). The deterioration of concrete due to acid attack can be achieved by using any kind of acid. The ACI 201.2R committee assessed that a PH level below 3 forms an aggressive acidic environment towards concrete. A detrimental acidic exposure is a combination of a PH level lower than 3 and in the form of ponding exposure (ACI 201.2R).

Selecting sulfuric acid to simulate an aggressive chemical attack is mainly because of two major reasons:1) it has a rapid chemical attack on concrete at ambient temperature and 2) it causes a double action of acid attack and sulphate salt attack (ACI 201.2R). Acid exposure in

the form of ponding of the EPS and control hollow blocks was selected because it is an additional factor that accelerates the attack (ACI 201.2R).

The blocks were immersed in 5% diluted sulfuric acid solution. Commercial sulphuric acid that contained impurities was bought from local chemical factories with concentration 98-99% and was added to water to produce 5% diluted. Four cycles of wetting and drying were performed. Before the start of the experiment, the blocks were weighed to obtain their initial dry weight. In each cycle, the blocks were immersed in the acidic solution for 4 days, and then removed. The wet weighed was measured and the blocks were left to dry in lab conditions for 3 days. The dry weight was measured before the blocks were immersed in the acidic solution to start the next cycle. The total test took four weeks of dry and wet cycles. The PH of the acidic solution was checked to ensure an aggressive acidic environment using a PH digital reader in the AUC environmental engineering laboratory. The PH ranged between 0.6 and 0.8 which indicates strong acidic environment (Fattuhi and Hughes 1988). During testing, the percent weight loss due to leaching was registered. At the end of the test, the blocks were tested in compression under the universal testing machine to determine the percent strength loss. The apparent degradation of the blocks throughout the four cycles was observed and recorded.

The effect of this aggressive environment on the blocks was evaluated in the form of:

1. Percentage of the weight loss at the end of each cycle. (quantitative)
2. The deterioration signs of the blocks at the end of each cycle as determined by visual inspection. (qualitative)
3. Percentage of compressive strength loss at the end of the four cycles. (quantitative)

3.6.2.3 Sea Water (Soluble Chloride) Attack

By far, the chloride ingression in porous materials is the most complicated kind of deterioration because chloride ions affect the three components of the proposed EPS blocks: cement mortar, wire mesh and fiber mesh in a series of chemical and physical reactions that are responsible of the subsequent strength loss and aesthetic degradation.

Salt attack is present in two ways according to ACI 201.2R, physical salt attack and soluble chloride attack. Physical salt attack occurs in the presence of salts that are precipitated over the surface and in the interior pores of concrete. It is present in soil, especially from ground

water. Also, building envelopes in coastal areas where they are subjected to sea water splash and airborne chloride ions would cause salt migration and deposition on the surface of the building envelope. Porous bricks are subject to efflorescence deterioration. Many brick faces and rendering layers (spatter dash) show this behavior (Lubelli and Rooij, 2009). Salts precipitated inside the pores of concrete cause the formation of crystallization pressure that result in the formation of cracks and efflorescence (Spragg et al, 2011). Deterioration induced by physical attack by sodium chloride resembles the deterioration induced by freeze-and-thaw cycles (ACI 201.2R).

The simulation of such attack is done by subjecting specimens to wet-and-dry cycles of saline attacks (Spragg et al, 2011) which is used in the present investigation. The test blocks were immersed in saturated saline solution of fine pure salt brought from saline lakes in Alexandria (El-Max Salines). Sodium chloride was selected to produce the saturated saline solution to serve both purposes: high alkalinity for fiber glass abrasion and passive film attack for steel corrosion.

Four cycles of wetting and drying were performed. Before the start of the experiment, the blocks were weighed to obtain their initial dry weight. In each cycle, the blocks were immersed in brine for 7 days, and then removed. The wet weigh was measured and the blocks were left to dry in lab conditions for another 7 days. The dry weight was measured before the blocks were immersed in the brine to start the next cycle. The weights of blocks were registered to assess the salt water absorption. The total test took eight weeks of wet and dry cycles. The salinity of the brine was checked by making sure of the presence of salt particles precipitating in the bottom of the testing container as a sign of full saturation (super saturation). At the end of the test, the blocks were tested in compression under the universal testing machine to determine the percent strength loss. The blocks apparent degradation was assessed.

The deterioration of the blocks was evaluated in terms of:

1. The loss of aesthetics of the blocks due to efflorescence and rust stains
2. The loss of water permeability due to chloride binding and precipitation
3. The gain in hollow block mass due to chloride crystallization (precipitation)

4. The loss in compressive strength due to salt crystallization in mortars, wire mesh corrosion and fiber glass leaching

3.6.3 Thermal Conductivity Assessment

Thermal conductivity of the EPS mortar was determined using the hot wire method. The ASTM C1113 defines the function of the hot wire method as to assess the thermal conductivity (k-value) of non-carbonacious and dielectric refractories. The hot wire apparatus allows determining the k-value over a wide range of temperature starting from room temperature to 1500 degrees Celsius.

3.6.3.1 Test Apparatus

The test apparatus used was UNITHERM TM Model 3141, a hot wire type thermal tester produced by Anter Corporation, Pittsburgh, PA. USA. The test apparatus is illustrated in Figure 3.18. The measurements were transmitted and displayed in a readable format simultaneously by means of proprietary software stored on the data acquisition system, Figure 3.18. The tests took place in the Ceramic and Refractory Materials Laboratories at The Central Metallurgical Research & Development Institute (CRMDI).

Figure 3.18: UNITHERM TM Model 3141 thermal conductivity tester

3.6.3.2 Test Specimens

The five mortar mixtures used in this research were tested for determining the coefficient of thermal conductivity (K). The two temperatures that resemble high and extreme noon time temperature in desert areas were selected to be 50 and 70 degrees Celsius. The average thermal conductivity of the specimens was measured at the two consecutive temperatures. The thermal tester was programmed to measure the average K-value at two temperature points in sequence and per a sole run.

Because of the limitation of the test apparatus size, the test specimens were in the form of brick shaped with dimensions 235x115x65 mm as shown in Figure 3.19. The average thermal conductivity (K) was measured of an assembly of the two bricks, stacked on top of each other in a column assembly, of the same mix to minimize the error that may be encountered due to deviations in the physical properties within the population of each mix such as weight, density, and EPS particle distribution.

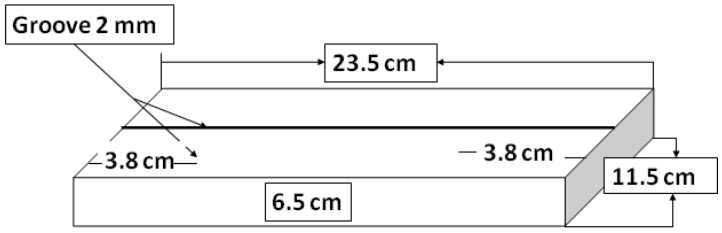

Figure 3.19: A schematic diagram of the tested specimens the thermocouples.

3.6.3.3 Specimen Preparation

The test specimens had to be prepared before being properly inserted in the thermal tester as follows:

1. During the specimen casting process, the top and bottom surfaces of the bricks were accurately leveled by means of a trowel or a glass plate.
2. Two bricks from each mix were prepared so that their surfaces are intact when they are put on top of each other; this was achieved by leveling the surface of the bricks by glass sheet immediately after casting the mixes in moulds.
3. To house the thermocouples, grooves had to be chiseled in one of the two bricks. One groove ran on the surface of the brick along its length (235 mm long) while two other grooves ran across the width from mid-width to the edge (55mm in length). The positions of the grooves were traced by a marker as shown in Figure 3.20 a. The three grooves were manually chiseled using a threaded screw and a wooden hammer, due to the frailty of the EPS mortar, to a width of 5mm and depth of 3mm as shown in Figure 3.20 b.
4. The powder resulted from the chiseling process was carefully maintained and stored in a Petri glass. The large debris resulted from the chiseling process were ground using a ceramic bowl and grinder and stored in the Petri glass as seen in Figure 3.20 c.

5. The grooved brick was placed in the thermal tester and the thermocouples were carefully and firmly inserted in the grooves as shown in Figure 3.20 d.
6. The second brick was placed on top of the grooved brick and full contact was ensured between the thermocouples and the two bricks as shown in Figure 3.20 e.
7. The lid of the thermal tester was firmly closed and the test commenced

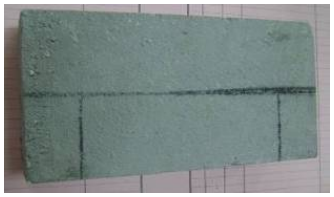

a) : Marked locations of the grooves

b) : Engraving the grooves

c) : Grounding the debris resulting from engraving the bricks into powder

d) : Filling the grooves with the brick powder

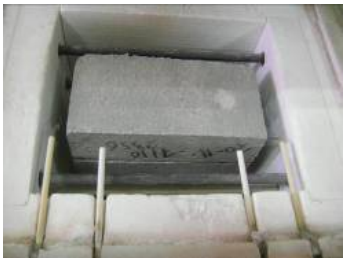

e) : The two-brick assembly inside the tester

Figure 3.20: Procedures adopted for specimen preparation prior to test commencement

3.6.3.4 Experimental procedures

Steady state thermal testing was conducted on each sample size at the two different temperatures. The two brick assembly was positioned in the thermal tester and the test was adjusted to record and calculate the k-value at 50 and 70 degrees Celsius. The sample was heated to reach 50 degrees then the first k-value was calculated by the software when steady state (thermal equilibrium) was reached. Afterwards, the sample was again heated to reach

70 degrees Celsius than the second k-value was calculated by the software when the steady state was reached. All the processes were automated and were done one shot. Each steady state was reached in more or less 7 to 8 hours and each brick assembly took approximately one days for the k-value to be calculated by the thermal tester's copy righted software registered on the data acquisition system—PC. After the termination of the test, a table and a plot were generated by the registered software that related the temperature at the steady state condition and the corresponding k-value.

Chapter 4

Results and Discussion

4.1 General

The experimental test results in terms of Mechanical properties of EPS Mortar and EPS blocks and bricks, the durability, and the thermal characteristics of the of the EPS mortar as determined from the experimental thermal tests of the EPS bricks are presented and discussed in this chapter. The thermal characteristics of the EPS hollow blocks are determined numerically using computer modeling and are presented and discussed in Chapter 5

4.2 Mechanical and Physical Properties of EPS Mortar

4.2.1 Density of Hardened EPS Mortar

The density of EPS mortar is the main parameter in this research. The change in the density of the EPS is derived mainly from partial substitution of sand with EPS particles. Table 4.1 presents the average densities of 15 mortar cubes of dimension150x150x150mm of each mix. The table also shows the standard deviation of the population cast based on the assumption that the population follows a normal distribution as well as the percentage reduction in the density as a result of increasing the EPS weight/m^3.

Table 4.1: EPS content and corresponding density and density reduction for each mix

Mix	EPS Content (kg/m^3)	Average Density of the Test Cubes (kg/m^3)	Standard deviation (kg/m^3)	Density Reduction%
Control	0	2138	45.9	0
EM10	10	1726	72.7	19.3
EM15	15.1	1553	64.1	27.4
EM20	20.4	1268	37.8	40.4
EM26	26.2	970	16.9	54.6

As shown in Table 4.1, the inclusion of EPS wastes tremendously reduced the density of the mortar. The addition of 10 kg of EPS wastes reduced the mortar density from 2138 kg/m^3 to 1726 kg/m^3, which represents a reduction of 19.3%. The highest density reduction was recorded by the inclusion of 26.2 kg of EPS wastes which reduced the density to 970 kg/m^3 or a reduction of 54.6%. The reduction is due to the fact that EPS aggregates are ultra-light

and occupy large space; the average density of EPS particles is 22 kg/m^3 with a maximum particle size of 19 mm.

The EPS mortar density varied significantly within the batch as indicated by the standard deviation shown in Table 4.1. This variation could be attributed to the poor gradation and shape of the EPS particles in addition to the segregation of aggregates that was observed during mixing especially in the mix with the lowest EPS content. The phenomenon of segregation was slightly reduced by proportioning the amount of HRWR; moreover, constant mixing was always applied even during casting to ensure that all scoops of EPS mortar uniformly contained EPS particles and mortar matrix. The segregation problem and the proposed methods of its mitigation were reported in the literature by several investigators (Perry et al, 1991; Ravindrarajah and Tuck, 1997; Abdulkadir and Demirbog, 2009) as was mentioned in Chapter 2. It was noticed during the casting of the test samples that vibration made the matter worse because it randomly dispersed the EPS and sand aggregates according to weight and accordingly the EPS particles floated at the top as they are almost weightless even when coated with mortar. Accordingly, it was decided in this research program to use sequenced vibration and hand compaction, however, variability of test results sustained.

It is also observed from the results presented in Table 4.1 that the variation in the density within the batch was reduced significantly with the increase in the EPS content. The explanation for this phenomenon is that the mix with high dosage was formed predominantly of EPS particles and by the time they got coated by the matrix, there was less cement mortar slurry to allow them to float and consequently more uniform mix was obtained.

Figure 4.1 shows the effect of EPS content per kg of the mix on the reduction of the EPS mortar density. The test data was best fitted by a linear regression as follows:

$$\rho = -44.3\ EPS_c + 2162.1$$

Where "ρ" is the dry density in kg/m^3 and "EPS_c" is the content in kg of EPS in the mix. The regression equation shows that addition of one kg/m^3 of EPS particles would decrease the density of the mortar matrix by 44.3 kg/m^3. This graph helps in future applications where it allows future researchers to try different dosage range that would produce a different density

range. On the other hand, it explains the gap that will be seen later in the strength results between the control mix and the EM10 mix.

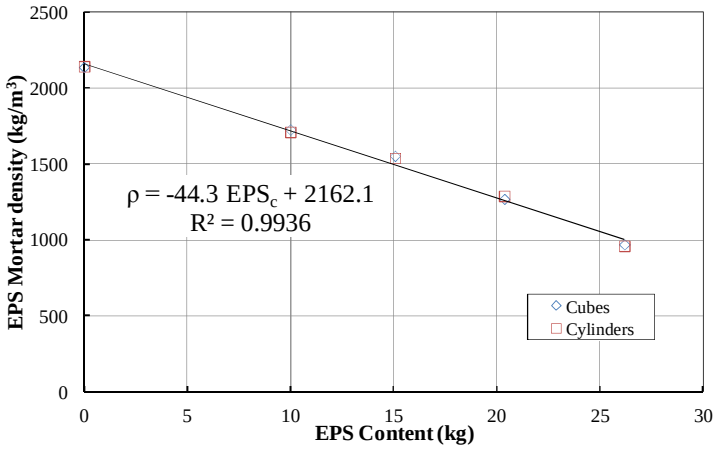

Figure 4.1: Relationship between EPS content in kg and EPS mortar density in kg/m^3

4.2.2 Compressive Strength of EPS Mortar

The most important mechanical property of proposed EPS mortar is the compressive strength. The compressive strength after 7, 14, and 28 days were determined by testing 150 mm cubes and the compressive strength after 28 days was also determined by testing 150x300 mm cylinders for all EPS mortar mixes under investigation as well as the control specimens.

4.2.2.1 Development of the EPS mortar Compressive Strength with Time

The development of the compressive strength as obtained from the cube tests of the control and EPS mortar mixes is given in Table 4.2 and Figure 4.2.

Table 4.2: The development of compressive strength of the test cubes

Mix	150 mm cube compressive strength (MPa)			28-day ratio to 7-day	28-day ratio to 14-day
	7-day	14-day	28-day		
Control	23.35	24.92	32.58	1.40	1.31
EM10	9.25	9.21	14.21	1.54	1.54
EM15	4.70	6.53	7.35	1.56	1.13
EM20	3.40	5.06	5.36	1.58	1.06
EM26	3.2	3.5	3.5	1.1	1

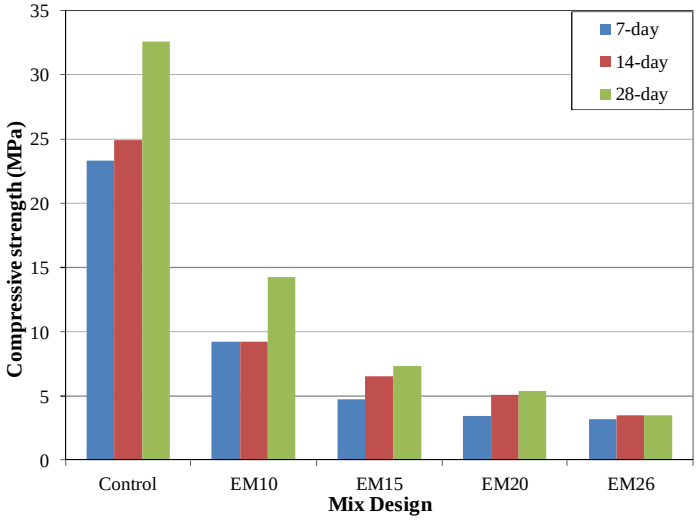

Figure 4.2: The development of compressive strength of the test cubes

Generally, the ratio between the 28-day compressive strength and the 7-day counterpart for concrete mixtures lies within the 1.3 and 1.7 range (Neville, 1981). Table 4.2 shows that the results of all test specimens fall within this range with the exception of EM26. While this ratio was 1.4 for the control specimens, it was little bit higher for EM10, EM15, and EM20 where it was 1.54, 1.56, and 1.58 respectively. It was expected for the ratio obtained by EPS mortars to be lower than that of the control's due to the effect of EPS aggregates in preserving the heat of hydration inside the cube during the hydration reactions (Tang et al, 2008). This could be attributed, generally to the curing regimen. Curing was adopted for all specimens by wet burlap which was rewetted three times a day, however, EPS mortars have high rate of moisture transmissivity (Bisschop and van Mier 2008), i.e., dry at a faster rate and the necessary water amount for proper hydration might not have been maintained by this curing regime. Therefore, it is better cure EPS mortars by soaking them in fresh water. Nonetheless, the curing regimen did not have its toll on mix EM26 because the volume of EPS was large enough to retain the heat of hydration inside the specimen.

Figure 4.2 shows that the rate of strength development is in a fast deceleration with the increase in EPS content. Table 4.2 and Figure 4.2 show that little strength development occurred after the 14-day strength for the EPS specimens. This phenomenon was also noticed by several researchers (Babu and Babu, 2003; Chen and Liu, 2004; Babu et al, 2006; Tang et al, 2008).

As for the results of EM10, this mix suffered from segregation which negatively affected the consistency and quality of its compressive strength results. This is evident from the result obtained for the 14-day compressive strength, where, for similar density the seven day compressive strength was almost the same.

4.2.2.2 28-day Compressive Strength of the Cubes and Cylinders

The experimental results for the 28-day compressive strength of the EPS mortar cubes and cylinders are given in Table 4.3. It is worth mentioning that the results tabulated in Table 4.3 are the average of 3 cubes and 3 cylinders. The relationship between the mix density and the 28-day compressive strength is given in Figure 4.3

Table 4.3: The compressive strength of EPS and control mortars cubes and cylinders

Mix	150 mm Cubes		150x300 mm Cylinders		
	Average Density (kg/m^3)	Average Compressive Strength (MPa)	Average Density (kg/m^3)	Average Compressive Strength (MPa)	Ratio of the Cylinder Strength to the Cube Strength
Control	2138	32.6	2143	26.40	0.81
EM10	1630	14.2	1710	11.40	0.80
EM15	1553	7.4	1539	6.70	0.90
EM20	1268	5.4	1288	4.50	0.83
EM26	970	3.5	982	2.65	0.76

Table 4.3 and Figure 4.3 depict a steep decrease in compressive strength with the increase of the EPS content. For the cube specimens, the first dosage of EPS wastes, EM10, decreased the density by about 24% and caused a significant decrease of the compressive strength by about 56%. The maximum decrease in both density and compressive strength was achieved by mix EM26 which is 55% and 89% respectively less than that of the control mix. The sharp decrease in strength stems from the fact that EPS particles are modelled as air voids and EPS mortars as cellular concretes (Haidar and Pijaudier-Cabot, 2002; Miled at al,2004; Bouvard et al, 2007). The vast variation between the elastic characteristics of EPS particles and the surrounding matrix may result in its indifference to the presence of EPS particles as if they

were air voids. The EPS wastes (Addipore) gradation as presented in Chapter 3 had a maximum size of 19 mm and a minimum size was 2.38 mm, the particles were in the form of irregularly shaped prismatic pieces (shreds) and oval crumbles to small beads of poor quality. The characteristics of Addipore created large pockets of negligible strength in the relatively strong mortar matrix resulting in steep and sharp decrease in the compressive strength of the composite accompanied to its first inclusion dosage.

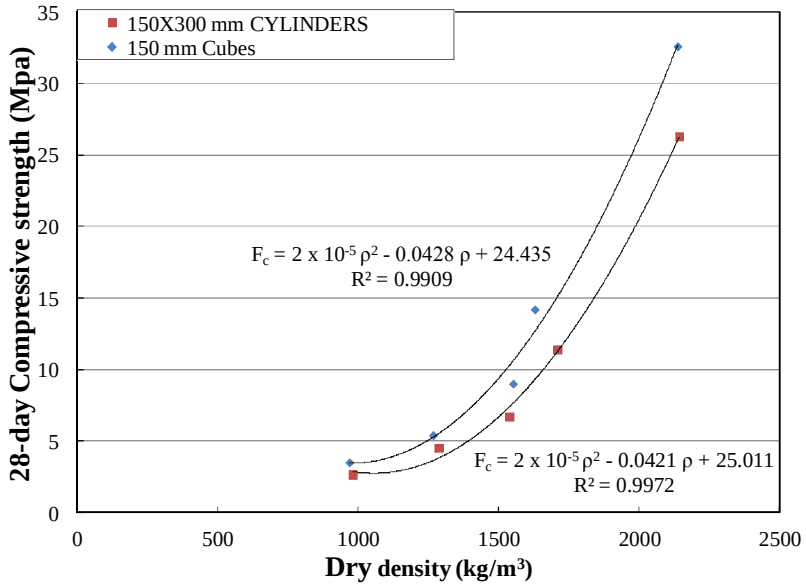

Figure 4.3: Relationship between mix density and 28-day compressive strength of EPS mortar

Figure 4.3 shows that the relation between the EPS mortar density and compressive strength was best fitted as a quadratic relation as follows:

$F_c = 2 \times 10^{-5} \rho^2 - 0.0428 \rho + 24.435$, for 150 mm cubes

$F_c = 2 \times 10^{-5} \rho^2 - 0.0421 \rho + 25.011$, for 150 x 300 mm cylinders

Where "F_c" is the compressive strength in MPa, and "ρ" is the dry density of the mix in kg/m^3. The power relation is in line with the previous research by Babu et al, 2006 and Kan and Demirboga, 2007. The obtained exponential relation between the compressive strength and EPS mortar density is a resultant of three factors: 1- the general EPS particle strength nature, 2-The specific EPS shape and size, and 3- the strength of the mortar matrix. Table 4.3

shows that the ratio of the cylindrical compressive strength to the cube compressive strength was about 0.8 for all mixes with the exception of EM15 which was 0.9.

4.2.2.3 Failure pattern of Cubes and Cylinder

The failure pattern of the cylinders and cubes is presented in Figures 4.4 and 4.5 respectively. The control mortar cylinders and cubes failed by localized inclined shear cracks. The narrow crack width may have resulted from the absence of coarse aggregates because splitting cracks are formed around the maximum size of the aggregate, which are sand particles in mortars.

On the other hand, EPS content enhances the ductility of the failure of EPS mortar cylinders and cubes which is characterized by crack initiation at lower stress than the ultimate's. The increase in EPS content results in more gradual failure that is characterized by extensive inclined cracks and spalls that was noticed on all cylinders. The lightest EPS mortar cylinders, EM26, exhibited maximum lateral dilation and sliding crack in compressible failure form.

Moreover, the inclusion of the first EPS particles produced a more ductile failure that was characterized by the dispersion of splitting inclined and sliding cracks over the volume of the cube. Lighter mixes, namely, EM15 exhibited dispersed and inclined hair cracks that indicate increase in the ductility of the EPS mortar upon failure. Mix EM20 exhibited similar shape of cracks but at a much less intensity. The lightest EPS mortar mix exhibited a rather compressible failure. Surface cracks were barely visible and were hugely dispersed.

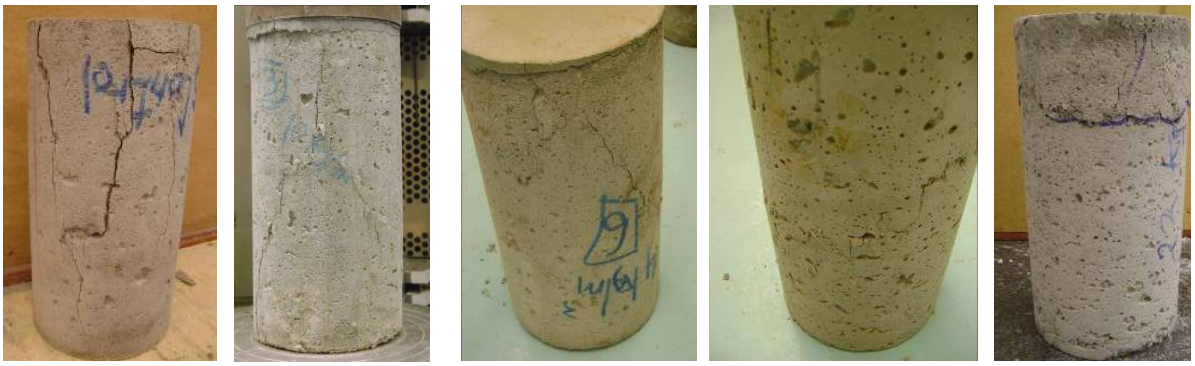

(a) Control Specimen (b) EM10 Specimen (c) EM15 Specimen (d) EM20 Specimen (e) EM26 Specimen

Figure 4.4: Failure pattern of the EPS Cylinders

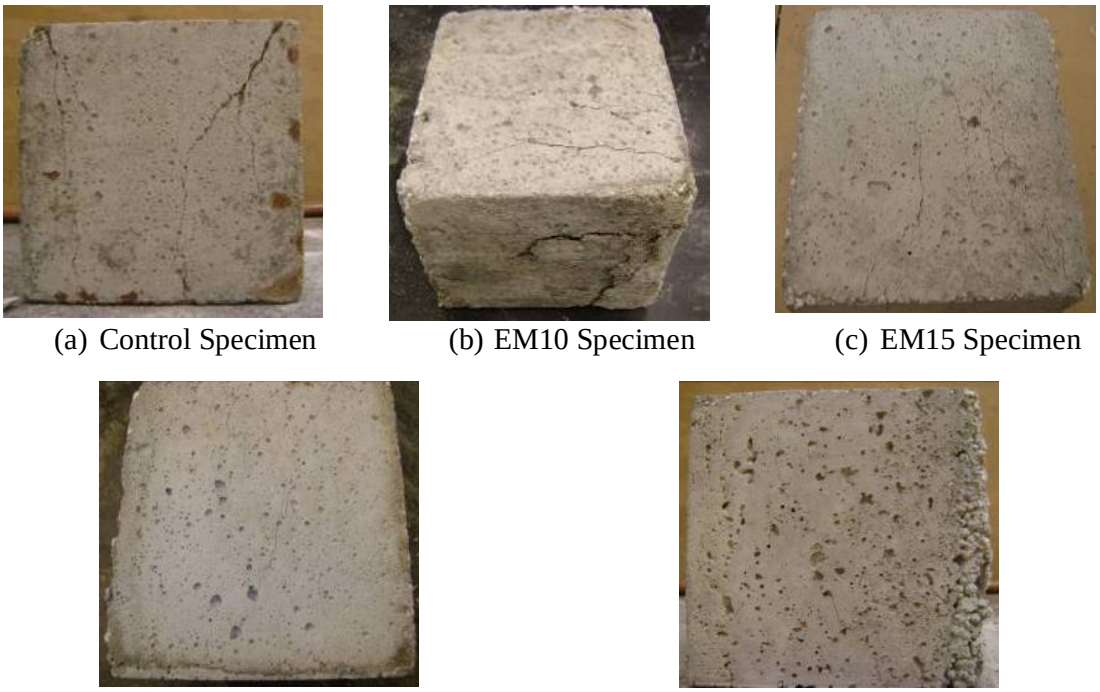

(a) Control Specimen (b) EM10 Specimen (c) EM15 Specimen

(d) EM20 Specimen (e) EM26 Specimen

Figure 4.5: Development of the ductile failure with the increase of EPS content

EPS wastes, likewise some aggregates from wastes, for example rubber tyre aggregates, do not fail. The deformability of aggregates such as EPS allowed differential dilation and lateral expansion of the mortar under compressive loading. However, the surface adherence of EPS and mortar matrix was effective just to allow mortar to gradually slide and spall but not to suddenly crush and collapse. The ductility of EPS mortar failure could be explained by the dampening (cushioning) effect of EPS particles to the further dilation of the crushed mortar that indicated ductile failure. Therefore, although EPS is assumed air voids because of its zero strength, EPS mortars have a significantly different failure pattern from that of aerated concretes.

4.2.3 Static Modulus of Elasticity

The results of the static modulus of elasticity of the five mixes are presented in Table 4.4. The values of the static modulus of elasticity of the EPS mortars of different densities ranged between 8 and 53 per cent of that of the control mix depending on the EPS content.

Table 4.4: The modulus of elasticity and splitting tensile of EPS and control cylinders

Mix	150x300 mm Cylinders			
	Test results for E		Test results for indirect tensile strength	
	Average Density (kg/m^3)	Average Static Modulus (GPa)	Average Density (kg/m^3)	Average Tensile Strength (MPa)
Control	2196	15.50	2120	2.87
EM10	1658	8.20	1762	1.46
EM15	1443	5.60	1553	1.22
EM20	1236	3.60	1320	0.78
EM26	1020	1.2	964	0.55

The decrease of the modulus of elasticity of EPS mortars with density is presented in Figure 4.6, which is best fitted with a linear regression relation according to the following equation:

$$E = 0.0122\ \rho - 11.55$$

Where E is the modulus of elasticity in GPa and ρ is the density of the mix in kg/m^3. The modulus of elasticity of EPS mortar is estimated as a combination between the moduli of elasticity of the components (phases); namely: the mortar and the EPS particles. Hence the decrease in the static modulus of EPS mortars with the decrease in density resulted from the fact that lighter mixes have lower and freer mortar body to deform. Moreover, the amount of sand in lighter EPS mortars (mortars with more EPS) decreased and resulted in richer mortars with lower E.

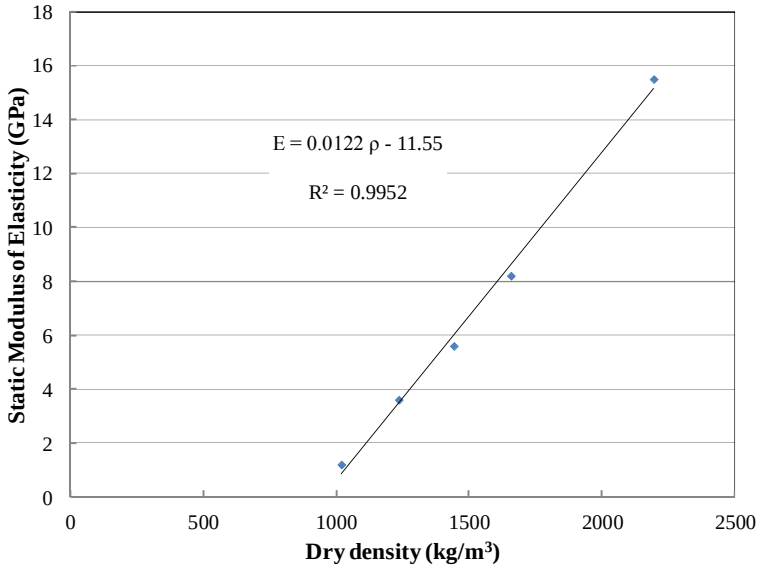

Figure 4.6: relationship between modulus of elasticity and EPS mortar density

The relationship between the static modulus of elasticity of EPS mortars and the corresponding compressive strength is presented in Figure 4.7. The figure shows that the relationship between the static modulus of elasticity of EPS mortars and its corresponding 28-day compressive strength is best fitted by a second order polynomial relation as follows:

$$E = -0.0141\ F_c^2 + 0.9916\ F_c - 0.8896$$

Where E and F_c are the modulus of elasticity in GPa and compressive strength in MPa respectively. Further, it is noticed that the compressive strength is more sensitive to the EPS mortar density variation than the static modulus. For example, the first inclusion of EPS in the mortar mix, EM10, reduced the compressive strength to 44 % and the static modulus to 53 % of that of the control mix. The different response between the compressive strength and the static modulus of EPS mortars could explain the former's volatility towards change in density.

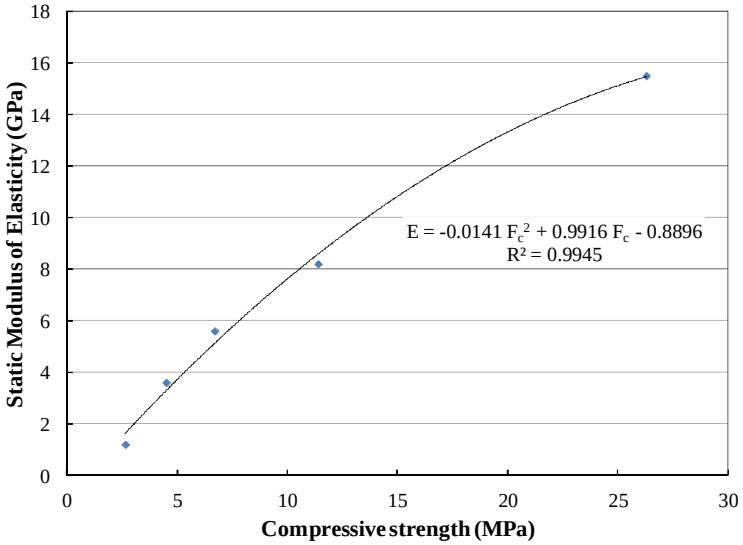

Figure 4.7: Relationship between the Static Modulus of elasticity and the 28-day compressive strength of EPS mortar

4.2.3.1 Stress-strain Curves

The stress-strain curve obtained for the control mix and the EPS mixes are presented in Figure 4.8. Comparing the stress-strain relationships of the control specimen with the EPS specimens clearly shows that the control specimen had a much stiffer relationship which implies a higher modulus of elasticity as explained in the previous section. The stiffness of the mortar was reduced by the increase of the EPS content. It is also noticed that the stress-strain curve of the control cylinders is convex and those of the EPS mortars are concave, which is intrinsic in the measuring instrument, loading rate and cycles (Bastgen and Harmann, 1977). The concavity of the curve was produced from the steady, low rate of loading adopted during testing the specimen on the MTS while the convex shape was produced from the unsteady and faster loading rate inherent in the UTM. This is why, determining the secant modulus—tangent to curve—would have been over-estimated the convex curves and under estimated the concave curves (Bastgen and Harmann, 1977). Especially that, one loading cycle was adopted in measuring the stress-strain curves, and different loading rates allowed the specimens to develop resistance at different pace that would affect the results obtained from the elastic region. As a result, the ASTM C 469 was adopted—which uses the chord method—for determining the static modulus of elasticity which does not stipulate specific loading rate or cycles in determining E. Nonetheless,

plotting the loading and defending portions of the stress-strain curve of EPS mortars might be important in interpreting its gradual and ductile failure.

The control, EM10, EM15, EM20 and EM26 had strains of 0.002, 0.0056, 0.0038, 0.0045, and 0.0033 respectively at the maximum corresponding stress. The higher strains of mixes EM10, EM15 and EM20 fits the LWA concrete stress-strain behavior explained by Neville, 1981 and Chandra and Berntsson, 2002. Similar stress-strain behavior was reported on EPS mortars by Bouvard, et al. 2007.

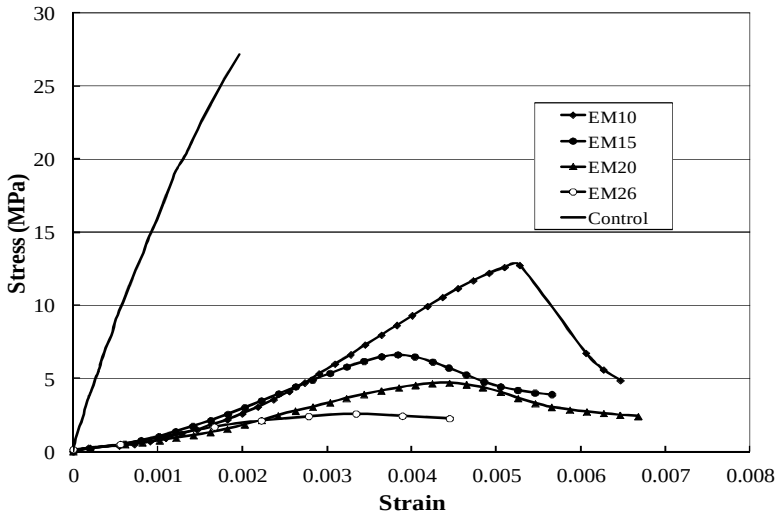

Figure 4.8: Stress-strain curves of the control and EPS cylindrical specimens

The descending part of the stress-strain curves of the EPS mortar would greatly assist in explaining the improved failure behavior of EPS mortar because it identifies the formation of unstable fissures starting close to the ultimate stress and ending by the complete failure of the specimen. Post ultimate stress, the EM10 mix exhibited sudden drop in stress that indicated loss of specimen integrity. This might be explained by the failure pattern that was characterized by the development of localized surface cracks. The macro-cracks formed released energy while the specimen was still carrying load and coalesced to produce the failure evident by the straight line of the descending curve. On the other hand, mixes EM15 and EM20 exhibited high ductility where the ascending curve was symmetrically mirrored on the descending curve. Such a shape indicates the gradual and improved failure of the EPS mortars. It also tells the development of ductile dispersed micro-cracks and spall rather than the widening of existing local cracks, which was observed during testing. The EM26 mix is a

proof of the compressibility and toughness of ultra-light EPS mortars. The descending curve was almost flat and the specimen maintained carrying 85 per cent of the maximum load till the test was terminated. The cylinder specimen was shrinking in a compressible way during loading as a sponge. Micro-fissures were noticed as a result of the loss in height (compressibility).

4.2.4 Splitting Tensile Strength

The splitting tensile strength also known as the Brazilian test is used to indirectly gauge the tensile strength of concretes and mortars. The values of the splitting tensile strength of the control mix and the EPS mortar mixes are presented in Table 4.4. The decrease in splitting tensile strength with the decrease in density is shown in Figure 4.9 and is fitted by a polynomial equation as follows:

$$F_{st} = 2 \times 10^{-6} \rho^2 - 0.0037 \rho + 2.4096$$

Where F_{st} is the splitting tensile strength in MPa and ρ is the dry density of the mix in kg/m^3. The first dosage of EPS particles decreased the splitting tensile strength by about 49% as compared to that of the control mix. The reduction of the splitting tensile strength of EPS mortar with the increase in EPS content registered 58, 73 and 81% as compared to that of the control mix corresponding to EM15, EM 20 and EM26. Evidently, the sharp drop in split tensile with the lowest EPS content is due to the little role the EPS particles had in resisting the propagation of the single crack induced by the Brazilian test. It is worth noting that the compressive strength and the splitting tensile follow the same power trend with the decrease in density.

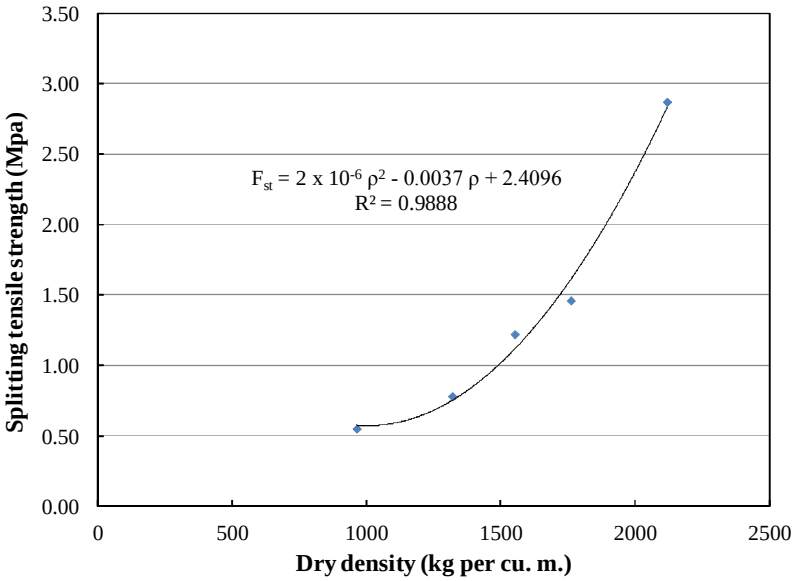

Figure 4.9: Relationship between the splitting tensile strength and the density of the control and EPS mortar mixes

The ratio between the splitting tensile and the compressive strength of the mortar specimens fell between 0.11 and 0.21 (control and EM26 mixes respectively), which conforms to the range suggested by Neville, 1981. Figure 4.10 shows the relationship between the splitting tensile strength and the corresponding cylinder compressive strength. The split tensile strength of EPS mortars increased with the increase of compressive strength. The relationship was best fitted by a linear regression as follows:

$$F_{st} = 0.0945\ F_c + 0.4005$$

F_{st} and F_c are the splitting tensile strength and the compressive strength in MPa respectively. The split tensile, like the E, is less affected by the EPS volume inclusion than the compressive strength.

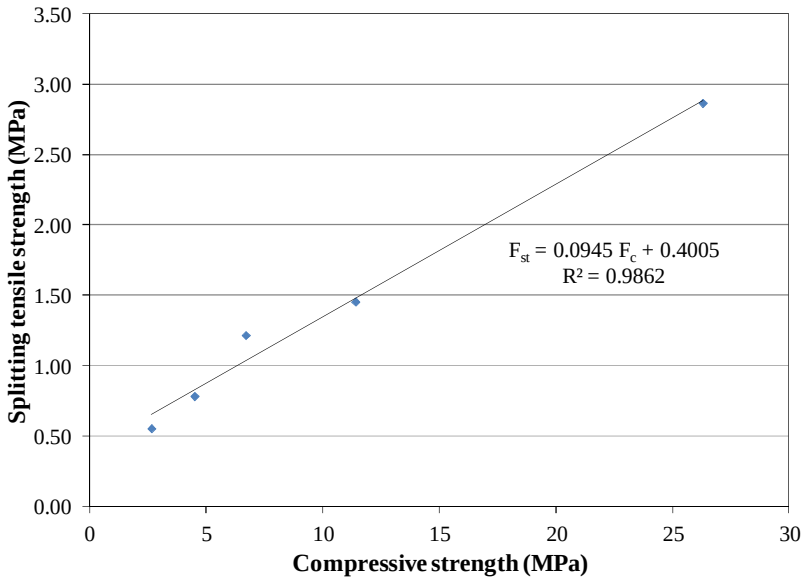

Figure 4.10: Relationship between the splitting tensile and cylinder compressive strengths of the control and EPS mortar mixes

4.2.4.1 Failure pattern

The failure of the control and EPS mortar cylinders by splitting tensile is presented in Figure 4.11. The failure of the control specimen resembled the classic splitting of the concrete into two halves by one splitting tensile crack. On the other hand, the first dosage of EPS improved significantly the failure pattern. Cylinders of mix EM10 had two brittle cracks as an impression of the loaded beam. The brittle cracks however, did not extend to the core of the specimen and were viewed as surface cracks. Lighter mixes showed longitudinal surface hair cracks along the length of the specimen. Mix EM20 and EM26 showed a pattern of compressible behaviour where longitudinal cracks were not developed in place of the loaded beam. Instead, the loaded beam left indentation of few millimetres deep which indicated energy absorption and high toughness. The split tensile failure is achieved by loading a strip with a uniformly distributed compression load P on the width of the strip which results in a homogenous stress field except for the concrete volumes close to the loaded strip (Kanos et al.). Failure occurs in the region close to the loaded strip under indirect tension by a splitting single crack. However, all EPS mortar specimens showed more than a single crack and preserved their integrity after failure which might indicate that near peak load, stresses were distributed on a wider region through successive cracking (energy release) and load redistribution (elastic straining). Assuming that the modulus of elasticity of concrete in

tension "E_t" is similar to that in compression "E_c" (Kanos et al.), the following equation could be used to estimate the tensile strain, where "F_{st}" is the splitting tensile strength and "ε_f" is the tensile strain (Kanos et al.).

$$\varepsilon_f = \frac{F_{st}}{E_c}$$

This implies that the maximum peak tensile strain increases with the increase of EPS content. For example, the maximum tensile strain of the control and EM26 as estimated by the above equation is 0.18×10^{-3} and 0.46×10^{-3} respectively. The capacity of lighter EPS mortars to retain specimen integrity comes from its higher tensile strain at peak load. Moreover, the failure of EPS mortars could be explained by the stress-strain curves described earlier. Though tensile failure is brittle and sudden, the inclusion of EPS transformed it to be gradual and ductile, similar to that of EPS mortar under compression. This entails that EPS mortar might have transformed the simple tensile failure into a complex failure like that of compression as has been shown in the failure plateau and defending leg of stress-strain curves in Figure 4.8.

(a) Control Specimen (b) EM10 Specimen (c) EM15 Specimen (d) EM20 Specimen (e) EM26Specimen

Figure 4.11: Splitting failure patterns of the control and EPS mortar cylinders

4.3 Expanded Polystyrene Mortar (EPS) Hollow Blocks

4.3.1 Compressive strength of EPS Hollow Blocks

The compressive strength of the EPS hollow blocks are assessed in accordance with the limits set by the ASTM C 90, ASTM C 129, and the Egyptian Standards. Table 4.5 presents the net compressive strength of the hollow blocks, which is calculated by dividing the ultimate compressive load over the area of the block less the area of two cavities (net area) and the gross compressive strength which is calculated by dividing the ultimate compressive load over the bulk area of the block (200 x 400 mm).

Table 4.5: The density, weight and strength of EPS hollow blocks

Batch	Average of Three Blocks			
	Density (kg/m^3)	Weight (kg)	Gross Strength (MPa)	Net Strength (MPa)
CBP	2119	23.5	6.6	9.5
CBW	2092	23.2	6.6	9.5
CBF	2157	23.9	6.0	8.7
EMBP10	1758	19.5	4.8	6.9
EMBW10	1910	21.2	4.7	6.8
EMBF10	1750	19.4	4.4	6.3
EMBP15	1487	16.5	2.9	4.1
EMBW15	1497	16.6	3.4	4.9
EMBF15	1408	15.6	3.4	4.9
EMBP20	1265	14.0	3.0	4.3
EMBW20	1246	13.8	3.1	4.5
EMBF20	1242	13.8	2.8	4.0
EMBP26	956	10.6	1.7	2.4
EMBW26	957	10.6	1.6	2.4
EMBF26	982	10.9	1.6	2.4

Table 4.6: The density, weight and strength of EPS solid bricks

Batch	Average of Three Bricks		
	Density (kg/m^3)	Weight (kg)	Strength (MPa)
CBR	2150	3.8	8.6
EMBR10	1679	2.9	5.9
EMBR15	1558	2.7	4.4
EMBR20	1354	2.4	3.5
EMBR26	995	1.7	2.2

The ASTM uses the net compressive strength of hollow block concrete masonry units (CMU) which specifies a minimum strength of 13.1MPa and 4.14Mpa for load bearing and non-load bearing units respectively. On the other hand, the Egyptian Standards (EOS 2005/42) specifies the required strength for solid and hollow blocks which varies with the density of the block as follows: 1) minimum strength of 7.0, and 5.6 MPa for load bearing solid blocks of low or medium density (< 2000 kg/m^3) and heavy density (> 2000 kg/m^3) respectively, 2) minimum strength of 5.0, and 4.0 MPa for load bearing hollow blocks of low or medium density and heavy density respectively, 3) minimum strength of 2.5, and 2.0 MPa for none load bearing solid blocks of low or medium density and heavy density respectively, and 4) minimum strength of 2.0, and 1.6 MPa for none load bearing hollow blocks of low or medium density and heavy density respectively. The density, weight, and strength of the EPS hollow blocks and solid bricks are presented in Tables 4.5 and 4.6. It is worth mentioning that a typical commercial concrete hollow block of dimensions 200x400x200mm was tested and the recorded results for this type were: 1) average density of 2100 kg/m^3 (heavy density), 2) weight of unit of 17.2 kg, and 3) average net strength of 5.5 MPa.

Based on the results given in Table 4.5, all EPS hollow block units, except batches made with EM26 mortar (EMBP26, EMBW26 and EMBF26) comply with the ASTM C-129 strength criteria for non-load bearing hollow blocks used for above grade and external wall application. On the other hand, while hollow blocks made with the control and EM10 mortar (CBP, CBW, CBF, EMBP10, EMBW10 and EMBF10) comply with the EOS 2005/42 strength criteria for load bearing applications, the rest of the EPS hollow block batches

comply with the EOS 2005/42 strength criteria for non-load bearing hollow blocks used for above grade and external wall application. As for the EPS solid brick, EPS solid brick batches made of EM10 and EM15 mortar complied with ASTM C-129 for similar application. On the other hand, all the EPS solid brick batches except for EMBR26 complied with the Egyptian standards for non-load bearing applications while the control batch complied with the requirements of load-bearing applications.

4.3.2 Effect of EPS Content on Density

The percent inclusion of EPS in the EPS mortar hollow blocks made from the EM10, EM15, EM20, and EM26 batches reduced the density by 15, 31, 41 and 54 per cent as compared to that of the control. The EPS bricks made from the respective batches had their density reduced by 22, 28, 37 and 54 percent compared to that of the control. The results of density reduction conform to those registered for cubes and cylinders discussed earlier. Figures 4.12, 4.13 illustrate the density and weight reduction obtained for the different hollow blocks and bricks batches. Table 4.5 shows that EPS hollow blocks made of EM15, EM20, and EM26 were lighter than the conventional concrete block available in the Egyptian market. These types of EPS hollow blocks have a unit weight below 16.5 kg and would be convenient for laborers to handle and stack.

The density and the unit weight of the EPS solid bricks followed the same pattern and reduced with the increase of the EPS content. Because of the small dimensions of the brick unit, its weight is very small as compared to the block weight which makes it more convenient in handling.

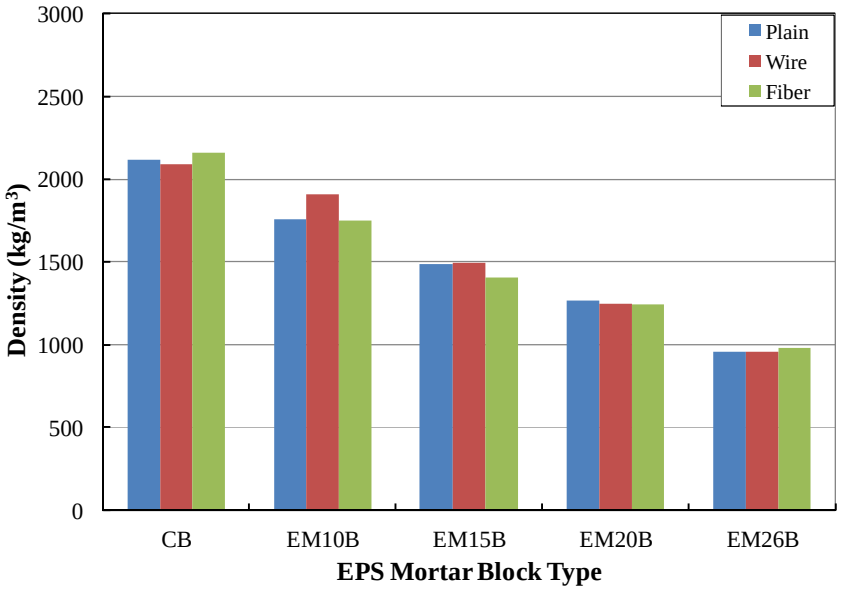

Figure 4.12: The density of the control and different batches of EPS mortar hollow block units

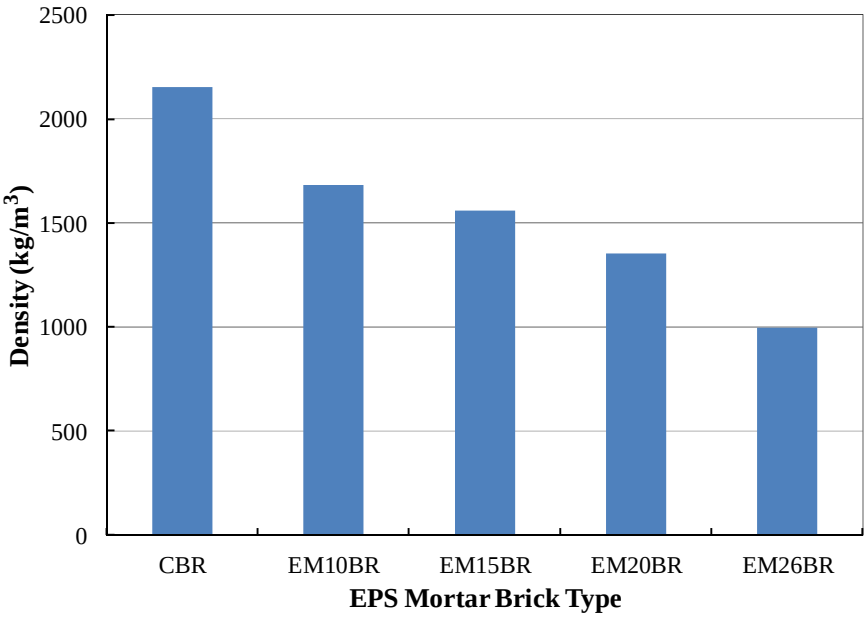

Figure 4.13: The density of the control and different batches of EPS mortar solid bricks

4.3.3 Effect of EPS Content on Compressive Strength

The compressive strength of the EPS mortar hollow blocks and solid bricks was adversely affected with the increase of EPS particles content as illustrated in Figures 4.14 and 4.15. Hollow blocks made from batches EM10, EM15, EM20, and EM26 showed 28, 50, 54 and 74% less compressive strength when compared to that made from the control mix. On the other hand, the solid bricks made from batches EM10, EM15, EM20, and EM26 had 31, 49, 59 and 74% less compressive strength when compared to that made from the control mix.

The strength reduction exhibited by EPS hollow and solid masonry units with the EPS content is almost similar. Nonetheless, when the compressive strength of the hollow blocks and solid bricks is compared as a percentage to that of the cubes and cylinders, the strength difference diminishes. For example, the compressive strength of the control and EPS mortar hollow blocks as a percentage of that of the cubes for the control, EM10, EM15, EM20, and EM26 mixes was 28%, 47%, 63%, 79% and 68% respectively. In addition, the compressive strength of the control and EPS mortar solid bricks as a percentage of that of the cubes for the control, EM10, EM15, EM20, and EM26 mixes was 26%, 42%, 59%, 65% and 63% respectively. This observation could be explained by the shape effect elaborated in the next section.

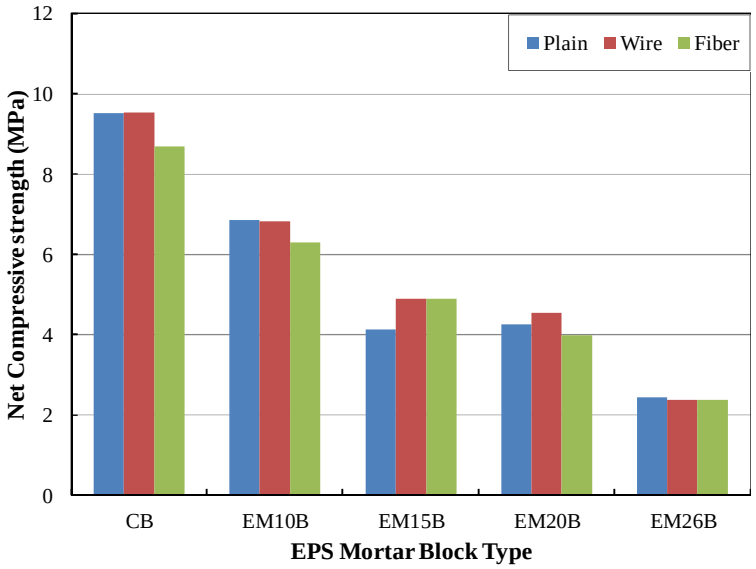

Figure 4.14: The net compressive strength of the control and different EPS hollow block units

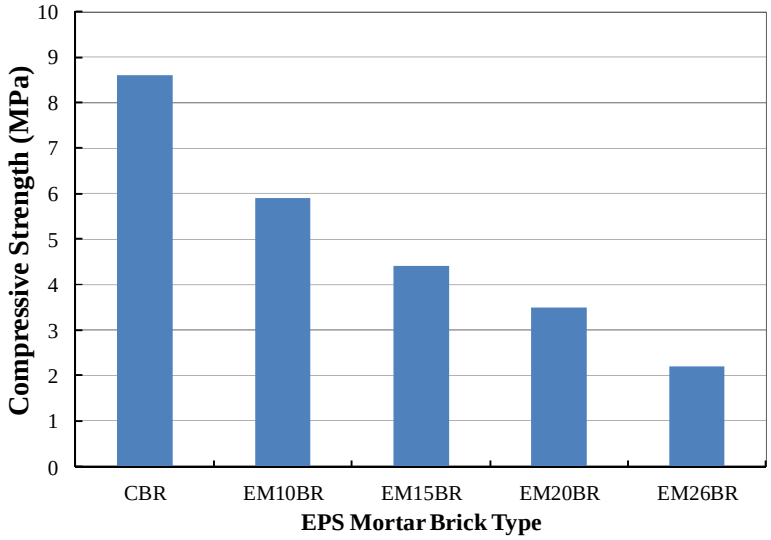

Figure 4.15: The compressive strength of the control and different EPS solid bricks

4.3.4 Shape effect on Compressive Strength

Specimens of different shape and surface finish were tested for compressive strength. This section aims at depicting the variation of compressive strength of the control and EPS mortars with the shape of specimens, surface finish and boundary conditions. It is important to relate the compressive strength of the cubes to the hollow blocks and bricks because the compressive strength of cubes is generally used as a representation of the strength of a given structure. Figure 4.16 shows the compressive strength of cylinders, cubes, hollow blocks and bricks of the control and EPS mortar mixes, Ferrocement Blocks and Fibrocement Blocks are respective acronyms for steel mesh reinforced and GFRP reinforced blocks. The figure demonstrates that the control specimens have the following strength vs. shape characteristics: 1) the cubes gave higher compressive strength than the cylinders, 2) the compressive strength obtained by cylinders and cubes was significantly higher than those obtained by the hollow blocks and the bricks, 3) hollow blocks had slightly higher compressive strength to that of the bricks. However, as the EPS content increased, the shape effect of the specimens was downscaled. This is better illustrated in Figure 4.17 that shows the compressive strength of the control and EPS hollow blocks as a percentage of that of the cubes and cylinders of respective batches. Similar relation for the solid bricks is presented in Figure 4.18. The relative percentage of the compressive strength of the control hollow blocks was the lowest.

The introduction of the first EPS dosage increased the relative percentage and reached the highest value for hollow blocks made from the EM20 mix. For example, from Figure 4.17, the compressive strength of the control plain hollow blocks is 29% and 36% of the compressive strength of the control cubes and control cylinders respectively.

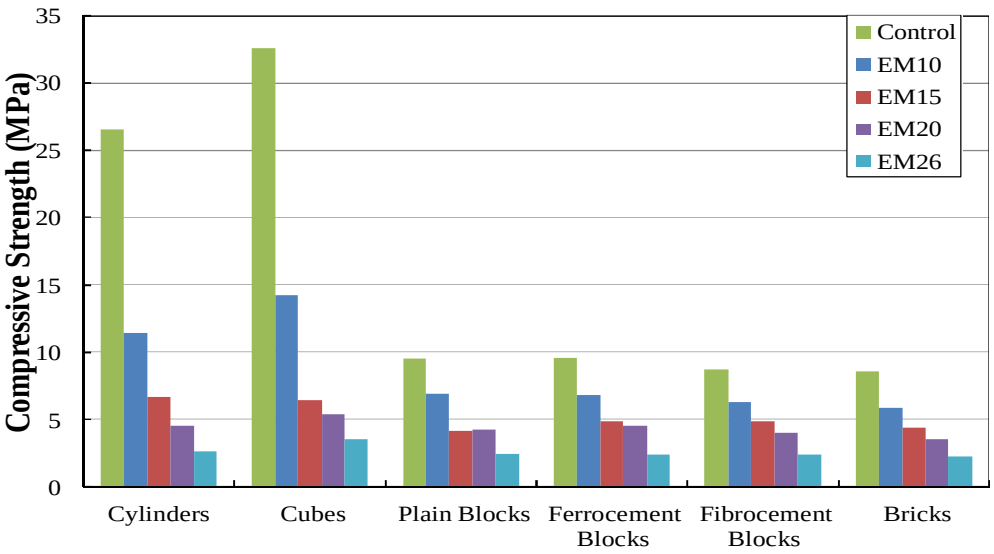

Figure 4.16 Effect of Specimen type and shape on the compressive strength of different specimens

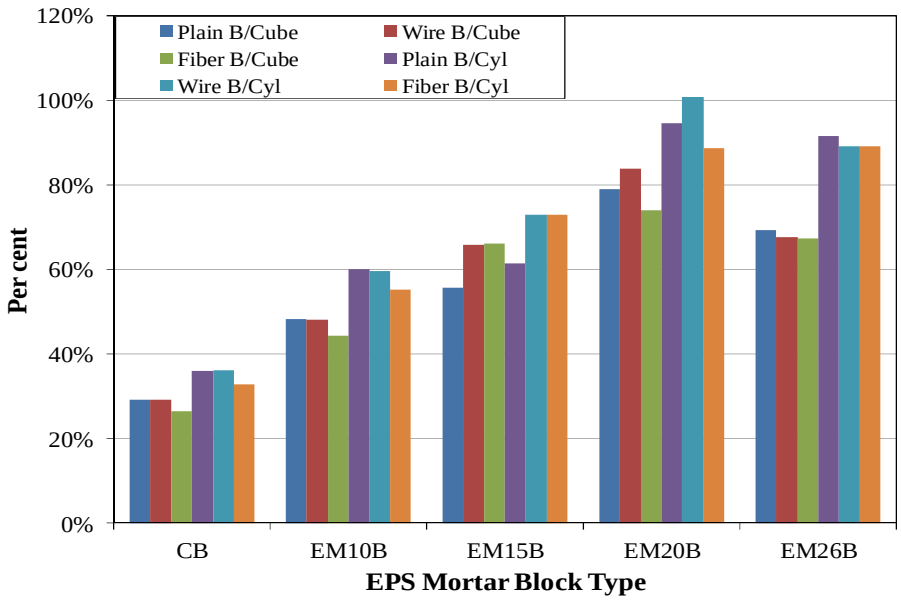

Figure 4.17: Percentage hollow block strength of the cube and cylinder strength

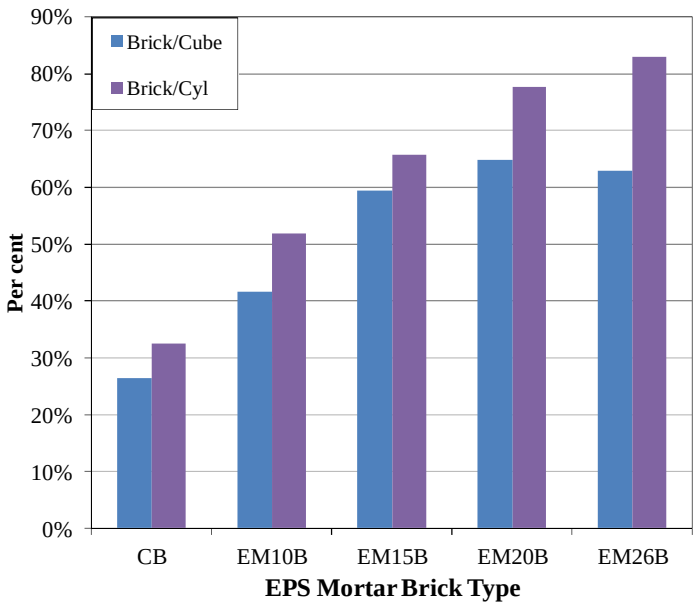

4.18: Percentage solid brick strength of the cube and cylinder strength

Similar trend was found for the solid bricks with the exception that the percentage of the strength relative to that of cylinders kept increasing up to the solid bricks made of EM26. Furthermore, the graph shows that the strength of the hollow blocks and bricks as a percentage of the compressive strength of cubes is lower by about 10 to 20% when compared to the compressive strength as a percentage of that of cylinders because cubes yield higher compressive strength than cylinders.

In the summary, the effect of shape variation on the compressive strength was more pronounced in the case of control specimens. The shape effect rises from the development of frictional—shear forces—between the loading platen and specimen that exerts confining pressure on specimens and counteracts its lateral deformation while loading. The platen confining effect and hence the shape effect is reduced by using frictionless platen such as rubber pad between the loading platen and the specimen, which was the procedure for all hollow blocks, solid bricks and cylindrical specimens. The cubes had friction boundary conditions. Although frictionless boundary conditions were applied, for almost all the specimens, the shape effect predominated the results of the compressive strength obtained by the control mix and diminished in all the EPS mortar specimens. Constant boundary conditions maintained for all the tested specimens assumes that the shape effect diminishing

influence on the compressive strength of EPS mortar specimens is intrinsic to the EPS aggregates effect. Moreover, the shape effect influenced the compressive strength of the control and EPS mortar cubes and cylinders. As a result, the *apparent* diminish of the shape effect could be explained by 1- the geometry of the presence of holes in the hollow blocks, 2- the very low slenderness ratio of the solid bricks and 3- the ability of EPS mortars to deform and redistribute stresses after crack initiation. The frictionless boundary conditions and the small thickness of the hollow block faces allowed the masonry units to deform in a barreling shape under compressive loading, which might have induced tensile stresses. The plain mortar of the control hollow blocks had limited straining characteristics and splitting cracks occurred which undermined the section to carry further load and failure occurred. Therefore, the presence of holes in the control hollow blocks undermined load carrying capacity and mortar efficiency. On the other hand, EPS mortars showed that they have higher straining ability, higher tensile toughness and sustained load long after crack initiation. As a result, the EPS mortar hollow blocks increased the mortar efficiency in load carrying despite the presence of the holes. Nonetheless, the capping of EPS mortar hollow block specimens might have exerted some restraining effects on lateral expansion because uncapped specimens exhibited more spalls upon failure, however, yielded more or less similar compressive strength.

This is similar to the case of the control solid bricks, where the very low slenderness ratio (almost 0.25) amplified the differential effect between its frictionless top that was free to deform and its friction bottom—the platen where the specimen rested— which resulted in splitting tensile cracks extending from top to bottom. However, the more straining characteristics of the EPS mortars allowed the specimen to sustain the differential deformation and withstand loading post the initiation of cracks.

The influence of EPS on the failure behavior of mortar is explained better in section 4.3.6 which discusses the failure pattern of different blocks. This is because explaining the geometry effect is inseparable from the pre-peak and post-peak specimen reaction to loading through the quantity and quality of cracks.

4.3.5 Reinforcement effect

The compressive strength of the reinforced blocks, in general, was expected to yield higher compressive strength than the plain ones. The expected higher compressive strength is attributed to the contribution of the vertical strands of the wire mesh in carrying some of the compressive strength load in addition to the confinement effect the horizontal stands of the wire and GFRP meshes would exert on the blocks. However, the ferrocement and plain hollow blocks of the EM10 mix had almost equivalent compressive strength, which was higher than that of the GFRP reinforced ones. The lower compressive strength obtained by the latter could be attributed to weak fiber strands in the direction of compression which would have lessened their confinement effect. This is also related to the difficulty in casting the GFRP reinforced specimen that resulted in some deformations, folds and tilts in the mesh wrap that underestimated its confinement effect.

The control ferrocement hollow blocks carry equivalent compressive strength as that of the plain ones. The presence of the wire mesh caused the mortar face to crack near the ultimate load due to the differential modulus of elasticity—straining capacity—between the mortar matrix and the reinforcement which reduced mortar's effective area in resisting the compressive strength. This resulted in a lower compressive strength of the control ferrocement hollow blocks than expected. A similar mortar cracking phenomenon occurred to GFRP reinforced hollow blocks, in addition to the ripping of parts of the fiber mesh itself which reduced its integrity and ability to confine the mortar. As a result GFRP reinforced hollow blocks exhibited the lowest compressive strength in its group.

The EPS mortar had a combination of factors that might have affected its compressive strength as plain and reinforced composite. The first effect is the variation of density mentioned at the beginning of this chapter. It was reported that the minor variation in density would result in a pronounced increase in the compressive strength of EPS mortars. The adverse effect of density variation is noticed in the compressive strength of the plain and reinforced batch of the hollow block of mix EM10. The ferrocement reinforced hollow block belonging to this batch yielded a compressive strength and density of 6.8 MPa and 1910 kg/m^3 respectively. Its plain counterpart yielded a 6.9 MPa compressive strength and had a density of 1758 kg/m^3. The effect of density is obvious because, following the pattern of the control blocks, cracking of the mortar reduced its ability to carry compressive load, however,

because the density of the ferrocement blocks was higher than that of the plain ones, their compressive strength was also higher. The density effect was offset with the GFRP reinforced hollow blocks belonging to the same batch, which had close density to that of the control ones and exhibited lower compressive strength as expected.

On the other hand, lighter reinforced EPS hollow blocks, namely, EM15 and EM20 mixes, exhibited a different behavior. These different blocks in these batches had almost similar densities and exhibited mortar matrix shear cracks and spalls with the increase in the compressive load. However, the ferrocement hollow blocks had higher compressive strength than that of the plain and fiber ones in consequence to a better utilization of the tri-axial confinement exerted by the wire mesh. Moreover, the vertical and horizontal strands of the wire mesh might have resisted some of the compressive load (Johnston and Mattar, 1976) in addition to the crack bridging effect of the reinforcement that might have prolonged the load-carrying capacity of light EPS mortar hollow blocks long after cracking. This trend was also noticed on GFRP reinforced EPS blocks made with mix EM15. Nonetheless, GFRP reinforced EPS hollow blocks belonging to batch EM20 exhibited lower compressive strength than that of the plain and ferrocement although they had similar density and similar matrix modulus of elasticity. As a result, the confinement effect of GFRP mesh and its contribution to the increase in the compressive strength cannot be confirmed for the GFRP EPS mortar hollow blocks.

The lightest EPS mix exhibited almost equivalent compressive strength for its three types plain, ferrocement and fibro-cement which indicate that reinforcement was ineffective in this batch.

Evidently, the inclusion of reinforcement did not shift any of the hollow blocks from non-load bearing category to load-bearing category. Nonetheless, improvement of failure pattern was observed on all reinforced hollow blocks. Henceforth, the wire mesh and fiber mesh confinement might have an effect on the pre-peak behavior of the specimens; however, its effect on the post-peak behavior of EPS mortar hollow blocks was pronounced and will be further discussed in the following section.

4.3.6 Failure Pattern of the Hollow Block Specimens

Figure 4.19 (a) exhibits the failure pattern of the control plain hollow blocks. The extension of the vertical cracks from the upper bound to the lower bound of the specimen indicated sudden and brittle failure. The crushing of the specimen was expected because of its low-slenderness and prismatic shape (Carpinteri et al. 2001). On the other hand, the failure of the ferrocement control hollow blocks was completely different. The initiation of the first crack occurred before reaching the ultimate stress which is a sign of gradual failure. Figure 4.19 (b) shows that the control ferrocement hollow blocks were intact and minimum debris was noticed. Vertical cracks were inclined in the form of localized shear cracks that took the shape of a wedge. Also, the extent of the vertical cracks from the top of the specimen to the depth of the formed wedge told the degree of specimen confinement and boundary conditions. Furthermore, horizontal splitting tensile cracks seem to bridge between the inclined shear cracks indicating that the wire mesh strands bridged the vertical cracks. Similar behavior was also noticed on the failure pattern of the control GFRP reinforced hollow blocks as shown in Figure 4.19 (c). However, some of the blocks split into two halves from the corner as the fiber wrap strands were torn upon failure. In summary, the presence of the wire mesh enhanced the ductility of the failure of the control hollow blocks. It must be noted that slippage of the wire and fiber wrap occurred as the loading machine initiated loading.

a) Plain Hollow Block

b) Wire mesh reinforced hollow block

c) Fiber glass reinforced hollow block

Figure 4.19: Failure pattern of the plain, wire mesh reinforced, and glass fiber reinforced control hollow blocks

On the other hand, the first inclusion of EPS dosage (EM10) enhanced the failure pattern of the plain hollow blocks significantly. EPS mortar hollow blocks exhibited first crack at strengths much lower than the ultimate strength which is a sign of prolonged failure and toughness. Figure 4.20 shows the failure pattern of plain EM10 hollow blocks. All the compressive cracks were inclined shear cracks and sliding wedges which indicated high

toughness and ductility (Vonk 1993). The shape and depth of the wedge indicated frictionless boundary conditions. The EMBP10 specimens were highly intact after failure. The failure of the EMBP10 specimens was affected by the EPS inclusion more than the shape of the specimen. Prisms of low slenderness are characterized by dispersed vertical splitting cracks that cover the entire volume of the specimen (Vonk 1993). But with the inclusion of the EPS particles, the cracks became finer and concentrated in a wedge pattern that followed the confinement conditions of the specimen. An interesting observation occurred in the depth of cracks, most of the cracks were surface ones and the EPS blocks were intact at failure.

a) Plain EM10 hollow block

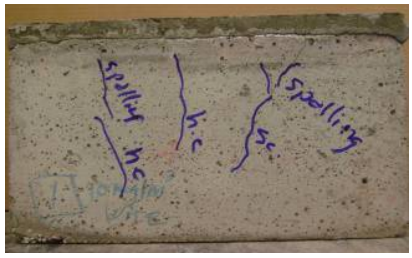

b) Wire mesh reinforced EM10 hollow block

Figure 4.20: Failure pattern of the plain, wire mesh reinforced EM10 hollow blocks

The increase in the EPS dosage increases more the ductility and toughness of the EPS mortar hollow blocks as shown in Figure 4.21 and 4.22. Lighter plain EPS mortar hollow blocks would have more dispersed spalls and sliding triangular cracks rather than defined cracks.

a) Plain EM15 hollow block

b) Wire mesh reinforced EM15 hollow block

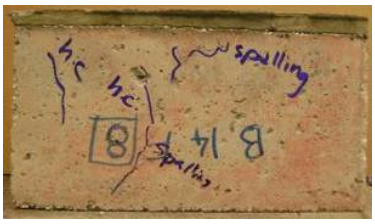

c) Glass Fiber reinforced EM15 hollow block

Figure 4.21: Failure pattern of the plain, wire mesh reinforced, and glass fiber reinforced EM15 hollow blocks

a) Plain EM20 hollow block

b) Wire mesh reinforced EM20 hollow block

Figure 4.22: Failure pattern of the plain, wire mesh reinforced EM20 hollow blocks

The failure enhancement with the first dosage of EPS was further refined with reinforcement. Although the presence of spalls and sliding cracks is indicative of higher toughness, the absence of cracks is a proof of ductility. It seems like the combination of EPS and reinforcement mesh produced refined and more inclined shear cracks that were barely visible. Steel and fiber wires acted at the initiation of the formation of tensile cracks by bridging them to produce a finer shear lines. The inclined shear cracks were almost 45 degrees in an indication of a more ductile failure (Vonk 1993). The inclined cracks also indicated that the direction of the maximum stresses changed from the vertical direction due to the presence of reinforcement.

The shape of the cracks resembled the shape of confined stresses that were provided by the frictionless boundary conditions. The less cracked block maintained close compressive strength as that of the plain blocks. Also, the presence of reinforcement resulted in a more prolonged and gradual failure. On the other hand, lighter reinforced EPS mortar hollow blocks exhibit inclined hair cracks that are localized in the direction of the composite action between the reinforcement and the EPS mortar. Hollow blocks made of EM26 mix showed failure by compressibility and cracks in plain and reinforced specimens were invisible. And, the sliding cracks in the form of spalls appeared shyly.

4.3.7 Failure Pattern of the Solid Brick Specimens

Unlike the hollow block specimens, the failure pattern of the brick specimens was governed and influenced mainly by their low slenderness ratio (Carpinteri et al. 2001 and Vonk 1993). The height to width (slenderness) ratio was very low that the crack pattern was highly distributed across the length and width of the specimen. The noticed effect of EPS on the failure pattern was that higher EPS content resulted in more ductile and tougher failure.

Although the increase in EPS content produced finer shear cracks and sliding spalls, it also produced higher volume of cracks that were dispersed over the whole volume of the brick as an indication of the ductility and energy release during failure. Figure 4.23 displays the transition of ductile failure from localized vertical cracks for EPS bricks belonging to mix EM10 to the more diffused sliding cracks exhibited by bricks belonging to mix EM20. It is observed that cracks extended from the frictionless conditions towards the direction of friction conditions—from top to the bottom.

a) EMBR10 b) EMBR15 c) EMBR20

Figure 4.23: Failure pattern of the solid EPS bricks

The above discussion of crack description and failure will help shed the light on the geometry effect observed on the control and EPS mortar specimens. Mortar is a quasi-brittle material whose strength characteristics were until the mid 1980s related to the size of specimen in a statistical relation. Weibull theory depicted that failure occurred in specimens of large volume at lower strengths because they were more probable to encounter a critical zone of weak strength that would foster the progressive growth of micro-cracks that lead to a propagating failure. However, this theory is rebutted when a macro crack develops and is sustained in the specimen before reaching the peak load, which is the case in all EPS mortar specimens. The existence of a sustained non-propagating crack and the dispersion of cracks result from the interaction between the stress redistribution at maximum load and energy release of load through dispersed cracking in the fracture process zone (area in front of the fracture tip). The localization of damage in definite bands—brittle deep cracks—in the control specimens is a deterministic size and shape effects symptom. However, the diminishing of localized cracks in EPS mortar specimens indicate a shift in ductility and increase in toughness where, a large fracture process zone exists, energy is released through non-propagating cracks and load redistribution counteracts crack propagation.

4.4 Durability Test Results

This section presents the experimental results obtained from the durability tests. The durability performance of control specimens and plain, glass fibre mesh reinforced and wire

mesh reinforced EPS mortar hollow blocks when subjected to aggressive environments as explained in Chapter 3.

4.4.1 Absorption test results and discussion

The hydrated paste in concretes and mortars is considered as porous materials. Absorption is an indirect measurement of concrete and mortar durability. The vulnerability of concrete and mortar to absorb water increases the chance of penetration of deleterious solutions and chemicals.

The average absorption percent of EPS mortar hollow blocks is presented in Table 4.7. The maximum limits of water absorption of concrete hollow blocks as stated in ASTM C90 are also presented in Table 4.7. The values obtained from the control hollow blocks indicate the excellent quality of the mortar matrix. The table shows that the mean value of water absorption for all test specimens, regardless of the EPS content, is well below the maximum allowable limits as specified by ASTM C90.

Table 4.7: Absorption percent of the different types and densities of EPS hollow blocks

Batch	Average Density Kg/m^3	Average Absorption % Sorted by Reinforcement Type						ASTM C 90 Maximum Water Absorption
		Plain		Wire Mesh		Fibre Mesh		
		kg/m^3	%	kg/m^3	%	kg/m^3	%	kg/m^3
C	2135	10.03	0.47	16.44	0.77	19.86	0.93	208
EM10	1686	51.1	3.03	56.83	3.37	57.50	3.41	240
EM15	1441	53.74	3.73	56.77	3.94	63.54	4.14	288
EM20	1214	55.95	4.61	52.91	4.36	44.17	3.64	288
EM26	959	31.84	3.32	33.28	3.47	26.47	2.76	288

The good quality of the pore structure of the control hollow blocks, as depicted by the very low percentage of absorption, could be mainly attributed to the silica fume that enhanced the

pore structure of the blocks. Silica fume densifies the cement matrix and produces finer and disconnected pore system (Song et al, 2010). The average absorption values increased sharply by replacing part of the fine aggregate volume by 10 kg/m^3 of EPS (the lowest dosage of EPS in the current study) regardless of the type of mesh reinforcement. The absorption ratio increased from 0.47 % for the plain control specimen to 3.03% for the case of plain hollow blocks, from 0.77% to 3.37% for wire mesh reinforced hollow block, and from 0.93% to 3.41% for the case of glass fiber mesh reinforced hollow block. This abrupt behavior indicates that the quality of the mortar matrix, as manifested in absorption values, was affected by the inclusion of EPS. The table also shows that the average water absorption values of EPS hollow blocks do not seem to vary significantly with the increase of EPS dosage beyond the lowest dosage of 10kg/m^3. The observed absorption percentage for all types of hollow blocks is also illustrated in Figure 4.24.

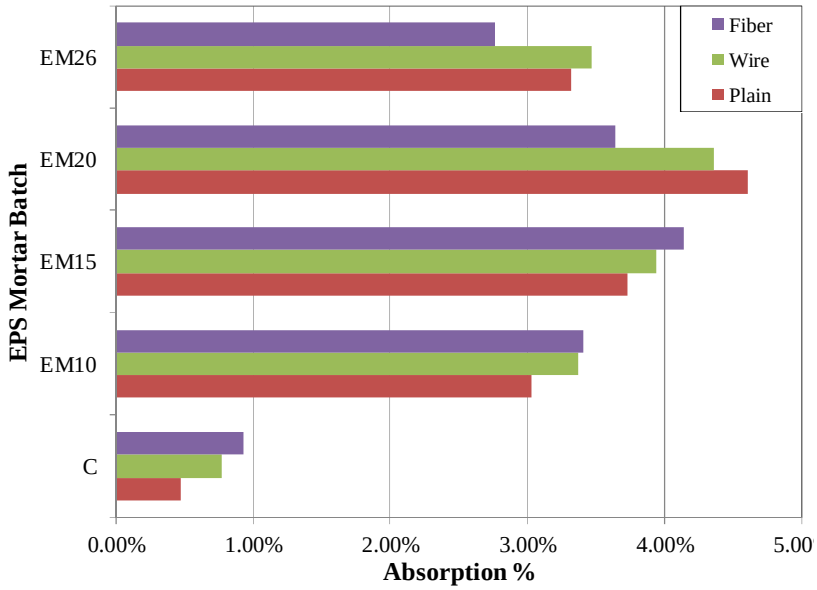

Figure 4.24: Average water absorption for the different types of EM hollow blocks

Despite of this increase, the absorption limits recorded by EPS hollow blocks were still well below the ASTMC 90 maximum absorption limits. Similar absorption range was reported by Babu and Babu, 2003 and was identified in this literature article as good quality mortar mix.

The lowest average water absorption was recorded for the hollow blocks made with mix EM26 and the highest average water absorption was recorded for the ones made with mix EM20. The change of the percentage of water absorption with the change in EPS contents

and the type of mesh reinforcement did not show a definite pattern. The figure shows a relatively slow rate of increase of water absorption that starts with blocks made from mixes EM10 and ends with blocks made from mix EM20. This increasing trend is reversed to a decreasing pattern for hollow blocks made with mix EM26.

EPS wastes are hydrophobic lightweight aggregates. Therefore, the drastic change in the absorption values comes from the effect EPS wastes on the matrix rather than the porous structure of the EPS aggregates as in case of processed porous lightweight aggregates such as LECA. Shrinkage is one of the factors that induce the formation of micro cracks in the cement paste matrix. Generally there are two types of restraining actions that result in shrinkage micro-cracks: 1-self restraint which occurs upon mortar drying due to the steep moisture gradient and shrinkage gradient between the mortar and the drying surface that constraints its shrinkage, 2-aggregate restraint of the cement paste from shrinking which is highly dependent on the size and concentration of aggregates (Bischoff and G.M. van Mier, 2008).

Shrinkage micro-cracks occur primarily in EPS mortars due to the restraining effect of the moulds. Micro-cracks due to this type of shrinkage restraint occur in perpendicular sense to the direction of the restraining face. The thin layer of EPS mortar that exists on the outer surface of the blocks is the one responsible for the permeability of the EM blocks and is subjected to three devastating effects: 1- the higher rate of drying of EPS mortar (Bischoff and G.M. van Mier, 2008), 2-the welcoming effect of EPS particle to cement paste shrinkage away from the moulds walls and 3-the tensile stresses developed in it due to the restraining action of the walls of the mould. In line with Bischoff and G.M. van Mier (2008) statement that cracks develop due to shrinkage in surface retrained concrete are assumed as macro-cracks which increase the permeability problem, shrinkage macro-cracks would exist on the outer surface of the EPS hollow blocks. As the EPS dosage increases, the thickness of the mortar's interface with the moulds surface becomes thinner and more perforated with more EPS particles which increases the tendency of cement paste to shrink and increases the micro-cracks due to surface restraints. This is why most of the EPS hollow blocks had higher values of absorption at a rate that was relatively indifferent to the content of EPS in the mix. As illustrated in Figure 4.24, the average absorption of EPS hollow blocks increases marginally from the EM10 hollow block and maximum values are reached by the EM20 blocks.

On the other hand, the lower average absorption values exhibited by the EM26 hollow blocks present a challenge in its interpretation. This phenomenon might be attributed to the assumption that the outer surface layer of the EM26 hollow blocks is formed of a thin film of cement paste of very low values of restraining sand aggregates. This film is connected to the rest of the block by a highly perforated cement matrix of hydrophobic EPS particles that form a sluggish path between the cracked surface mortar and the inner films of the mortar. This sluggish path as well as the hydrophobic effect of EPS particles might repel water.

The reinforcing mesh in the skin of the hollow blocks has several effects which influence the absorption of the blocks. On one hand the reinforcement mesh helps in resisting the shrinkage cracks. On the other hand, the space between the reinforcement mesh and the mould's walls was very tight despite the use of super plasticizer and vibration adoption. In addition, reinforced hollow blocks might have less compaction than the plain ones during casting to ensure that the reinforcement cage will not sway off its position which might have caused the formation of more surface pores or air pockets that allowed for the ingress of water. The obvious trend is the negative effect of wire and GFRP mesh reinforcement on the absorption of the control and EPS hollow blocks. However, the absorption of plain hollow blocks made of EP20 mortar was higher than that of reinforced blocks. The may be explained by the fact that the effect of shrinkage cracks may have suppressed the other effects for this mix.

Another factor that might require further research is the absorption behavior of the EPS aggregates. As previously stated in Chapter 3, EPS aggregates have 2.7% water absorption, which is nearly equal to the difference between the control and EPS hollow blocks absorption values. Although the absorption capacity of EPS aggregates were nearly impossible to gauge by soaking the aggregates in water--as they float, may be the pressure of the water ingress between the matrix interface with the EPS aggregates allowed the latter to host water inside its pores. Since both arguments have not been verifies by laboratory measurements, it is fair to consider that the higher absorption rate of EPS mortar hollow blocks is a compound behavior due to shrinkage and EPS aggregate high water absorption.

4.4.2 Acid/Sulphate test results and discussion

This section illustrates the deterioration characteristic of the hollow block batches and the effect of weight loss on the compressive strength. The effect of the EPS dosage and reinforcement inclusion will also be discussed.

4.4.2.1 Visual Observation

When the control hollow blocks were immersed in the acidic solution, leaching occurred at near constant amount throughout the four cycles. By the second wetting cycle, the thickness of the face shell of the blocks was notably reduced and parts of the wire mesh were exposed in case of wire reinforced control blocks. The fiber reinforced blocks exhibited same deterioration where the fiber mesh wrapping one of the faces was completely exposed. The third wetting cycle exposed more of the wire and fiber reinforcement areas and weathered the exposed reinforcement wire mesh into air and the exposed fiber mesh into debris. The fourth wetting cycle exhibited more leaching and weathering.

Visually, the first drying cycle was characterized by the formation of large dense whitish spots that protruded on the face shell of the blocks. The white expanded spots could be gypsum as reported in literature. The second drying cycle was characterized by the formation of a thin film of whitish yellowish layer that fell off with friction and the oxidation of the exposed part of the wire mesh. The gypsum layer exposed sand aggregates in a typical erosion deterioration. The thickness of the whitish layer continued to increase and the exposed wire and fiber continued to oxidize during the last two drying cycles. Similar deterioration was reported by Fattuhi and Hughes (1988). The deterioration of control blocks was characterized by the maximum leached contaminants of all the block specimens.

The deterioration of EPS hollow blocks was significantly different. A general observation was that the amount of contaminants leached decreased with the increase of the content of EPS particles in blocks (decrease in density). Also, the leached material would flow out carrying surface EPS particles during the process. The first wetting cycle was characterized by maximum leaching of hydration products of all the four cycles. By the second wetting cycle, EPS blocks of higher densities revealed a reduction in the thickness of the face shell while EPS blocks of lower densities exhibited expansion in volume. Denser EPS blocks exposed some of the wire and fiber reinforcement, just a strand of wire or two. By the fourth

wetting cycle all EPS blocks exhibited some sort of expansion in the face shell. On the other hand, the first drying cycle revealed the eroded EPS particles and the surface shell had a thick gypsum layer formed. The rest of the cycles were characterized by the expansion of the eroded beads in a pop-corn like shape and the expansion of the gypsum layer. The eroded EPS particles and gypsum layer would fall off with friction. The revealed wire mesh was oxidized by the third drying cycle. All EM blocks displayed sponge like shape and texture at the end of the fourth drying cycle.

4.4.2.2 Weight Loss and Decrease in Compressive Strength

The percentage weight loss was monitored and reported at the completion of each cycle. Table 4.8 shows the cumulative percentage weight loss as well as the loss in compressive strength when the blocks were tested at the completion of the 4 cycles. The results are also plotted in Figures 4.25 and 4.27.

Because of the constant binder content and w-cm ratio used in all the control and EPS hollow blocks and the same testing conditions, one may expect that the leaching reaction and products should be similar. Also because leaching depends on the porosity, and based on the results obtained from the absorption test, one may expect that the control blocks should have the least leaching and weight loss. However, Table 4.8 and Figure 4.25 show the contrary to this logic as the weight loss decreases with the increase of EPS content. This phenomenon can be explained based solely on the effect of EPS on cement paste.

In addition to the effect of EPS particles as explained under the absorption section, the hydrophobic EPS particles act also as separate buffer zones that causes sluggish path of contaminants in the mortar. The more the content of the particles the more it is difficult for the leaching process to occur. Figure 4.25 illustrates the cumulative weight loss for all the hollow block batches over the 4 cycles. The observations drawn from this figure are:1-the weight loss, which is a function in the leached content, decreases with the increase of EPS content in blocks, 2- the rate of weight loss with the progression of cycles decreases to a constant trend with the increase of the EPS content, 3-most of the weight loss in EM blocks occurs in the first and second cycles.

Table 4.8: Test results of cyclic ponding of test specimens in 5% sulphuric acid solution

Batch	Average Density (kg/m^3)	Cumulative Weight Loss (%)				Loss in Compressive Strength (%)
		Cycle 1	Cycle 2	Cycle 3	Cycle 4	
CBP	2095.79	6.49	15.11	20.11	23.25	25.78
CBW	2086.33	3.80	6.57	8.90	12.27	19.06
CBF	2156.2	6.50	12.24	17.43	21.40	22.89
EMBP10	1703.59	3.28	9.37	13.43	15.97	47.43
EMBW10	1828.92	2.72	7.96	11.85	14.94	40.09
EMBF10	1609.38	4.20	9.92	12.49	14.01	22.69
EMBP15	1412.82	2.39	6.35	7.88	9.22	14.73
EMBW15	1431.76	2.33	5.35	6.36	7.05	14.63
EMBF15	1346.56	3.88	6.63	7.66	8.84	14.88
EMBP20	1198.24	2.30	3.17	3.17	3.17	27.22
EMBW20	1248.28	5.16	6.06	6.06	6.21	29.28
EMBF20	1210.86	2.91	4.17	4.17	4.17	25.20
EMBP26	956.61	0.28	0.28	0.28	0.28	17.56
EMBW26	949.4	0.79	1.50	1.50	1.50	18.36
EMBF26	957.51	2.73%	3.11%	3.11%	3.11%	15.42%

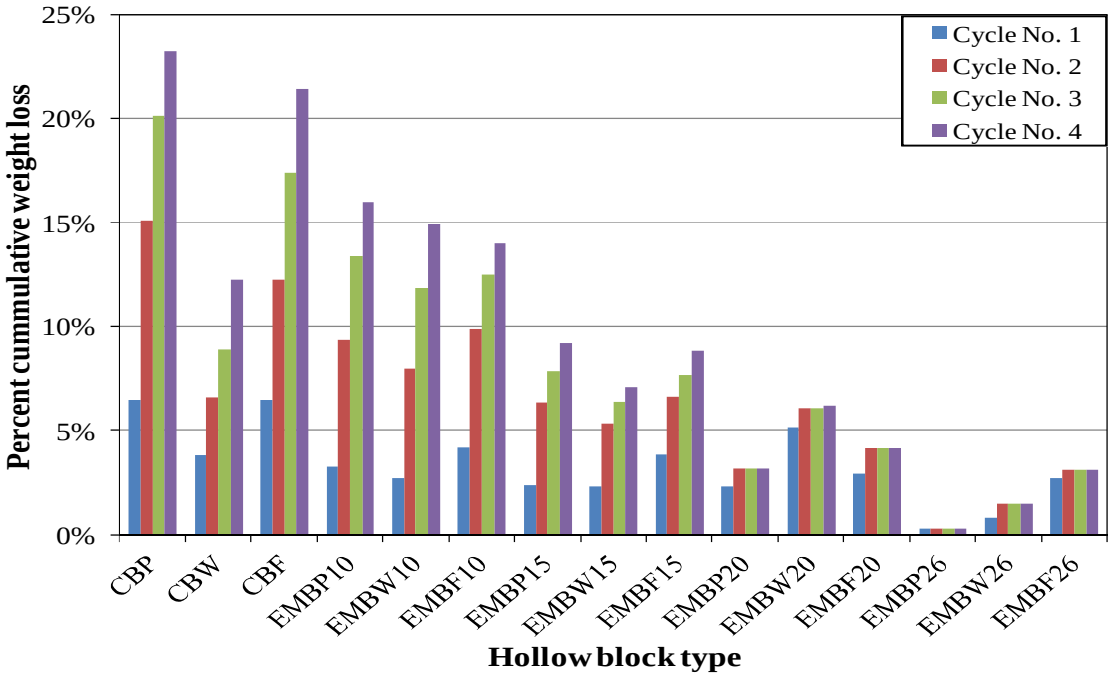

Figure 4.25: Average cumulative weight loss for the different types of EM hollow blocks

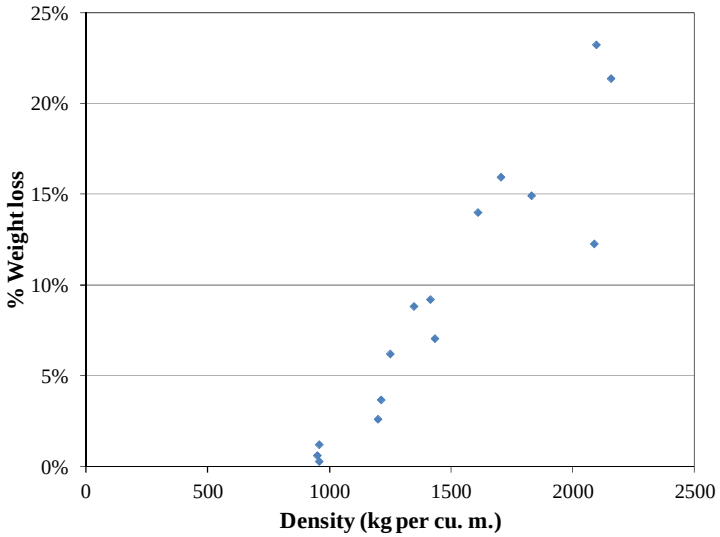

Figure 4.26: Average cumulative weight loss vs. density of EPS hollow blocks

Figure 4.25 shows that the rate of weight loss in the control blocks only decreases slightly over the four cycles. This suggests that the shrinking core and the moving leaching shell deterioration pattern continue even after four cycles. A direct effect is that the porosity of the control blocks increases and the size of the block decreases. The control blocks had the

thinnest face shell of all the tested batches after four cycles. On the other hand, the rate of weight loss over the four cycles of EPS hollow blocks decreases with the increase of the EPS content (decrease in density). EPS hollow blocks that belonged to batches EM20 and EM26 ceased losing weight after the second and first cycles respectively. This means that the shrinking core and the moving leaching shell phenomenon cease to exist in EPS mortar blocks of lower densities. As a result, the porosity of the face shell would not be compromised with more acid leaching. Also, the declining rate and cessation of weight loss are indicative that EPS hollow blocks are more affected by sulphate salt attack more than sulphate acid attack. Sulphate salt attack would form a thick whitish-yellowish gypsum layer that formed armor to the abrasive solution. It was also noticed that after the ponding cycles the EPS particles would be exposed and appear on the blocks' surface due to leaching. During the drying cycles the EPS particles on the face shell of the blocks would expand in a pop corn manner. The EPS hollow blocks would appear fluffier due to the expansion of the layer surrounding EPS particles over the surface shell. The amplified expansion of the deteriorated surface shell could be attributed to the lack of restraining action of the EPS particles to the expansion of the mortar. Slight friction would release some of the expanded powder taking off some EPS particles with it. Figure 4.26 shows a decreasing linear trend of the cumulative weight loss with the decrease of density of the control and EPS hollow blocks.

Figure 4.27 does not show a specific relation between the final cumulative weight loss and compressive strength loss of the EM blocks. On the contrary, it shows a direct proportionality between the weight loss and the compressive strength loss of the control blocks. This could indicate that the weight loss due to leaching was the primary factor for compressive strength loss in the control blocks. However, comparing the strength loss and weight loss in the EM blocks would suggest that leaching was a secondary factor detrimental to strength. The primary aggression could be chemical reactions related to sulphate salt attack that caused loss in strength accompanied by shrinkage cracks and material expansion. This argument is supported by the declination and cessation of the rate of weight loss reported for EM blocks as well as expansive deterioration discussed earlier. The decrease in leaching might be due to the formation of the thick impervious gypsum layer that reduced the permeation of the acid water. Another deterioration mode indicative to sulphate salt attack was the presence of

surface shrinkage cracks over face shell of EM blocks. It was also noticed that most of the block specimens exhibited strength loss that ranged between 15 and 30%.

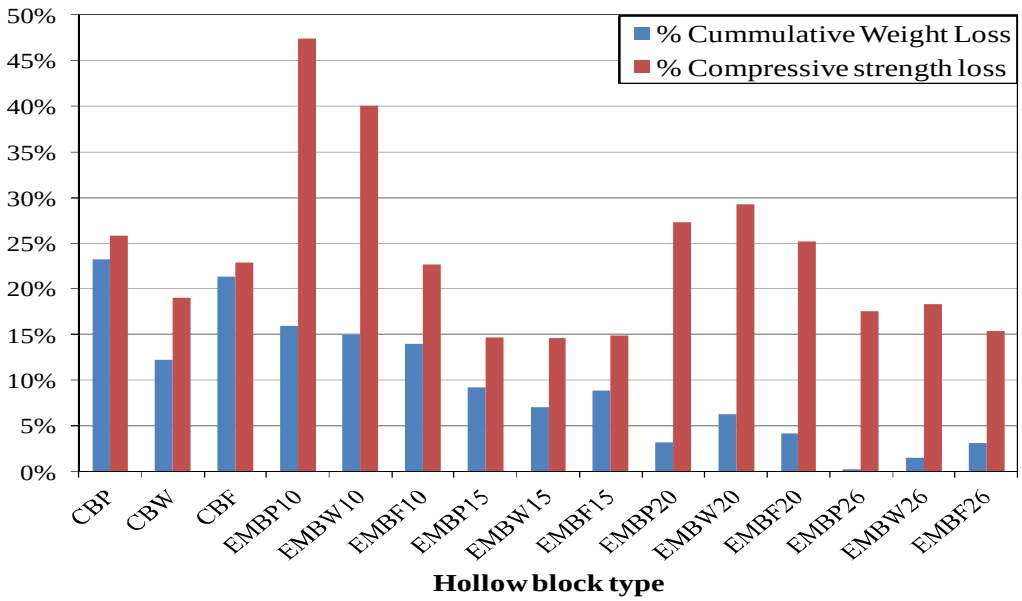

Figure 4.27: Average compressive strength loss for the different types of EPS hollow blocks

Figure 4.28 shows that the strength loss is not affected by either the density of the block or the EPS content, except for a few outliers. This could be explained by the fact that sulphate attack only targets the hydration products of the binder which is kept at a constant content of 500 kg/m^3. And, in mortars and EPS mortars, the compressive strength of the cement paste and its quality are the primary strength setters. Therefore, the deterioration faced by the control and different EM blocks may differ but the strength loss would be within a certain range that could be estimated through the chemistry of the sulphate reaction with the hydrated paste. Some specimens however would show higher strength loss such as specimens EMP10 and EMW10 which could be attributed to the higher surface porosity incurred during casting.

The role of reinforcement is more evident in the failure pattern which is discussed in the following section. The weight loss limits and the deterioration indicate that blocks made with EPS mortar of binder content 500 kg/m^3, silica fume replacement of 9.8% and w/cm ratio of 0.45 showed good resistant to strong acidic and sulphate environments. This was manifested in the volumetric intactness of the blocks, the preservation of almost 70 to 80% of the

compressive strength and the ductility of failure under compression. EM blocks exhibited similar durability to that of the control blocks but with less leaching.

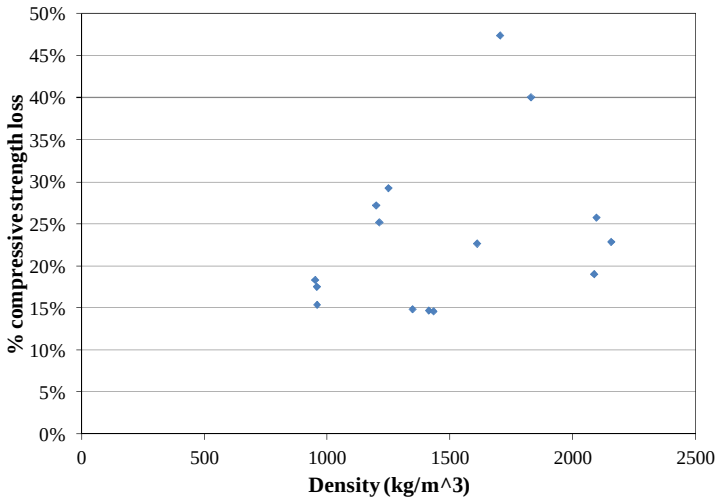

Figure 4.28: Percent compressive strength loss vs. density of different types of EM hollow blocks

4.4.2.3 Failure Pattern

The failure pattern will be better discussed by the effect of EPS content first then the effect of the reinforcement type on the failure patter of the hollow blocks. Figure 4.29 shows the effect of the EPS content over the failure pattern of plain EM hollow blocks. The surface deterioration of the hollow blocks is evident. The failure of the control plain hollow blocks was sudden and brittle in an explosive manner. With the increase of the EPS content to 10 and 15 kg/m^3 the failure transformed from brittle to a more gradual failure, yet, failure was in the form of disintegration. The failure was in the form of splitting longitudinal cracks the shuttered the blocks into pieces of separate columns. The increase of EPS content to 20 and 26 kg/m^3 produce a ductile failure that is characterized by the shearing of the loaded surface of the face shell.

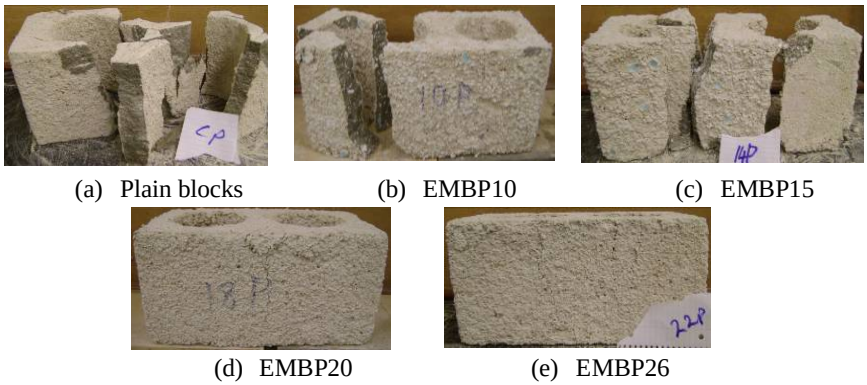

(a) Plain blocks (b) EMBP10 (c) EMBP15

(d) EMBP20 (e) EMBP26

Figure 4.29: Failure pattern of plain control and EPS mortar after wet-dry acid cycles

The effect of the wire mesh was evident over the failure pattern of the control block and all densities of the EM hollow blocks in Figure 4.30. The failure of the ferrocement control hollow blocks was gradual and in the form of longitudinal splitting brittle cracks. The split sections were kept intact by means of the wire cage and the block retained its volumetric shape. The first dosage of EPS tremendously improved the failure behavior of the ferrocement hollow blocks. Denser ferrocement EM hollow blocks, namely with EPS content to 10 and 15 kg/m^3, was characterized by a brittle longitudinal crack. The number of longitudinal cracks increased to two for EPS content of 15 kg/m^3 which is indicative to a more ductile failure. The longitudinal crack was surficial and the blocks retained their volumetric shape and no debris was noticed. The increase of the EPS dosage to 20 kg/m^3 produced ductile gradual failure that was characterized by an increase of the longitudinal cracks frequency. The loaded surface of the blocks also was characterized by the sliding of the surface into triangular chips. More ductile failure was revealed by the EMW26 hollow blocks. It was noticed, prior to failure, that buried wire and GFRP meshes were unharmed. The performance of the wire mesh was evident in the ductile failure of the EMW blocks. This was evident by the chipping and sliding of the face shell of the EMW blocks. Triangular spalls require more energy to form and suggest energy absorbing failure of the specimens (Vonk, 1993). The specimens were perfectly intact and failure was in a spongy manner.

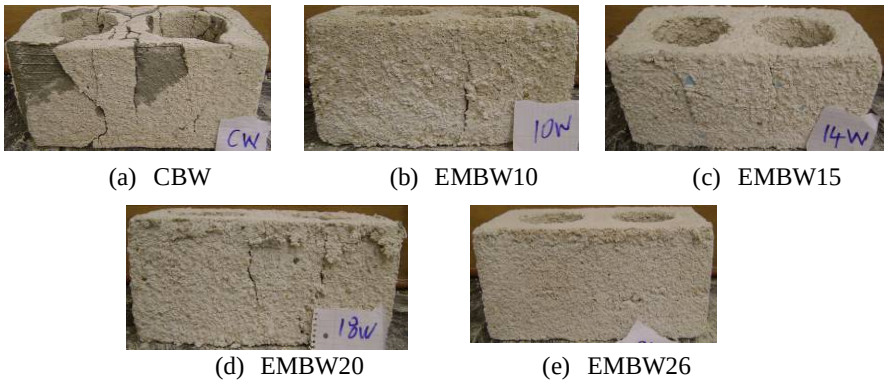

(a) CBW (b) EMBW10 (c) EMBW15

(d) EMBW20 (e) EMBW26

Figure 4.30: Failure pattern of ferrocement control and EPS mortar after wet-dry acid cycles

The glass fiber mesh produced more gradual failure pattern of the control block and all densities of the EM hollow blocks as illustrated in Figure 4.31. The gradual failure of the control blocks was characterized by the shear off of the fiber mesh and the block split into two pieces. The failure pattern of fiber glass hollow blocks with addition of EPS content was more improved than that of the ferrocement EM hollow blocks. This is attributed to the smaller mesh spacing of the fiber mesh. The more ductile failure was characterized by triangular cracks that indicate that compression failure was not the predominant cause and tensile failure also contributes to the ductility of the failure (Vonk, 1993). The softening of the loaded surface into slid triangular chips also proved the ductility of the failure especially in the EMF15 specimens. The cracks were almost invisible in specimens EMF20 and EMF26. In all cases the EM hollow blocks were intact volumetrically.

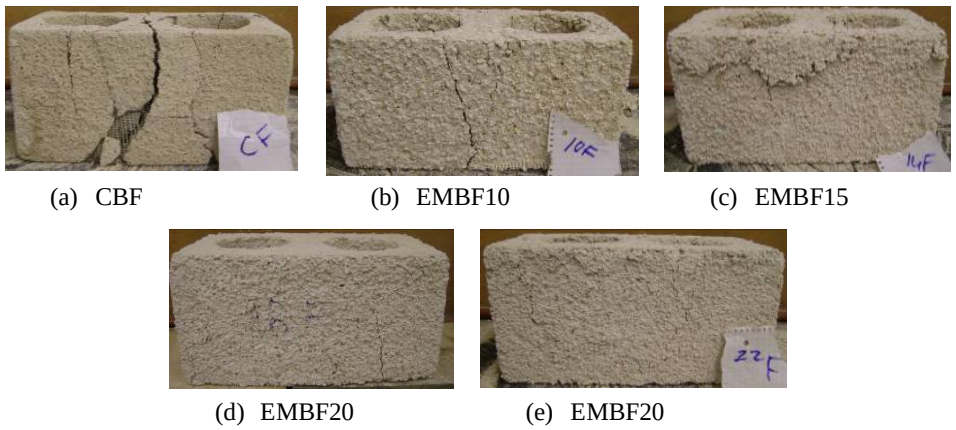

(a) CBF (b) EMBF10 (c) EMBF15

(d) EMBF20 (e) EMBF20

Figure 4.31: Failure pattern of fiber reinforced control and EPS mortar after wet-dry acid cycles

4.4.3 Soluble Chloride test results and discussion

The discussion of the test results of the soluble chloride wetting-drying cycles will be divided on three section:1-the effect of soluble chloride cyclic ponding on plain control and EM blocks, 2-its effect on ferrocement control and EM hollow blocks and 3- its effect on GFRP reinforced control and EM hollow blocks. This division was chosen because this type of test adversely affects the cement mortar, wire mesh and GFRP mesh through physical reactions and two different chemical reactions respectively.

4.4.3.1 Precipitation of salt and water retention and different absorption of salt water

Table 4.9 and Figure 4.32 show the rate of precipitation of salts and pore clogging observed on the tested blocks. It is evident that batches that had high saline solution absorption (Figure 4.33) have also high rate of salt precipitation. This is because absorption and precipitation are function in the porosity of the matrix. Block batches that showed a constant or decreasing rate of saline solution absorption indicate the presence of pore clogging by precipitated salts. On the other hand, blocks that showed increasing rate of saline water absorption may indicate the formation of micro-cracks due to salt crystallization and/or corrosion products. Saline solutions are more readily absorbed into the pores of the hollow block through the wetting cycles. On the other side, losing the absorbed water during the drying cycles was very slow. By the end of each drying cycle, some of the blocks would evidently have moisture content. In addition, the blocks never retrieved back their initial weight after the first wetting and drying cycle. During the drying cycles, surface water evaporated leaving behind salts in the concrete pores to precipitate and clog the surface pores which made water in the inner pores of concrete to remain trapped (water retention). With the progression of wetting and drying cycles, the mass difference between wet and dry specimens decreased and the specimens never returned back to their initial weight. Similar behavior was reported by R. P. Spragg et al, 2011.

Table 4.9: Cumulative rate of saline solution absorption and salt precipitation of the different types of control and EM blocks

Batch	Cumulative saline solution absorption (%)				Cumulative salt precipitation (%)			
	Cycle 1	Cycle 2	Cycle 3	Cycle 4	Cycle 1	Cycle 2	Cycle 3	Cycle 4
CBP	0.41	0.33	0.33	0.26	0.04	0.00	0.00	0.02
CBW	1.22	1.22	1.13	1.06	0.74	0.63	0.54	0.67
CBF	1.25	1.27	1.14	1.21	0.75	0.67	0.39	0.78
EMBP10	3.23	3.15	3.20	3.07	2.03	2.09	2.06	2.22
EMBW10	2.63	2.63	2.53	2.67	1.80	1.80	2.02	2.19
EMBF10	2.59	2.59	2.57	2.64	1.84	1.84	2.07	2.19
EMBP15	4.21	4.18	4.71	4.21	2.52	2.65	2.62	2.85
EMBW15	3.71	3.71	3.71	3.83	2.78	2.78	3.06	3.18
EMBF15	3.09	3.09	3.22	3.18	2.23	2.23	2.43	2.53
EMBP20	2.94	2.91	3.02	3.06	1.38	1.49	1.38	1.57
EMBW20	2.20	2.20	2.42	2.71	1.03	1.03	1.43	1.76
EMBF20	2.70	2.70	2.93	3.00	1.61	1.61	1.94	2.08
EMBP26	3.67	3.91	4.39	4.24	0.91	1.14	1.29	1.71
EMBW26	4.46	4.84	4.88	5.12	1.79	2.30	2.12	2.58
EMBF26	2.36	2.73	3.20	3.16	0.38	0.52	0.53	0.90

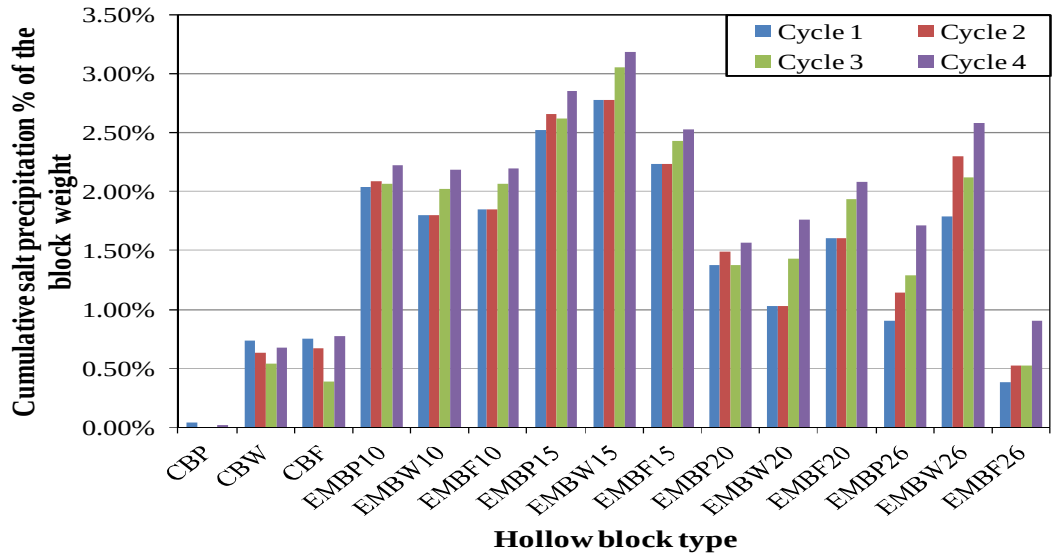

Figure 4.32: Cumulative salt precipitation in hollow blocks per cycles

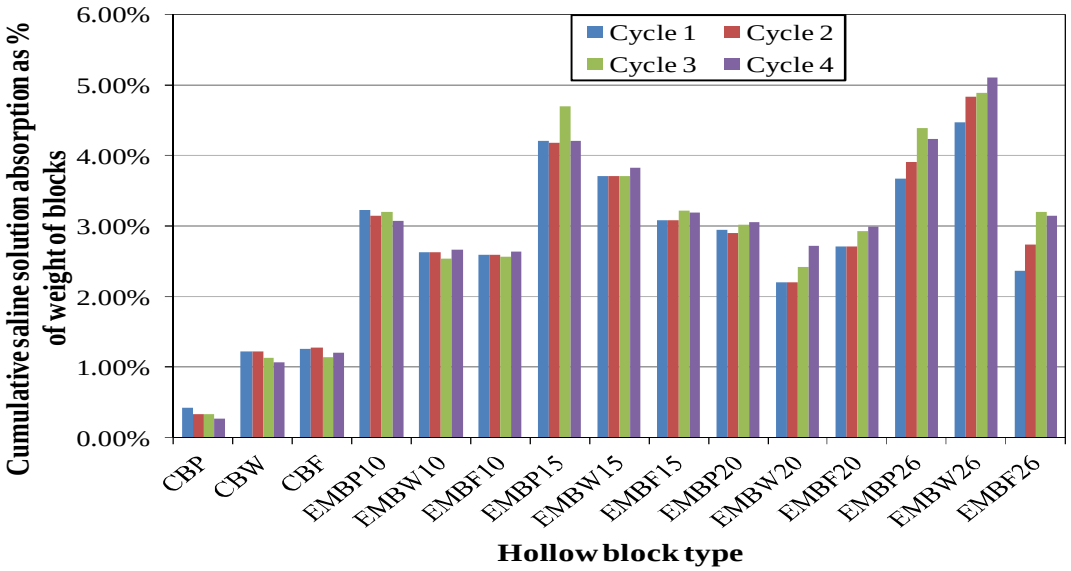

Figure 4.33: Cumulative salt water absorption of hollow blocks per cycles

4.4.3.2 Visual observations

Salt crystallization and efflorescence phenomena occurred in all hollow block specimens. By the second drying cycles, it was observed that the upper surface of the hollow blocks would be saturated with salt crystals that are adsorbed to surface pores. The surface would be shiny

with pieces of crystals. Also, efflorescence in the form of whitish streaks of salts accumulated on the block's surface and discoloration was noticed. The reason behind the crystallization of salts is that during the drying cycles of mortars subjected evaporation of surface water occurred. The moisture content near the mortars' surface decreased rapidly and consequently the concentration of salts increased in a similar rate. In addition, the surface drying stimulated the migration of water from inside the pores towards the mortars' surface. However, the crystallization of salts near the mortar's surface caused the transport of water from inside to the surface to diminish. The salt crystallization process took place on the surface of mortars and the amount of precipitated salts increased continuously with time. At the end of each drying cycle, thin-needle like crystals accumulated to form salt streaks were observed on the surface of all hollow block batches indicating the dense pore structure of the matrix and the crystallization of salts. Similar salt crystallization phenomena were reported earlier by Koniorczyk, 2010 and Lubelli, and R. de Rooij, 2009. The maximum amount of surface crystals and efflorescence was noticed on the control ferrocement hollow block specimens. The EM hollow blocks suffered less discoloration and whitish streaks were reduced to whitish patches and spots except for blocks made with EM26 mortars which showed the maximum deterioration due to salt crystallization. This may be attributed to the porous surface finish of the EM26 hollow blocks that helped foster salt crystallization. This behavior was contradictory to the low absorption characteristics of these blocks, which confirmed the assumption that the less absorption values of the EM26 blocks was due to the large amounts of the hydrophobic EPS particles in the mix and the blocks' surface. On the other hand, the extent of efflorescence in ferrocement control and EM blocks was the severest among the three types of blocks for all EPS contents. EM20 hollow blocks suffered the least of efflorescence deterioration. Figure 4.34 illustrates some control and EM hollow blocks suffering efflorescence.

(a) Control (CBF) (b) EMBW10 (c) EMBW26

Figure 4.34: Hollow blocks suffered from efflorescence due to salt crystallization.

4.4.3.2 Plain hollow blocks strength deterioration

Figure 4.35 and table 4.10 show the strength reduction occurred to control and EM hollow blocks subjected to cyclic chloride ponding. The reduction of strength in plain control and EM hollow block could be largely attributed to distresses and micro-cracks resulted from the salt crystallization phenomenon. It is obvious that the strength loss in plain control and EM hollow blocks was not affected by the EPS content. Higher ratios of EPS content in the blocks exhibit lower strength loss, although it is previously displayed that the water absorption of EM hollow blocks is higher almost 10 folds than that of the control blocks. This might be explained by low elastic modulus EPS particles have that would allow the expansion of mortars during salt crystallization without restraint. Also, EPS mortars have bigger pores between EPS and the matrix and have higher moisture transmission than conventional mortars which contributes in the responsive loss and gain of saline water without retaining much inside its pores for evaporation and expansion.

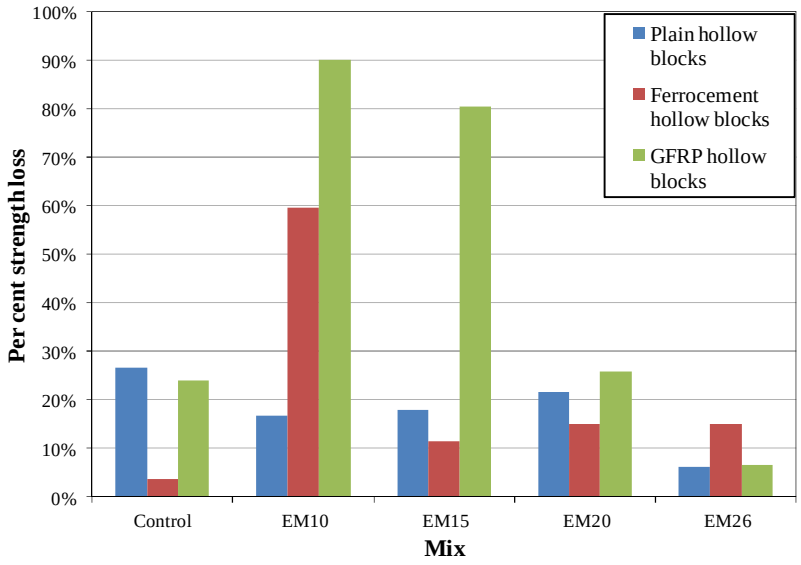

Figure 4.35: Average strength loss of all block batches after four wet-dry cycles of saturated NaCl ponding

Table 4.10: Strength loss incurred to the control and EM hollow blocks after wet-dry cycles of saturated NaCl ponding

Batch	Average Density (kg/m^3)	Strength loss (%)
CBP	2071.00	26.67
CBW	2075.51	3.71
CBF	2089.03	23.97
EMBP10	1704.04	16.69
EMBW10	1896.99	59.64
EMBF10	1808.63	90.15
EMBP15	1359.63	17.95
EMBW15	1456.10	11.43
EMBF15	1373.15	80.54
EMBP20	1211.76	21.57
EMBW20	1227.99	15.07
EMBF20	1231.60	25.74
EMBP26	945.79	6.11
EMBW26	960.22	15.05
EMBF26	962.47	6.47

4.4.3.3 Deterioration of ferrocement Control and EM Hollow Blocks

The aggressive cyclic chloride ponding caused corrosion to all the ferrocement hollow blocks. The corrosion was noticed as early as the first cycle of testing. The early cycles were characterized by the appearance of leached rust products from the face pores of the blocks. This could be attributed to the large surface pores between the cement coated EPS particles of different sizes. Surface shrinkage and high absorption rate are also responsible for the early corrosion. It is worth noting that the same degree of corrosion was noticed in control and EM hollow blocks, which confirms that the key player of durability of EPS mortars is the quality of mortar matrix. Early signs of corrosion were noticed on all ferrocement specimens

regardless the content of EPS in the block. The expansive corrosion products developed underneath the reinforcement strands caused the mortar layer to crack. Also, EPS particles inflected low restraining effect on expansive corrosion products and crystallized salts. The corrosion products accumulated and deformed the ribs of the face shell as shown in Figure 4.36. Corrosion cracks were also noticed and a combination between efflorescence and corrosion leach was observed as shown in Figure 4.36. The formation of oxidized leaks from the composite's pores indicated that the concentration of soluble chloride ions reached the threshold value when the passive layer was pitted. The wet and dry cycles supplied the chemical reaction with soluble chloride, moisture and oxygen respectively which accelerated the corrosion of the reinforcement bars. The portlandite ($Ca(OH)_2$) reacted with chloride ions (Cl^-) and reduced the pH level in the pore solution of mortars to pH 10 or below which disturbed the equilibrium between portlandite, calcium silicate hydrate and the pore solution. The passive layer was pitted, and with further wetting cycles, chloride ions continued ingression towards steel, and caused the formation of corrosion products that were expansive and subsequent cracks of mortar steel cover occurred.

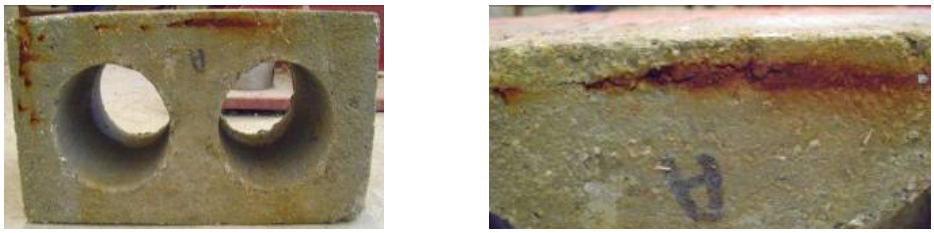

(a) Leached rust stains (b) Crack formation due to Expansive rust products

Figure 4.36: Deterioration of ferrocement hollow blocks due to wet-dry saline cycles

Table 4.10 and Figure 4.35 show the decrease in strength of ferrocement control and EM hollow blocks is lower than that exhibited by the plain ones except for mixes EM10 and EM26. The less effect corrosion has on strength deterioration agrees well with the discussion that wet-dry cycles reduce corrosion rate and that EPS mortars made with silica fume have high electric resistance. This also confirms that the quality of mortars determine to a great extent the corrosion behavior of the composite. However, higher strength loss inflected the EMBW10 hollow blocks could be attributed to the poor compaction and the presence of segregation during mixing which introduced larger pores in this batch. Moreover, the high content of EPS aggregates in batches EMBW26 produced a very rough finish where

reinforcement strands could be seen exposed from the blocks' faces. The inefficient steel cover aided the corrosion development and subsequent strength loss. The compressive strength of ferrocement hollow blocks made with the control, EM15 and EM20 batches was less affected than the plain ones made with similar batches. The confining effect of the reinforcement bars as well its load carrying capacity might have interfered to compensate for the strength lost by the cement matrix due to salt crystallization.

4.4.3.4 Deterioration of Glass Fiber Mesh Reinforced Control and EM Hollow Blocks

Although the GFRP mesh used in this research is alkaline resistant, the GFRP reinforced control and EM hollow blocks suffered the highest compressive strength loss as reported in Table 4.10 and Figure 4.35. The main deterioration factor was wetting and drying cycles in addition to the minor help provided by free chloride in altering the pore solution of the mortars and corroding the GFRP surface. Figure 4.35 demonstrate the sensitivity of GFRP EM hollow blocks to the quality of the mortar matrix and content of EPS. Comparing the effect obtained by the control fiber blocks and EMBF20 and 26 blocks shows that EPS may form a buffer zone of low permeability around the GFRP cage that decreases its leaching rate. It is fair to mention that the tremendously aggressive environment ailed to the failure of the glass fiber mesh which inflected sudden explosive failure of the mortar matrix. The wetting cycles induced a chemical reaction that caused hydroxylation of the glass fiber surface and resulted in pitting and embrittlement that deteriorated the tensile properties of glass fibers. The glass fiber degradation occurred due to the formation of a gel-coat of H_2SiO_3 (Silicic acid) that was formed due to the hydration and dissolution of glass fibers when subjected to moisture inside the pore solution of concrete. Karbhari et al, 2002 presented a more detailed of the deterioration of GFRP bars in high alkaline environments. The failure pattern will be explained sufficiently in the next section. The strength loss in specimens EMFB10 and EMFB 15 may be attributed to the increased permeability of these two batches more than the rest of the batches. The increased permeability would allow the more ingression of water and chloride to the glass fiber mesh and accelerate its deterioration. Also, the strength loss of glass fiber reinforced EM hollow blocks decreases significantly with the increase in EPS content. Although the GFRP hollow blocks did not exhibit any signs of severe deterioration—but for the salt crystallization—the deterioration of glass fibers in marine environment (cyclic wetting and drying of NaCl solution) is a complex kind of deterioration

that needs further research. The mechanism by which chloride ions and hydroxyl ions interacts with GFRP and mortar interface and the produced products is a recent field of research with very scarce information and analysis.

4.4.3.5 Failure Pattern of Plain control and EM hollow blocks

The increase in EPS dosage not only helped EM plain hollow blocks retain more strength than the control ones, but also increased the failure ductility as shown in Figure 4.37. The failure of the control blocks was a brittle one that was characterized by splitting longitudinal cracks. EMP10 specimens had a more ductile failure that was characterized by narrower longitudinal cracks and spall of the face shell. However, splitting cracks were also noticed on EMP10 specimens' failure. The blocks belonging to batches EMP15 and EMP20 exhibited more toughness that was manifested by a more ductile failure. Triangular spalls and chipped surface dislocations indicated a failure that absorbed lot of energy to occur. EMP26 blocks had almost no visible longitudinal cracks and failed by surface shell spall. A very significant pattern of behavior occurred at the start of the experiment. The blocks would release energy in a pop sound that causes the loading machine to kink and stop then reloads till failure. This behavior might be an indication of the distresses caused by crystallized salts clogging the pores of the blocks.

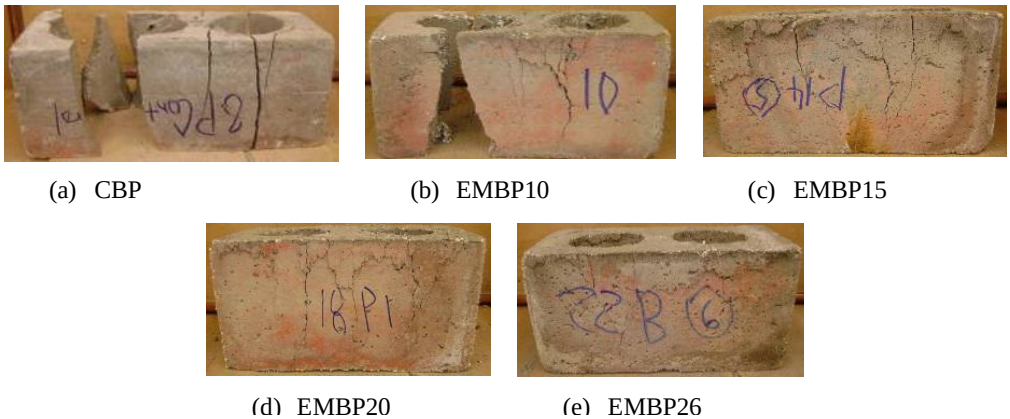

(a) CBP (b) EMBP10 (c) EMBP15

(d) EMBP20 (e) EMBP26

Figure 4.37: Failure pattern developed in plain hollow blocks after wet-dry saline cycles

4.4.3.6 Failure Pattern Ferrocement control and EM hollow blocks

The corrosion and salt crystallization was evident on all the ferrocement hollow block specimens as shown in Figure 4.38. The failure of ferrocement blocks was characterized by slippage in all specimens. This was noted when the loading machine kinked and stopped

loading at the beginning of the test. A pop sound was heard and the machine resumed loading till failure. Some specimens suffered more than one slippage incident during testing. Tensile failure occurred in batches CBW and EMBW10 which was characterized by brittle explosive failure. The cracks were tensile cracks (diagonal cracks) and wire mesh failed by either rupture or severe deformation. Specimens belonging to batches EMBW15 and 20 displayed a shift in toughness. The ductile failure was characterized by triangular dislocated spalls of the face shells. However, deep tensile cracks could still be noticed. Specimens EMBW26 showed failure by compressibility, no cracks were evident. It is worth noting that specimens EMBW20 and 26 showed decrease in their height in a compressed barreling failure. This behavior could be attributed to the internal micro-cracks developed by the salt crystallization and expansive corrosion products that were not restrained by the EPS particles.

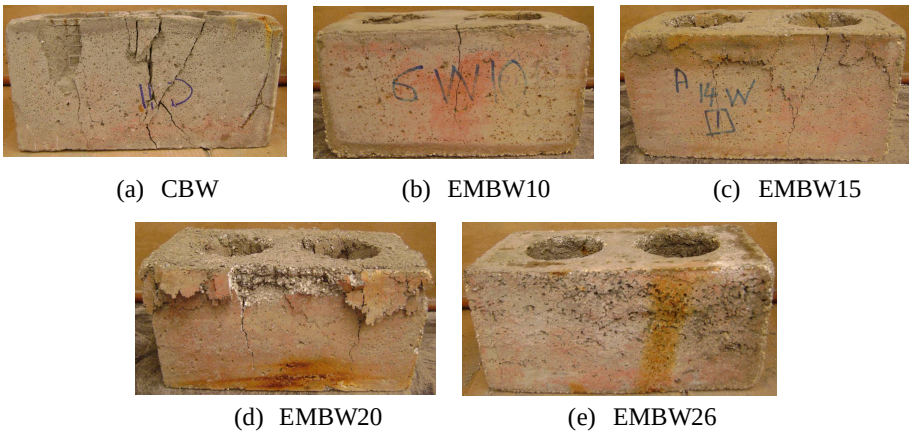

(a) CBW (b) EMBW10 (c) EMBW15

(d) EMBW20 (e) EMBW26

Figure 4.38: Failure pattern developed in ferrocement hollow blocks after wet-dry saline cycles

4.4.3.7 Failure Pattern GFRP control and EM hollow blocks

The GFRP blocks are the most interesting group of specimens. The degradation of GFRP cage initiated failure in the blocks. The failure of hollow block belonging to groups CBF, EMBF10 and EMBF15 was a brittle explosive failure. CBF blocks first suffered slippage of fiber then the composite block failed suddenly. Figure 4.39 shows shuttered pieces of mortar falling loosely off the GFRP cage in an indication of loss of bond. On the other hand, this partially composite action did not exist in blocks belonging to batches EMBF10 and EMBF15, rather, these blocks failed explosively due to the rupture of the GFRP cage. Deep tensile cracks existed and were localized around the rupture location of the fibers. On the

other hand, blocks belonging to batches EMBF20 and EMBF26 displayed a more gradual and ductile failure that was characterized by triangular slid spalls occurring on the face shell. However, tensile cracks would be still seen at the bottom section of these blocks (shear cracks).

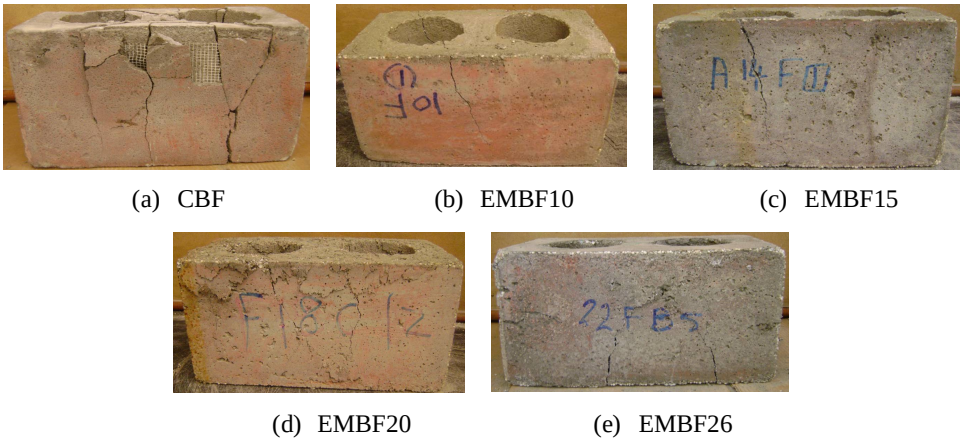

(a) CBF (b) EMBF10 (c) EMBF15

(d) EMBF20 (e) EMBF26

Figure 4.39: Failure pattern developed in GFRP hollow blocks after wet-dry saline cycles

4.5 Thermal Test Results and Analysis

This section analyses the thermal conductivity results obtained experimentally from the hot wire method. The effect of EPS dosage on the k-value is illustrated and the variation of k-value with EPS content and temperature is highlighted.

4.5.1 The EPS content effect on the k-value

The k-values of the control mix and four EPS mortar mixes measured at 50 and 70 degrees Celsius are presented in Table 4.11. Figure 4.40 presents the variation of the k-values with the density at 50 and 70 degrees Celsius. The results obtained show a general trend of the decrease of the k-value with the increase of the EPS content. This decrease could be explained simply by analyzing the contribution of each of the constituents of the composite to the k-value by using a rule of mixtures. The overall k-value could be mathematically calculated by proportioning the k-values of each of the composite constituents according to its contribution in the overall composite weight or as a percentage and applying the sum rule to the proportioned k-values (Marshall, 1972). The thermal conductivity of the control mix is 1.8 W/m. K at 50 degrees Celsius, while the thermal conductivity of EPS beads as reported by Incropera and DeWitt, 1996 is 0.04 W/m. K at 27 degrees Celsius. Applying a simple rule

of mixture, EPS decreases the density of mortars as compared to the control mix by 24, 30, 39, and 55 per cent for mixes EM10, EM15, EM20 and EM26 respectively. This means that these percentages of density of solid quartzite sand, which has a very high thermal conductivity of 8.6 W/m. K (Khan, 2002) was replaced by cellular solids of negligible thermal conductivity.

Table 4.11: The k-value of the control and four EPS mortar mixes measured at 50 and 70 degrees Celsius

Mix	Density (kg per cu m)	Average Thermal Conductivity (k-value)	
		Temperature in degree Celsius	
		50	70
Control	2200	1.80	2.15
EM10	1680	1.53	1.47
EM15	1550	0.99	0.94
EM20	1350	0.56	0.29
EM26	980	0.16	0.29

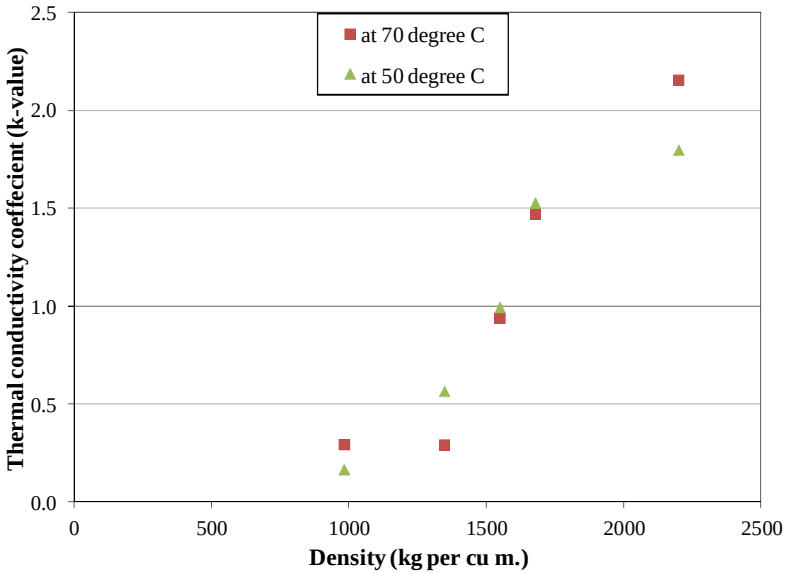

Figure 4.40: The K-value measured at 50 and 70 degrees Celsius of all mixes

4.5.2 Temperature and moisture effect on the k-value of the control mix

It was previously shown that the absorption of EPS mortar changes insignificantly with the increase of the EPS dosage. However, because the specimens were not conditioned at 100-110 degrees Celsius as recommended by ASTM C642, their pore structure inevitably was susceptible to moisture content either remnant of the curing process or from the prevailing atmospheric conditions. The significance of moisture in specimens affected the results of the k-values of the control bricks. This phenomenon could be explained by the fact that the adsorbed moisture to the pores of the materials consumed some of the heat generated by the electric current passing through the hot wire. As a result, the effective heat dedicated to increase the temperature of the solids was more than otherwise have been in case of a bone-dry specimen, and the rise of temperature at a fixed distance from the wire was lower than that expected in bone-dry specimens (dos Santos, 2003). In experimental practice, the k-value was thus apparently higher than expected.

4.5.3 Temperature and moisture effect on the k-value of EPS mortars

Although it has been shown in the previous section that the k-value of the specimens were supposed to be increasing as the measuring temperature increases from 50 to 70 degrees Celsius, the k-value of the EPS mortar decreased on this temperature range. The k-values of the EPS mortar mixes presented in Table 4.11 decrease with the increase of the tested temperature. At 70 degrees Celsius, the surface EPS combusted, leaving air in place, thus reduced the k-value of the brick. The thermal conductivity of air at 27 degrees Celsius is 0.0263 W/m. K (Incropera and DeWitt, 1996) which is lower than that of EPS measured at the same temperature. Furthermore, the vast variation between the k-value measured for the EM20 mix at 50 and 70 degrees Celsius might be due to the heat release by the thermal decomposition of the surface EPS beads. The average heat resulting from the thermal degradation of EPS is 800 J/g (Kannan et al, 2007). To help quantify this amount of heat; 4.186 J are needed to raise the temperature of 1 g of water by 1 degree Celsius. This heat release would increase the ambient temperature of the test specimen as well as the temperature of the specimen itself. Kligys, et al, 2008 reported that as the amount of EPS in cement matrix increases, the heat release increases during the combustion of the beads. The more the EPS concentration produces more heat evolving from their combustion. This

explains the vast variation between the k-value at 50 and 70 degrees observed for EM26 specimens. In reverse to what happened in the presence of moisture, the added heat would mean that less energy was needed by the platinum wire to raise the temperature of the tested specimen than if otherwise the heat of degradation did not exist. This explains why apparently; the k-value is lower with the increase of the temperature at which it is measured. The combination of specimen conditioning and instrumentation limitations and heat of degradation had their toll over the k-value measured for the EM20 and EM26 mixes. Because the volume around the platinum wires became tremendously porous and heated with the heat of degradation, the k-value at 70 degrees Celsius is measured as double that of the one measured at 50 degrees Celsius. As a result, it is better to ignore the k-value obtained at 70 degrees Celsius for the EM20 and EM26 specimens. After the test termination at 70 degrees Celsius, it was noticed that the bricks had surface pores that took the shape of EPS particles which was evidence that EPS particles shrunk and evaporated at a temperature around 70 degrees Celsius. The pores resulting from the softened EPS surface particles are shown in Figure 4.41. There are several explanations to the premature thermal degradation of EPS particles. Although the thermal degradation of EPS is independent of its shape and polymer density, it is dependent on the additives used during its manufacturing, the number of weak bonds, the method of synthesis, etc (Kannan et al, 2007). Therefore, it is recommended to do some pyrolysis tests on samples of EPS to map the kinetics of its thermal decomposition. It is safe to note that the combustion of EPS particles embedded in the surface of EPS mortars occurred around 70 degrees Celsius. Kligys, et al, 2008 reported that combusted EPS crush left cavities in the aerated cement matrix.

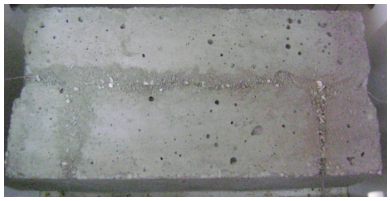

Figure 4.41: Pores resulting from the softening and shrinking of surface EPS aggregates of prisms made from mix EM20

Chapter 5

Numerical Model for Determining Thermal Characteristics

5.1 Introduction

The instrumentation required to measure the thermal conductivity of hollow block units is very limited in Egypt. Only one environmental chamber operating by means of guarded hot box method is available in Housing & Building National Research Center and it measures the U-value, which is the overall thermal conductivity of walls. The only obvious solution was to either construct a guarded hot box, which requires strict quality control and expertise or opt for numerical modeling of heat transfer behavior of hollow blocks.

5.2 Mathematical formulation

The heat transfer problem comprises the conduction and radiation equations in the solid phase and cavity wall respectively and the flow equations in the fluid phase (air). The problem is simplified by implementing the Boussinesq assumption, which means that viscous dissipation in fluid is neglected and the motion of air is solely due to variation in its density due to differential temperature of the walls of the cavity induced by the two isothermal surfaces. In other words, air density is temperature dependant. The governing equations are presented below (Ait-Taleb et al, 2008, Al-Hazmy 2006 and Sun and Fang 2009).

For the solid walls, the conduction equation applies:

$$\frac{\partial}{\partial x}\left(K_s \frac{\partial T}{\partial x}\right)+\frac{\partial}{\partial y}\left(K_s \frac{\partial T}{\partial y}\right)+\frac{\partial}{\partial z}\left(K_s \frac{\partial T}{\partial z}\right)=0 \qquad (1)$$

For air-filled enclosure, the following equations apply for convection:

The continuity equation

$$\frac{\partial u}{\partial x}+\frac{\partial v}{\partial y}+\frac{\partial w}{\partial z}=0 \qquad (2)$$

The momentum in the x-direction:

$$\rho\left(u\frac{\partial u}{\partial x}+v\frac{\partial u}{\partial y}+w\frac{\partial u}{\partial z}\right)=\frac{\partial P}{\partial x}+\mu\left(\frac{\partial^2 u}{\partial x^2}+\frac{\partial^2 u}{\partial y^2}+\frac{\partial^2 u}{\partial z^2}\right) \tag{3}$$

The momentum in the y-direction:

$$\rho\left(u\frac{\partial v}{\partial x}+v\frac{\partial v}{\partial y}+w\frac{\partial v}{\partial z}\right)=\frac{\partial P}{\partial y}+\mu\left(\frac{\partial^2 v}{\partial x^2}+\frac{\partial^2 v}{\partial y^2}+\frac{\partial^2 v}{\partial z^2}\right) \tag{4}$$

The momentum in the z-direction:

$$\rho\left(u\frac{\partial w}{\partial x}+v\frac{\partial w}{\partial y}+w\frac{\partial w}{\partial z}\right)=\frac{\partial P}{\partial y}+\mu\left(\frac{\partial^2 w}{\partial x^2}+\frac{\partial^2 w}{\partial y^2}+\frac{\partial^2 w}{\partial z^2}\right)+\rho_c g\beta\left(T-T_c\right) \tag{5}$$

The energy equation:

$$\frac{\partial T}{\partial \tau}+u\frac{\partial T}{\partial x}+v\frac{\partial T}{\partial y}+w\frac{\partial T}{\partial z}=\alpha\left(\frac{\partial^2 T}{\partial x^2}+\frac{\partial^2 T}{\partial y^2}+\frac{\partial^2 T}{\partial z^2}\right) \tag{6}$$

Rayleigh's number equation:

$$Ra=\frac{g\beta H^3\Delta T}{\nu^2}\Pr \tag{7}$$

The Boussinesq assumption:

$$\rho=\rho_c\left[1-\beta(T-T_c)\right] \tag{8}$$

For enclosure walls, the following equations apply for radiation:

The dimensionless radiative Q_r heat flux to the radiative heat q_r (W/m^2) by:

$$Q_r=\frac{q_r}{\sigma\Delta T_0^4} \tag{9}$$

The radiative heat $q_{r,k}(r_k)$ is a function in the radiosity $J_k(r_k)$ and incident radiative heat flux $E_k(r_k)$ on surface. The heat flux exchanged between two surfaces: the finite area dS_k located at position r_k and surface k, is defined by the following equation:

$$q_{r,k(rk)} = J_r(r_k) - E_k(r_k) \tag{10}$$

The radiosity equation:

$$J_k(r_k) = e_k \sigma \left(T_k(r_k)\right)^4 + (1 - e_k) E_k(r_k) \tag{11}$$

The incident radiative heat flux equation:

$$E_k(r_k) = \sum_{j=1}^{4} \int_{Aj} J_j(r_j)\, dF_{dSj - dSj\,(rk, rj)} \tag{12}$$

5.2.1 Post-processing equations

The following equations are used to evaluate the equivalent thermal conductivity obtained numerically:

$$q = rate\, of\ heat\, transfer \left(\frac{W}{m^2} \left(m^2\right) \right) \tag{13}$$

$$Q = \frac{q}{A} \left(\frac{W}{m^2} \right) \tag{14}$$

$$K_{eq} = W \times \left(\frac{Q}{T_h - T_c} \right) \ in\ W/m.K. \tag{15}$$

5.3 Boundary conditions

The main building block of the thermal model represents half a block and is exhibited in Figure 5.1. The height, width and length are equivalent and equal to 0.2 m. the diameter and height of the cylinder are 0.125 m and 0.2 m respectively. In the x-direction, the right-side rib has a width of 0.025 m and the left-side one has a width of 0.05 m. In the y-direction, the two upper and lower withes have an equivalent width of 0.0375 m.

All the elements are wall elements. The outer and inner surfaces of the wall are isothermal surfaces and are kept at constant temperatures, T_h=50 and T_c=25. The surface exterior to the wall at x=0 is maintained at a constant temperature of 50 degrees Celsius (323 K) while the interior's surface is kept at a constant temperature of 25 degrees Celsius (298 K). The left and right sides, bottom and top of the block are adiabatic surfaces at y=0, y= 0.2, z=0 and z=0.2 respectively. Adiabatic surfaces mean that the surfaces are insulated and do not allow the gain or loss of heat.

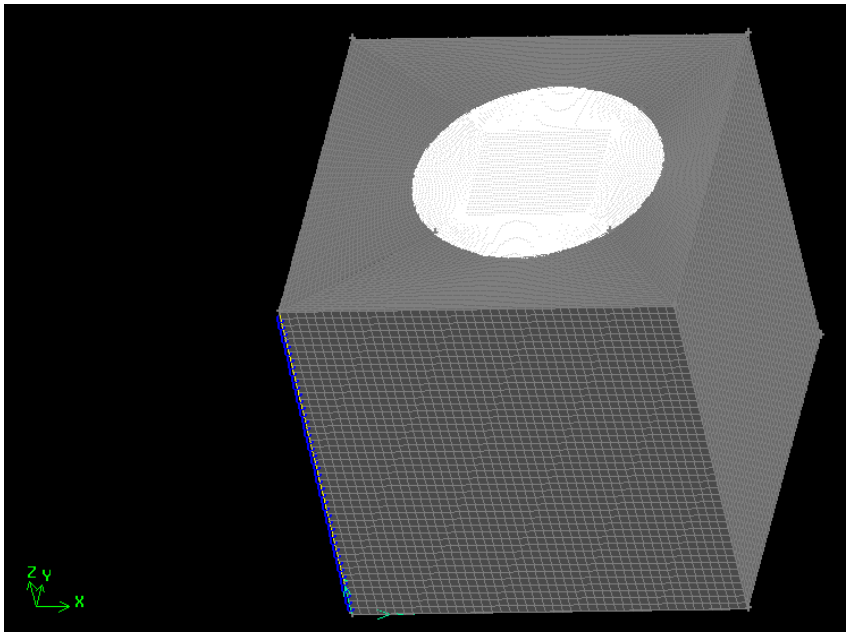

Figure 5.1: A 3-D representation of half a block was used to model the heat transfer problem of the EPS hollow blocks

5.3.1 Operating conditions

The 3-D model drawn on GAMBIT had the fluid and solid phases defined so when read by FLUENT, the conduction shells were automatically defined. The convection and radiation phases were defined manually to simulate the heat transfer problem accurately.

The motion of air in the cavity is assumed to exhibit laminar flow in a steady state. The Bousinesq assumption was implemented in the operating conditions. The gravitational acceleration was activated and was given a value in the z-direction only to be -9.81 m/s^2. The

operating density of air is assumed 1.225 kg/m^3. The non-slip condition was activated to ensure that the velocities at the walls of the cavity were zero.

The radiation model selected for this problem was the surface-to-surface (S2S) model. It is particularly suitable because it is used for the calculation of radiative transfer in enclosures without the presence of a participating medium, (a medium that participates in the radiation heat by emitting, absorbing and reflecting heat like smog in a factory flue for example). It assumes that all surfaces of the enclosure are gray and diffuse. However, it is time and space costly in the computation of the view factor especially that the model is 3-D. To speed up this process, the amount of radiating surfaces is decreased in a process called surface clustering. The view factor and surface cluster parameters were hemi cube and surface smoothing to increase the accuracy of computation.

5.4 Simulation

Five main models were generated in FLUENT; each was run with 4 different scenarios, namely: 1-conduction, 2-conduction and radiation, 3-conduction and convection and 4-conduction, convection and radiation. The material properties of the fluid phase are the same for all five models and are defined as air of Boussinesq density and thermal expansion β of 0.003356 (K^{-1}). The material properties of solid phase are defined as that of the five mixes studied in this thesis, namely: the control, EM10, EM15, EM20, and EM26. Only the density and the coefficient of thermal conductivity were altered for each model as was determined experimentally. The specific heat and emissivity were kept constant at 840 (J/kg .K) and 0.94 respectively. Although it was previously mentioned that EPS improves significantly those properties, the difficulty of experimentally obtaining them invoked this assumption.

The conduction-convection-radiation heat transfer scenario was obtained by enabling the gravitational acceleration, Boussinesq model with a specified thermal expansion of air and the radiation model S2S. The conduction-convection heat transfer scenario was achieved by disabling the radiation models in general. The conduction heat transfer scenario was achieved by disabling both the gravitational acceleration (making air stagnant) and the radiation model.

The heat transfer problem was initialized by setting all zones at relative average temperature of 37.5 degrees Celsius (310.5 K) and setting air motionless by zeroing all the velocities and

pressure. For solution controls, the discretization options selected for pressure, momentum and energy were PRESTO!, QUICK and QUICK respectively. The pressure-velocity coupling was done by the SIMPLE algorithm.

5.4.1 Grid dependence simulation

The mesh selected for the modeled module was structured mesh. A breakdown of the 3-D model into a basic geometry was implemented to be able to perform structured meshing (figure 5.2). The basic model shown in Figure 5.2 was used to generate five models of different mesh refinement in GAMBIT. The meshing scheme was quadrilateral of the type map and brick elements were produced of minimum skewness. The mesh was examined and the produced report indicates it was of good quality. Figure 5.3 shows a green histogram which is accumulated at the left side as a sign of the good quality of the mesh. The volume of the block was created by sweeping the meshed faces about the z-axis, which in turn was also meshed a priori.

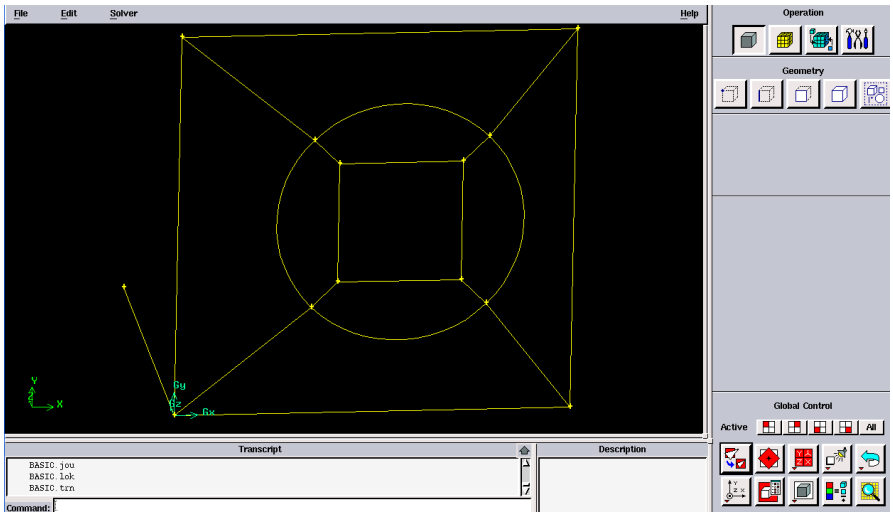

Figure 5.2: The basic geometry for the generation of structured mesh.

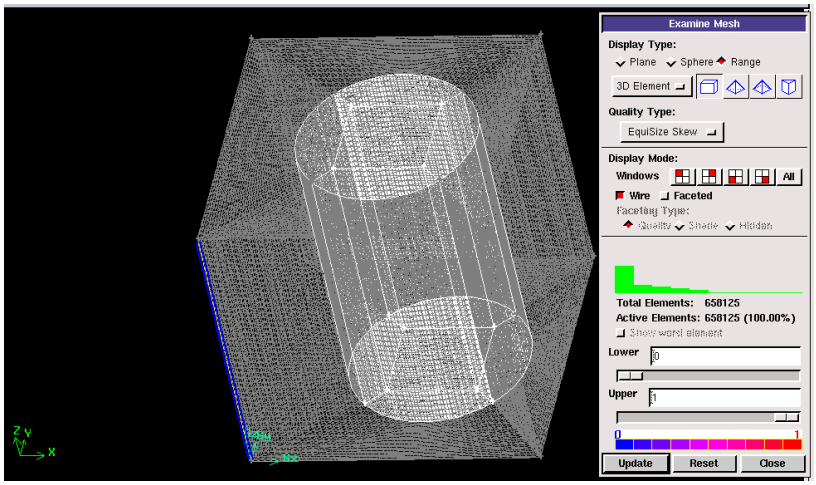

Figure 5.3: 3-D module of the hollow block. The green histogram on the left indicate a good quality mesh.

The accuracy of the results is associated with fine meshing. However, the fine the mesh could get is also a function in its cost in terms of solution conversion time and computer processing space. Five mesh sizes were selected for grid dependency testing as shown in table 5.1 and Figure 5.4. The difference between the heat transfer rates was diminishing starting from case 3 till case 5, which was the most expensive in terms of computation time and space. Therefore, case 3 was selected to represent the module of the numerical problem as it produces the most accurate results with the least expensive cost.

Table 5.1: Cases tested for mesh sensitivity estimation

Case	No. of nodes	Total heat transfer (W)
1	42,861	7,15
2	95,576	7,12
3	178,591	7,11
4	676,936	7,10
5	948,651	7,10

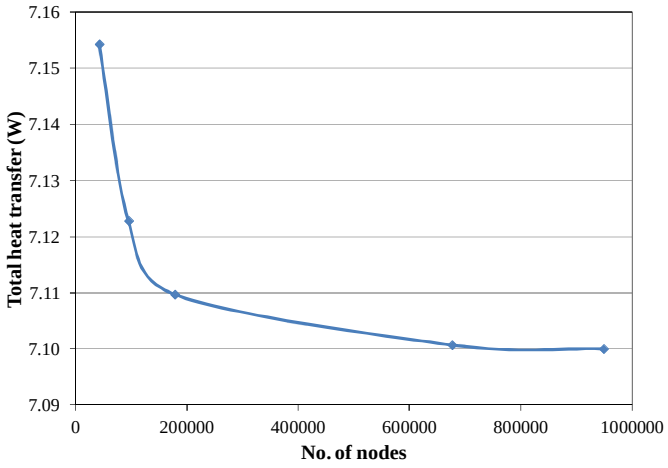

Figure 5.4: The plot shows the mesh sensitivity towards the number of meshed elements.

5.4.2 Code Validation

The geometry the hollow blocks discussed in this research is not abundantly discussed in literature. Therefore, the model's validation was done on the selection of a representative module, the boundary conditions and the mesh density. The 3-D validation model represents half a commercially available concrete hollow block with the cavity asymmetric to the conductive shell. Figure 5.5 represents a schematic of the validation model, which bore the same boundary conditions, mesh density, and physical parameters of the constituting materials as that of the control mix. Two types of validation are discussed in this section, namely, validating against numerical and experimental results.

The Nusselt's number for the conduction-convection mode was obtained numerically and compared to values in literature for Ra $=10^6$ and Pr=0.7 for the given grid size. Nusselt's number is a parameter that defines the dimensionless temperature gradient at a surface (Incropera and DeWitt 1996). Its importance lies in the fact that it provides a measure of the convection heat transfer at a surface (Incropera and DeWitt 1996). The following equations were used in numerically computing Nusselt's number (De Vahl Davis 1983, Balaji and Venkateshan 1993, and Barakos and Mitsoulis 1994)

$$Nu_x = \int_0^1 Q(x,z)dz \qquad (16)$$

$$\overline{Nu} = \int_0^1 Nu_x dx \qquad (17)$$

The mean Nusselt's number is 8.3, which agrees well with the mean Nusselt's number estimated by the benchmark solution with just 3.6 % error (De Vahl Davis 1983).

The second method of is against experimental results. The numerically obtained total equivalent thermal conductivity yielding from running the conduction-convection-radiation scenario was 1.32 W/mK. The equivalent K-value of commercial concrete hollow blocks, same dimensions and material is 5.23 and 9.8 per cent error with experimental results cited by Baig, 2008 and VanGreen 1986 respectively. The error limited are acceptable given that uncertainty—experimental error—lies in the vicinity of 6.13% to 6.92% (Al-Hadhrami and Ahmad 2009).

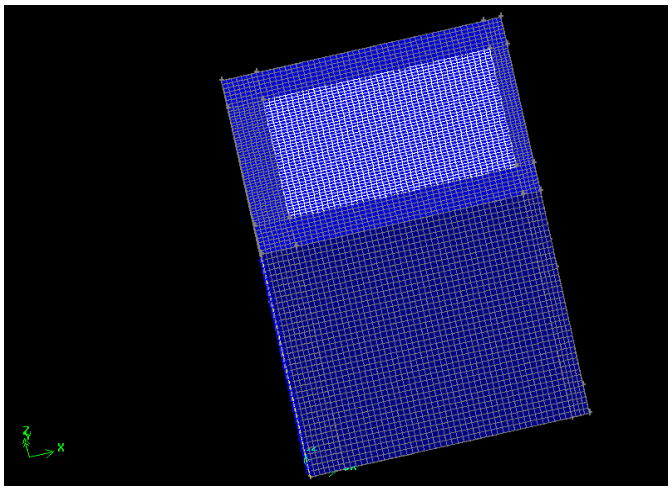

Figure 5.5: A schematic of the 3-D model representing a module of the commercially available concrete hollow blocks.

5.5 Results and discussions

The equivalent thermal conductivities of the different types of EPS hollow blocks are presented in Table 5.2 and Figure 5.6. The effect of air movement in the enclosure is evident from the difference between the k_{eq} obtained from the conduction and that obtained from convection-conduction scenarios. Also, the effect of radiation is evident from the difference in the Keq-values obtained from the all-modes and the conduction-convection scenarios. The

lowest K_{eq} –values are that obtained from the conduction mode, while the highest is that of the prism for high EPS mortar densities and that obtained from all-heat-transfer modes scenario for lower densities.

The difference between the total equivalent thermal conductivity (K_{tot}) obtained from the all-heat-transfer-modes scenario and the K-value of prisms decreased significantly with the decreased with the increase in the density of the mixes. The presence of cavities in blocks made with mixes EM20 and EM26 may prove to be futile and degenerative as the K_{tot} values obtained from the conduction mode were higher than that obtained from the solid prism. However, more light will be shed on the effect each mode of heat transfer separately in the coming sections.

Table 5.2: Results of K_{eq} obtained from the three different run-scenarios as compared with the experimental K-value of the solid bricks

Batch	Density (kg/m3)	Experimental Bricks' thermal conductivity (Ks)	Numerical analysis results of different modes of heat transfer scenarios		
			all modes of heat transfer	Conduction and convection only	Conduction only
Control	2200	1.80	1.43	1.14	0.97
EM10	1678	1.53	1.27	0.99	0.83
EM15	1549	1.00	0.94	0.71	0.54
EM20	1347	0.57	0.63	0.46	0.32
EM26	982	0.17	0.25	0.19	0.10

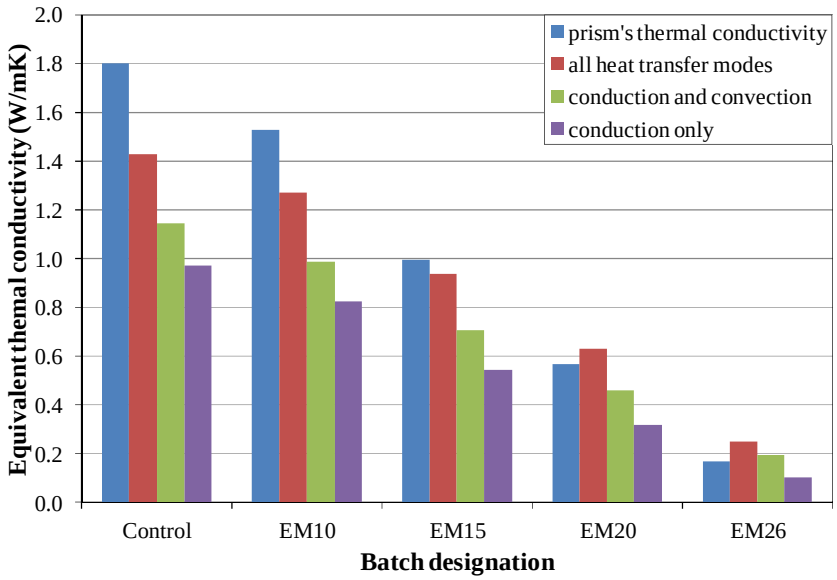

Figure 5.6: K_{eq} of different hollow blocks obtained from the numerical simulation scenarios

5.5.1 The conduction mode

In this mode the air is assumed stagnant as well as the solid phase is assumed not to reflect, absorb or emit any incident radiation rays. The thermal resistance of the hollow block module is merely the summation of a series and parallel R-values of fluid and solid phases analogical to an electrical cell resistance. The K_{cond} obtained is lower than that of the prisms' for all densities because the thermal conductivity of stagnant air is almost ten folds that of EM26, and air constitutes 30% of the volume of the module block.

When compared to the other two heat transfer scenarios, the K_{cond} is very low; however, it is the dominating mode of heat transfer as shown in Figure 5.6. The conduction mode decreases linearly with the decrease in the solid's thermal conductivity. A decreasing K-value means an increasing thermal resistance. Also, the gap between the contributions of the equivalent K-value of the three phases diminishes with the decrease in the solid's K-value. The lighter EPS composites EM20 has the less gap between K_{cond} , K_{conv} , and K_{rad} implying that the conduction, radiation and convection phase are sharing power in contributing to the total equivalent thermal conductivity. Mix EM26 is characterized by the balanced contribution of the three equivalent K-values.

The conduction K-value (K_{cond}) attributes to 32 to 58% of the total equivalent K-value (K_{tot}) obtained from the three modes of heat transfer. This suggests that the controlling heat transfer mode in this research is conduction. The per cent contribution of K_{cond} increases with the decrease in the prisms' thermal conductivity. The largest contribution of K_{cond} is done by mixes EM20 and EM26 at 49.6% and 57.9% respectively. This suggests the balancing of the three modes of heat transfer in lighter EPS hollow blocks.

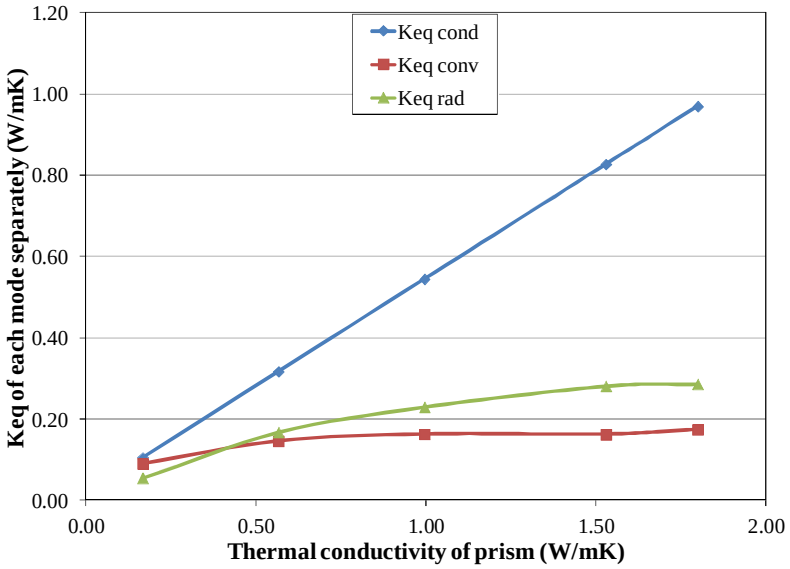

Figure 5.7: the contribution of each heat transfer modes' K_{eq} in total equivalent thermal conductivity (K_{tot})

5.5.2 The effect of convection

The effect of convection in the heat transfer in hollow blocks is significant and cannot be practically ignored. The addition of the convection mode increased the K_{eq} value as compared to that obtained from the conductive mode only for all the EPS mortar mixes as shown in Figure 5.6. Figure 5.7 shows the rate of heat transfer contributed by the convection mode (Q_{conv}). The contribution of Q_{conv} ranges between 12.16 to 36.14% for blocks made from the control and EM26 mixes respectively.

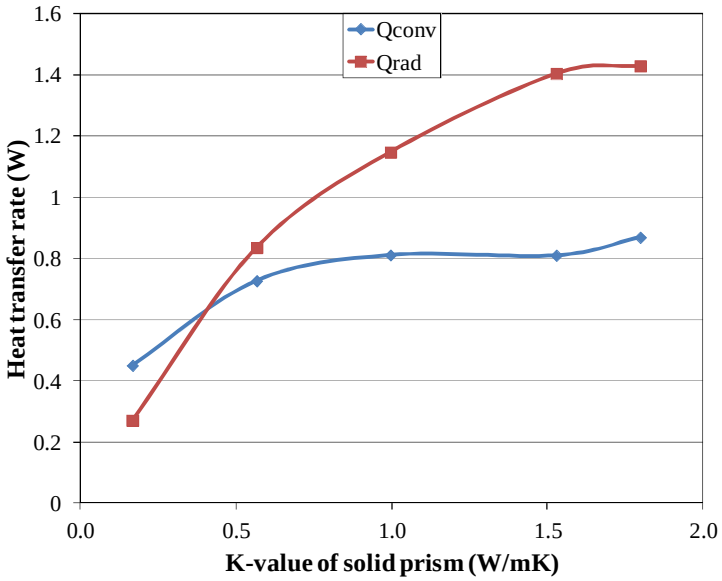

Figure 5.8: Convective and radiative heat transfer rates decrease with the decrease in the solids K-value

The movement of air upwards at the heated side and downwards at the cooled side induced air circulation in a cellular motion. This is evident from the isotherms gradient shown in Figure 5.8. The isotherm gradient falls sharply near the hot and cold surface of the cavity indicating the presence of a cellular motion due to buoyancy (Al-Hazmy, 2006). Figure 5.8 shows the temperature gradient of a horizontal line passing through the midpoint of the isothermal surfaces located at the mid height of the hollow block (in ratios: z=0.5, x=0.5, 0<y<1). A comparison between hollow blocks of the control and EM20 mixes is drawn in this figure. The cavity is starts at y=0.0375 m and ends at y=0.01625 m, near these points, the temperature gradient steeply drops till a constant value, where the air is stagnant in the middle of the cavity away from its walls. The effect of the k-value of solids is manifested in the steepness of the temperature gradient in the solid phase and near the cavity walls in the fluid phase. The EM20 blocks exhibit steep gradient in temperature as compared to the control blocks. Also, the cavity wall temperature is 319.9 K at the hot wall and 301.015 at the cold wall as compared to 321.4 K and 299.6 K for the control blocks' counterparts. The steep gradient in temperature showed by EM20 blocks could be explained by the hypothesis that EPS mortar has lower thermal mass than conventional mortars. It is relevant to add that EPS is expected to decrease the specific heat capacity of the EPS mortar, however, for the lack of

experimental data, their specific gravities are assumed to be equivalent. Although, adjusting the specific gravity would yield steeper results for the EM20 blocks in the conduction zones. The higher temperature exhibited at cavity's the cold wall could be explained by the steep gradient existing in the conduction solid phase. The higher velocity of air circulations assist in the transmission of heat through air, and vice versa. Figures 5.9 through 5.15 display the velocity magnitude vectors, vortices (air spinning) in the y- and z-directions for the control and EM20 hollow block respectively. The values obtained by the EM20 blocks are lower than that obtained by the control ones. The difference in cavity wall temperature between the EM20 and the control hollow blocks explains the less Q_{conv} exhibited by the former than the latter. Similar centerline heat distribution in a single cavity hollow block module were obtained and discussed in Baig, 2008.

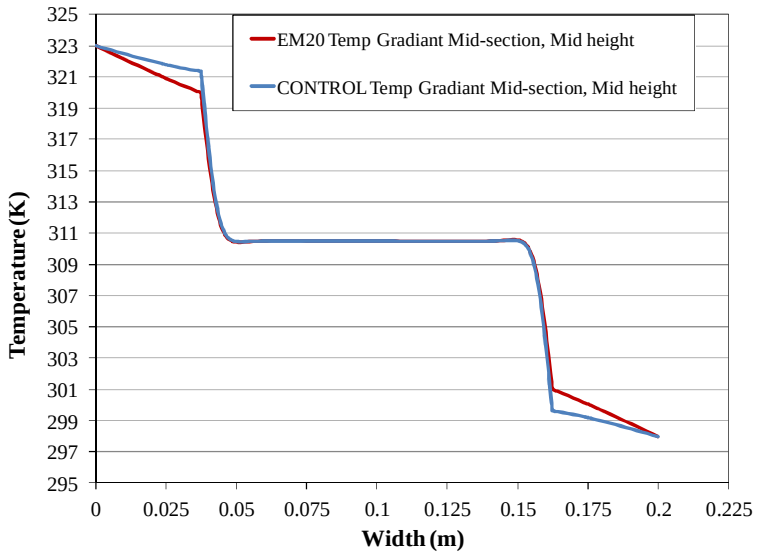

Figure 5.9: Temperature gradient at z=0.5, x=0.5, 0<y<1, through the control and EM20 hollow blocks.

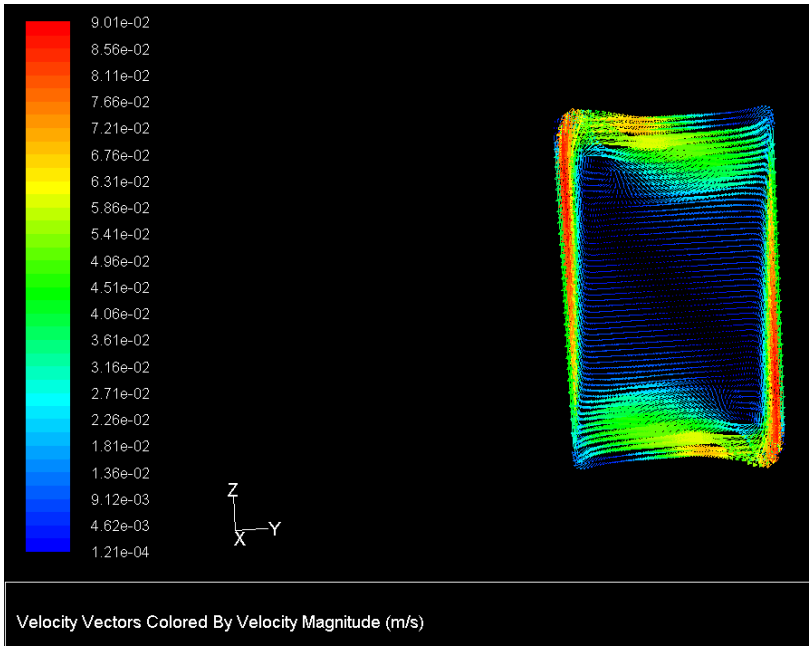

Figure 5.10: Velocity vectors magnitude obtained from the control hollow blocks in the direction of temperature gradient.

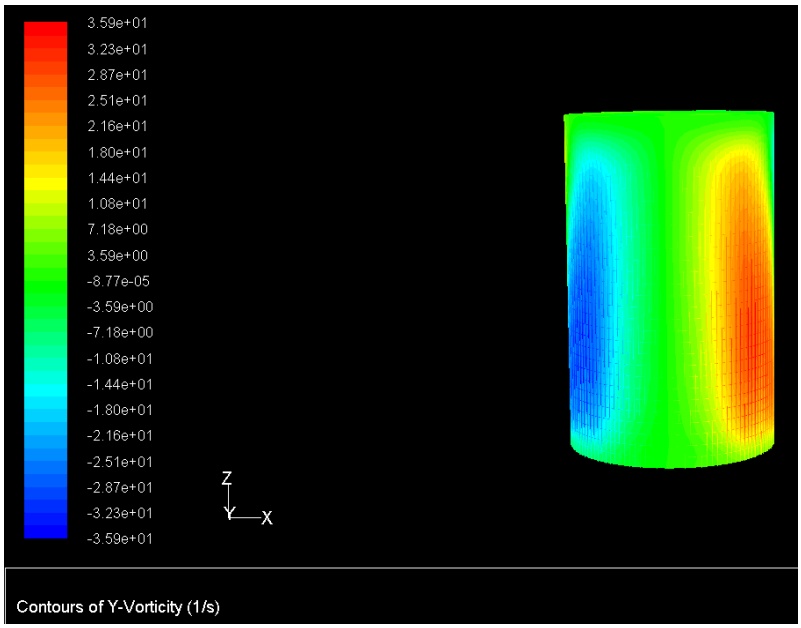

Figure 5.11: Vorticity obtained from the control hollow blocks in the direction of temperature gradient.

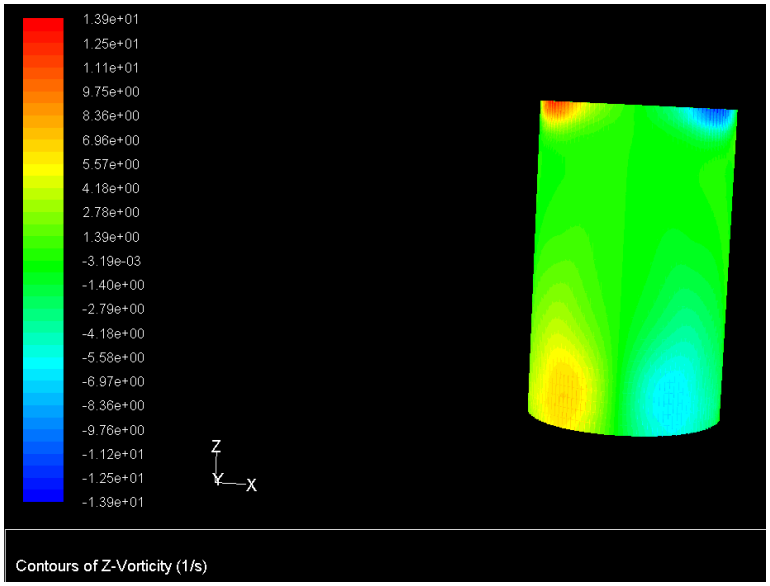

Figure 5.12: Vorticity obtained from the control hollow blocks in the z- direction.

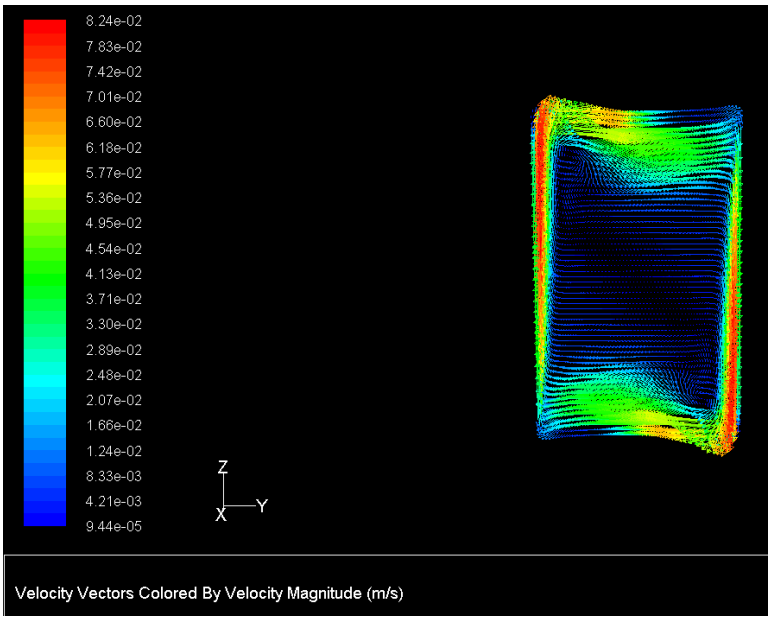

Figure 5.13: Velocity vectors magnitude obtained from the EM20 hollow blocks in the direction of temperature gradient are less than those exhibited by the control ones.

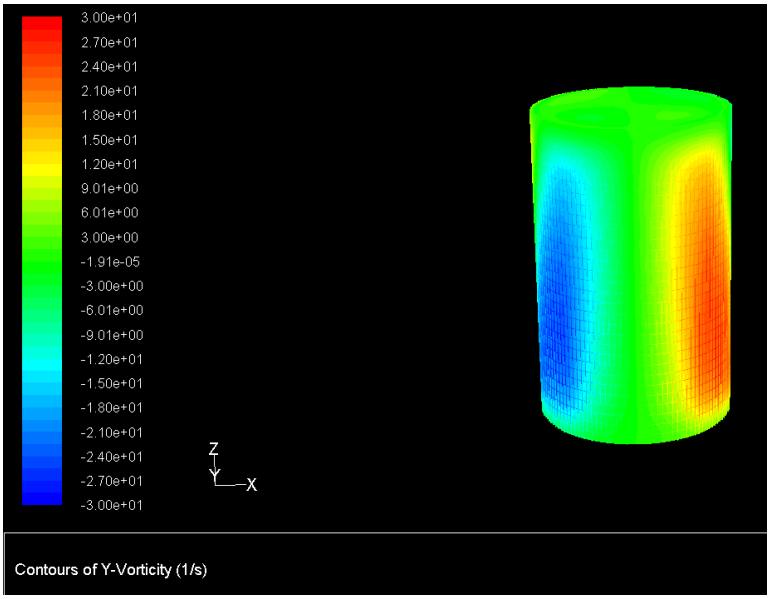

Figure 5.14: Vorticity obtained from the EM20 hollow blocks in the direction of temperature gradient is less than those developed by the control ones.

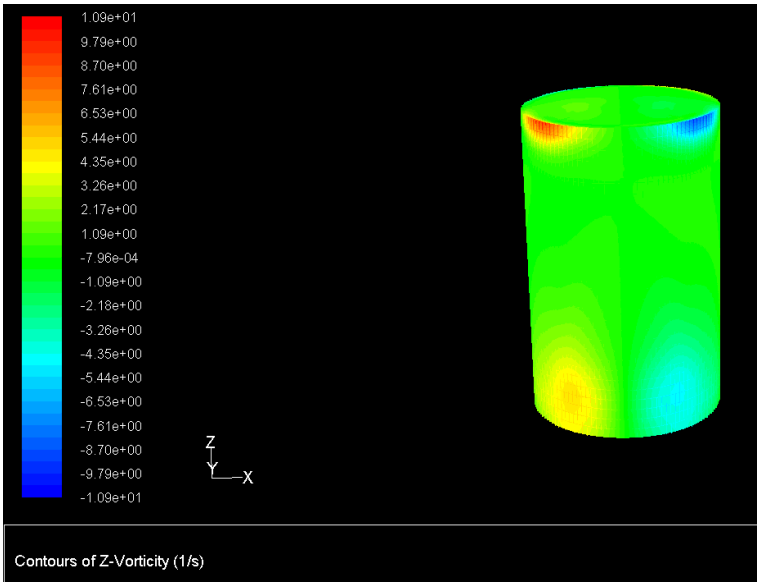

Figure 5.15: Vorticity obtained from the EM20 hollow blocks in the z-direction is less than those developed by the control ones.

Also, there is a significant change in temperature between the top and the bottom of the hollow blocks in general in along the height of the cavity as shown in Figure 15. This

temperature gradient is produced by the buoyancy forces between the rising flow at the hot isotherms and the descending flow at the cold ones. Hot air accumulates at the top cells while cold air accumulates at lower cells (Al-Hazmy, 2006).

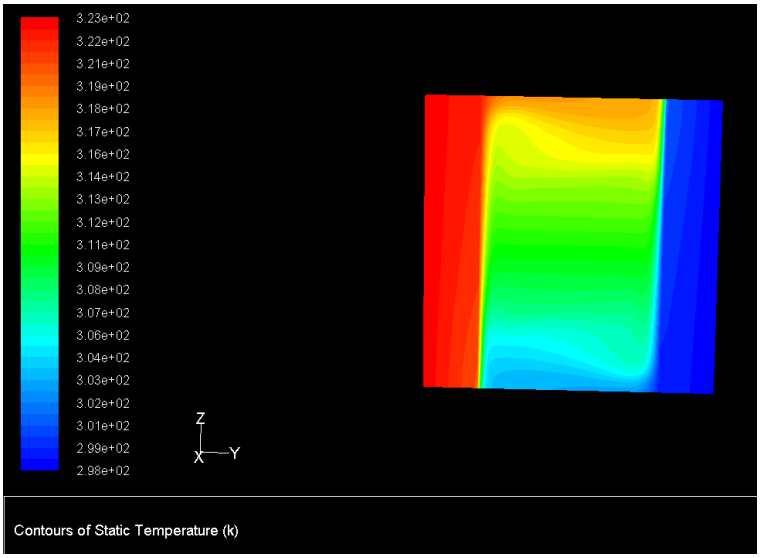

Figure 5.16: Temperature gradient along the height of the hollow blocks induced by buoyant forced circulating air.

It is difficult, therefore, to ignore of the effect of convection. The contribution of convection increases as the K-value of the solid phase decreases could be explained by the supposition that the weakness of the conduction mode and contribution let way to the amplification of the effect of convection. This amplification has a negative effect on the EM26 hollow blocks where the K_{eq} produced from the conduction-convection mode ($K_{cond-conv}$) is more than the K-value of the solid phase. Therefore these blocks are better off either solid or filled with convection suppressing core like polystyrene or wool.

5.5.3 The effect of radiation

The rate or radiation heat transfer Q_{rad} is slightly more than the effect of Q_{conv}, however, this effect rapidly decreases with the decrease in the K-value of solids (K_s) as illustrated in Figure 5.7. When radiation mode is introduced to the conduction-convection mode, the K_{tot} rapidly increases and the gap between K_s and K_{tot} is bridged significantly as shown in figure. Hollow blocks of mixes EM20 and EM26 are the most severely affected by considering radiation that

their K_{tot} is more than their K_s. The significant effect of radiation is acknowledged and cannot be disregarded for reason of engineering practicality (Sun and Fung, 2009).

The effect of radiation is dominant in enclosures (Balaji and Venkateshan, 1994; Baig, 2008; Sun and Fung, 2009). Radiation causes a drop in the convective component that is amplified in the presence of high emissivity (e>0.9) (Balaji and Venkateshan, 1994). The drop occurs because radiation exerts an equilibrating effect on the temperature of the walls of enclosures, thus reducing the temperature gradient that initiates air circulation (Balaji and Venkateshan, 1994).

The drop in convection makes way to the interaction between the conduction and radiation modes (Balaji and Venkateshan, 1994). This is seen in Figures 5.6 and 5.7 where the contribution of conduction diminishes with the decrease in the k-value of the solid phase. Figure 5.16 shows the drop in the cavity differential temperature due to the introduction of the radiation mode as compared to the conduction-convection mode.

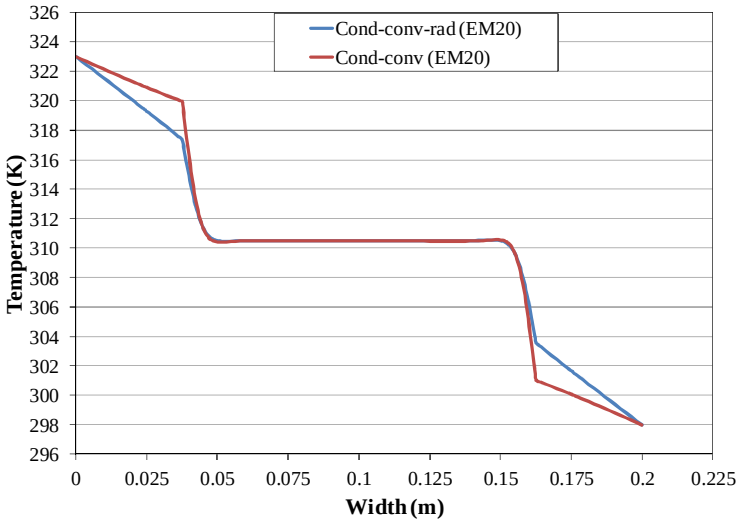

Figure 5.17: the effect of radiation mode on equilibrating the cavity wall temperature.

The factors that mainly affected the contribution of radiation are the emissivity and the cavity width (Baig, 2008; Sun and Fang 2009). Setting the emissivity of the EPS and conventional mortars equivalent might need further study and review. EPS is a highly insulating material that contains gas filled pores; its addition to concrete produces a composite that possesses

significantly improved low emissivity. EPS mortar of dry density equals to 458 kg/m^3 has a conduction-radiation equivalent K-value ($K_{cond-rad}$) of 0.137 W/mK which indicates a significantly low emissivity and therefore, low contribution in the radiation heat transfer mode (Bonacina et al, 2003 and Jelle et al, 2009).

The cavity width plays a major rule in contributing to the increase in Q_{rad}(Sun and Fang, 2009). Similar results of elevated contribution of K_{rad} were reported by Sun and Fang, 2009 and attributed to the cavity width and the presence of one cavity. Splitting the cavity through partitions into smaller cavities or lining the cavity walls with insulation would reduce the radiation effect (Sun and Fang, 2009, and Al-Hazmy, 2006).

Chapter 6

Summary and Conclusion

6.1 Summary

This research attested the viability of using EPS aggregates in casting hollow blocks and solid bricks as a viable thermally efficient building component. EPS particles were used as partial replacement of the fine aggregates. Four dosages of EPS were used mainly, 10, 15, 20, and 26 kg/m^3 partial substitution of the sand content in the mortar mixes. Experimental investigation was conducted to study the effect of the percentage of EPS on the properties of the EPS mortar. The different mixes of the EPS mortar were used to cast hollow blocks of dimensions 400x200x200 mm with two cylindrical holes of diameter 125mm and solid brick of dimensions 235x115x65 mm. The ferrocement concept was used to reinforce the hollow blocks with two types of reinforcing mesh mainly welded wire mesh and glass fiber mesh. Experimental tests were conducted on the developed hollow block and solid bricks to investigate the effect of the EPS content on the mechanical properties, durability, and thermal characteristics of the developed building units. The results showed that EPS mortar of density range 988 and 1748 kg/m^3 produced mechanical properties of EPS hollow blocks and solid bricks that comply with ASTM C 129 and the Egyptian standards. Moreover, the long-term cyclic exposure to abrasive environments revealed the resilience of the proposed building units. In addition, the experimental and numerical thermal analysis revealed good reduction trend in the thermal conductivity of the bricks and hollow blocks.

6.2 Conclusion

Based on the experimental results of the present investigation and within the limitations of the conducted experimental program, the following conclusion could be drawn:

- The use of EPS is effective in reducing the dry density of mortar mixes. The reduction in density is somewhat proportional to the increase in the content of EPS per mix.
- It is recommended to use a polymer admixture such as latex or polyvinyl acetate to improve bond between the mortar matrix and EPS aggregates in denser EPS mortar mixes such as EM10 and EM15.

- The compressive strength reduced from 14.2 to 3.5 MPa when the weight of EPS/m^3 of the mix was increased from 10 to 26 kg/m^3.

- Specimens incorporating EPS showed improved failure pattern as demonstrated by a gradual failure pattern until ultimate failure. All EPS mortar specimens displayed gradual failure retained their integrity after failure, unlike the control mortar mix which suffered from sudden and brittle failure.

- The static modulus of elasticity of EPS mortar mixes is reduced with the increase of the dosage of EPS. The static modulus of elasticity ranged between 8.2 and 1.2 GPa for mixes EM10 and EM26 respectively
- The compressive strength of the EPS mortar hollow blocks and solid bricks was highly affected by the content of EPS aggregates. The net compressive strength of the EPS mortar hollow blocks ranged between 6.9 and 2.4 MPa with a corresponding weight range between 19.5 and 10.6 kg. The control hollow blocks had compressive strength of 9.5 MPa and weighed 23.5 kg
- The strength of the EPS mortar solid bricks ranged between 5.9 and 2.2 MPa with a corresponding weight ranged between 2.9 and 1.7 kg. The control solid bricks had compressive strength of 8.6 MPa and weighed 3.8 kg.
- The reinforcement inside EPS mortar hollow blocks did not transform their compressive strength from the non-load bearing category to the load bearing category.
- The wire mesh and GFRP reinforcement positively affected the characteristics of the hollow EPS mortar blocks by generating more gradual failure and specimens retained their integrity.
- The compressive strength of ferrocement dense EPS hollow blocks (EM10) was almost equivalent to that of the plain but significantly higher than that of the GFRP mesh reinforced EPS hollow blocks.
- A good utilization of the wire mesh reinforcement was recorded by lighter EPS mortar hollow blocks (EM15 1nd EM20) where the compressive strength was higher than that obtained by their plain and GFRP reinforced counterparts.

- The dosage of the EPS aggregates exerted unsubstantial effect on absorption that rendered a near constant average absorption value of 4 % recorded by almost all the EPS mortar hollow blocks.
- The wet-dry cyclic exposure to 5% of sulfuric acid dilute unveiled that the strength loss was not affected by either the density of the block or the EPS content, except for a few outliers. The strength loss for all the hollow blocks ranged between 15 and 30 percent.
- The wet-dry cyclic exposure to saturated saline solution had adversely affected the plain and reinforced EPS hollow blocks in different physical and chemical reactions. All hollow blocks suffered from weight retention after drying cycles which resulted from prolonged drying and salt precipitation.
- Plain hollow blocks suffer from efflorescence and micro-cracking due to salt crystallization. The compressive strength loss ranged between 6.11 % and 26.67%.
- The addition of EPS decreased the strength deterioration and weight loss of the plain hollow blocks when subjected to 5% sulphuric acid wet/dry cycles.
- The addition of EPS decreased the strength deterioration of the plain hollow blocks when subjected to saline wet/dry cycles.
- All ferrocement hollow blocks are the least affected by saline cycles except for the densest and the lightest batches of hollow blocks.
- The GFRP mesh reinforced hollow block suffers the most from saline wet-dry cycles due to the GFRP fiber deterioration by the cyclic exposure to moisture. The GFRP mesh failure set the ultimate strength and triggered the failure of denser EPS hollow blocks.
- Incorporating EPS improves the thermal insulation properties of the mix. The coefficient of thermal conductivity (K-value) is decreased with the increase of EPS content in the mix**.**
- The lowest thermal conductivity was reported for the EM20 and EM26 bricks which recorded 0.56 W/m K and 0.16 W/m K respectively, compared with 1.8 W/m K for the control mix.
- The lowest total equivalent thermal conductivity—considering the three heat transfer modes: conduction, convection and radiation—was recorded for the lighter EPS mortar hollow blocks at range of 0.63W/m K and 0.25 W/m K.

- The of radiation in the numerical model showed that lighter EPS mortar hollow blocks (from mixes EM20 and EM26) had more equivalent thermal conductivity than if they had solid geometry.
- Denser EPS hollow blocks (mixes EM10 and EM15) are recommended for non-load bearing external wall applications.
- Lighter EPS hollow blocks (from mixes EM20 and EM26) are recommended for non-load bearing external wall applications in very hot climates because of their higher thermal insulation, especially in high rise and office buildings where dead load and energy consumption reductions are appreciated.
- Lighter EPS hollow blocks, especially reinforced ones, are recommended for non-load bearing external wall applications where dynamic load exists, however, the construction method needs to be designed with care--flexible mortar joints and shear reinforcement should be designed accordingly.
- Reinforced EPS hollow blocks, especially the ferrocement ones, are recommended for applications where dynamic load--e.g. earthquakes--is considered because of the block's capacity to develop narrower cracks and tougher response.
- EPS hollow blocks would be suitable as salvage walls in foundation lining where salts and/or abrasive soils--sulphur presence from ground water or sewage leak--is a fret.

6.3 Recommendations for future work

- The rheology of the EPS mixes should be studied and adjusted according to different factors such as: 1-volume of the mix, 2-volume of the mixer, 3-bouyancy forces exerted by the mortar, 4-surface tension between the EPS aggregate and the mortar, 5-mixing method and time and 6-casting method and time. The consistency of the mix could be enhanced by adding polyvinyl acetate emulsion, latex or any other bond enhancing admixture.

- Study the effect of higher percentages of silica fume and fly ash would increase the durability of EPS mortars. The strength of the EPS mortar mix could be improved by using beaded spheres of much smaller size.
- Study the effect of EPS aggregate size, gradation and quality on the compressive strength of EPS mortar mixes experimentally and numerically.

- Assessing the thermal characteristics of EPS mortars is just at its initial stages, hence parameters are needed to be experimentally assessed such as specific heat capacity, emissivity, moisture transmissivity and micro porosity and macro porosity.
- EPS mortar should be subjected to pyrolysis test-fire degradation-to estimate the temperature at which it starts degrading and the volume of toxic fumes released during thermal degradation.

6.4 Recommendations for applications

- The compressive strength of the EPS hollow blocks would rather be put in context in future research through testing prisms and real size walls. The interaction between the stronger mortar joints confining the more ductile ferrocement EPS mortar hollow blocks is worth assessing and studying.

- The construction method of EPS hollow block walls in terms of type and design of mortar joint and the presence of shear reinforcement and expansion joints should be explored to maintain the structures' low thermal conductivity--reduce thermal bridges--and toughness.
- Finite element modeling was proved a utile tool in this research. Since nearly all the mechanical and thermal properties of EPS mortar were explored in this research, FEM of real size walls should be embarked on as the next step in research to explore compressive, dynamic and impact strength of structures made from the proposed building units.
- Researching the transient thermal transmissivity of the EPS mortar hollow blocks wall would certainly mark their advantages in terms of thermal mass and the factors affecting the thermal performance of walls subjected to a simulation of real environmental conditions.
- Walls made from plain and reinforced EPS hollow blocks—filled and cored—should be tested against impact load. As one of the main attraction of EPS mortars is its gradual failure and higher toughness.
- EPS cement blocks should be tested and rated against fire exposure with the presence and absence of fire retardant inside their cavities. Counteractive measures and special fire retarding plaster should be also considered and tested to overcome any toxic emissions.

References

ACI Committee 201.2R. *Guide to Durable Concrete.* Technical Report, Farmington Hills, IL: American Concrete Institute, 2006.

ACI Committee 530-08. *Building code requirements for masonry structures.* Technical Report, Farmington Hills, IL: American Concrete Institute, 2006.

ACI Committee 549. *Guide for the Design, Construction & Repair of Ferrocement* . Technical Report, Detroit : American Concrete Institute, 1988.

Aitcin, P. C. *High-Performance Concrete.* London: E & FN Spon, 1998.

Ait-Taleb, T., A. Abdelbaki, and Z. Zrikem. "Numerical simulation of coupled heat transfers by conduction, natural convection and radiation in hollow structures heated from below or above." *International Journal of Thermal Sciences*, 2008: 378-387.

Albikary, Abdel-latif Abou El Atta. *The engineering encyclopedia for building construction and public utilities: Part 1(in Arabic).* Cairo, Egypt: Dar Misr for Publishing, 2003, 6th Ed.

Al-Hadhrami, Luai M., and A. Ahmad. "Assessment of thermal performance of different types of masonry bricks used in Saudi Arabia." *Applied Thermal Engineering*, 2009: 1123–1130.

Al-Hazmy, Majed. "Analysis of coupled natural convection-conduction effects on the heat transport through hollow building blocks." *Energy and Buildings* , 2006: 515-521.

Al-Jabri, K. S., A. W. Hago, A. S. Al-Nuaimi, and A. H. Al-Saidy. "Concrete blocks for thermal insulation in hot climate." *Cement and Concrete Research* , 2005: 1472– 1479.

Almusallam, Tarek H., and Yousef A. Al-Salloum. "Durability of GFRP rebars in concrete beams under sustained loads at severe environments." *Journal of Composite Materials*, 2006: 623-637.

ASTM C 496 – 96. *Standard Test Method for Splitting Tensile Strength of Cylindrical Concrete Specimens.* Standard, West Conshohocken, PA: ASTM International, 1996.

ASTM C1012/C1012M – 10. *Standard Test Method for Length Change of Hydraulic-Cement Mortars Exposed to a Sulfate Solution.* Standard, West Conshohocken, Pennsylvania: ASTM International, 2010.

ASTM C1113/C1113M – 09. *Standard Test Method for Thermal Conductivity of Refractories by Hot Wire (Platinum Resistance Thermometer Technique).* Standard, West Conshohocken, Pennsylvania: ASTM International, 2009.

ASTM C129 – 06. *Standard Specification for Nonloadbearing Concrete Masonry Units.* Standard, West Conshohocken, Pennsylvania: ASTM International, 2007.

ASTM C1314 . *Standard Test Method for Compressive Strength of Masonry Prisms.* Standard, West Conshohocken, Pennsylvania: ASTM International, 2010.

ASTM C140 – 09a. *Standard Test Methods for Sampling and Testing Concrete Masonry Units and Related Units.* Standard, West Conshohocken, Pennsylvania: ASTM International, 2009.

ASTM C1552 – 09a. *Standard Practice for Capping Concrete Masonry Units, Related Units and Masonry Prisms for Compression Testing1.* Standard, West Conshohocken, Pennsylvania: ASTM International, 2009.

ASTM C39/C39M – 11a. *Standard Test Method for Compressive Strength of Cylindrical Concrete Specimens.* Standard, West Conshohocken, PA: ASTM International, 2010.

ASTM C469 – 02. *Standard Test Method for Static Modulus of Elasticity and Poisson's Ratio of Concrete in Compression.* Standard, West Conshohocken, Pennsylvania: ASTM International, 2002.

ASTM C642 – 06. *Standard Test Method for Density, Absorption, and Voids in Hardened Concrete.* Standard, West Conshohocken, Pennsylvania: ASTM International, 2006.

ASTM C90 – 11. *Standard Specification for Loadbearing Concrete Masonry Units.* Standard, West Conshohocken, Pennsylvania: ASTM International, 2011.

Babu, Daneti Saradhi, K. Ganesh Babu, and Wee Tiong-Huan. "Effect of polystyrene aggregate size on strength and moisture migration characteristics of lightweight concrete." *Cement & Concrete Composites*, 2006: 520-527.

Babu, K. Ganesh, and D. Saradhi Babu. "Behaviour of lightweight expanded polystyrene concrete containing silica fume." *Cement and Concrete Research*, 2003: 755-762.

Baig, Hassan. *Numerical analysis of conjugate conduction-natural convection in a hollow building block.* MSc. Thesis, KING FAHD UNIVERSITY OF PETROLEUM & MINERALS, May 2008.

Balaji, C., and S. P. Venkateshan. "Interaction of surface radiation with free convection in a square cavity." *Int. J. Heat and Fluid Flow*, 1993: 260-267.

Barakos, G., and E. Mitsoulis. "natural convection flow in a square cavity revised: laminar and turbulent models with wall functions." *International Journal for Numerical Methods in Fluids*, 1994: 695-719.

Bastgen, K. J., and V. Hermann. "Experience made in determining the static modulus of elasticity of concrete." *Matériaux et constructions*, 1977: 357-364.

Bazant, Zdenek P., Josko Ozbolt, and Rolf Eligehausen. "Fracture size effect: review of evidence for concrete structures." *Journal of Structural Engineering*, 1994: 2377-2398.

Bischoff, B. H., K. Yamura, and S. H. Perry. "Polystyrene aggregate concrete subjected to hard impact." *Proceedings of the Institution of Civil Engineers, Part2: Dsign and Construction.* Institution of Civil Engineers (Great Britain), 1990. 225-239.

Bisschop, Jan, and Jan G.M. van Mier. "Effect of aggregates and microcracks on the drying rate of cementitious composites." *Cement and Concrete Research*, 2008: 1190–1196.

Bonacina, C., M. Campanale, and L. Moro. "Analytical and experimental investigations on the heat transfer properties of light concrete." *International Journal of Thermophysics*, 2003: 1407-1414.

Bouvard, D., et al. "Characterization and simulation of microstructure and properties of EPS lightweight concrete." *Cement and Concrete Research*, 2007: 1666-1673.

BS 8110: 1997. *Structural use of concrete Part 1: Code of practice for design and construction.* Standard, London: British Standards Institution, 1997.

Carpinteri, Alberto, Francesco Ciola, and Nicola Pugno. "Boundary element method for the strain-softening response of quasi-brittle materials in compression." *Computers and Structures*, 2001 : 389-401.

Cellular Concrete INC. *Masonry*. 2007-2011. http://www.cellularconcreteinc.com/Masonry.html (accessed 5 January, 2011).

Ceroni, Francesca, Edoardo Cosenza, Manfredi Gaetano, and Marisa Pecce. "Durability issues of FRP rebars in reinforced concrete members." *Cement & Concrete Composites* , 2006 : 857–868.

Ceroni, Francesca, Edoardo Cosenza, Manfredi Gaetano, and Marisa Pecce. "Durability issues of FRP rebars in reinforced concrete members." *Cement & Concrete Composites* , 2006: 857–868.

Chandra, Satish, and Leif Berntsson. "Durability of Lightweight Aggregate Concrete to Chemical Attack." *Lightweight aggregate concrete*, 2002: 231-289.

Chen, Bing, and Juanyu Liu. "Mechanical properties of polymer-modified concretes containing expanded polystyrene beads." *Construction and Building Materials*, 2007: 7–11.

Chen, Bing, and Juanyu Liu. "Properties of lightweight expanded polystyrene concrete reinforced with steel fiber." *Cement and Concrete Research* , 2004: 1259–1263.

Chen, Yi, Julio F. Davalos, Indrajit Ray, and Hyeong-Yeol Kim. "Accelerated aging tests for evaluations of durability performance of FRP reinforcing bars for concrete structures." *Composite Structures*, 2007: 101–111.

Dawood, ET, and M. Ramli. "Hollow block concrete unit production using super-plasticizer and pumicite." *Australian Journal of Civil Engineering*, 2010: 35-46.

De Vahl Davis, G. "Natural convection of air in a square cavity a bench mark numerical solution ." *International Journal for Numerical Methods in Fluids*, 1983: 249-264.

del Coz Diaz, J. J., P. J. Garcia Nieto, J. L. Suarez Sierra, and C. Betegon Biempica. "Nonlinear thermal optimization of external light concrete multi-holed brick walls by the finite element method." *International Journal of Heat and Mass Transfer*, April, 2008: 1530-1541.

del Coz Diaz, J.J., P. J, Garcia Nieto, J. L. Suarez Sierra, and I. Penuelas Sanchez. "Non-linear thermal optimization and design improvement of a new internal light concrete multi-holed brick walls by FEM." *Applied Thermal Engineering*, June, 2008: 1090-1100.

dos Santos, Wilson Nunes. "Effect of moisture and porosity on the thermal properties of a conventional refractory concrete." *Journal of the European Ceramic Society*, 2003 : 745–755.

EOS 2005/42 . *Standards for solid bricks and hollow blocks (in Arabic)* *الطوب والبلوكات الرملية الجيرية الطوب المصمت والطوب المثقب والبلوكات المصمته والبلوكات المجوفة*. Standard, Cairo, Egypt: Egyptian Organization for Standardization and Quality, 2005.

Fattuhi, N. I., and B. P. Hughes. "The performance of cement paste and concrete subjected to sulphuric acid attack." *Cement and Concrete Research*, 1988: 545-553.

Fusegi, T., J. M. Hyun, K. Kuwahara, and B. Farouk. "A numerical study of three-dimensional natural convection in differentially heated cubical enclosure." *Int. J Heat Mass Transfer*, 1991: 1543-1557.

Gaafar, Hassan Mohammed. *Ferrocement sandwich and hollow core panels for floor and wall construction.* MSc. Thesis, Cairo, Egypt: The American University in Cairo, 2004.

Gaggino, Rosana. "Light and insulant plates for housing external closure." *Construction and Building Materials*, 2006: 917–928.

Godwin, Alan. "Versatile concrete block for the third world." *The Indian concrete journal*, 1982: 240-241.

Gunduz, L. "Use of quartet blends containing fly ash, scoria, perlitic pumice and cement to produce cellular hollow lightweight masonry blocks for non-load bearing walls." *Construction and Building Materials* , 2008: 747–754.

Hago, A. W., K. Al-Jabri, A. Al-Harithi, and M. QAMARUDDIN. "Development of lightweight concrete blocks for thermal insulation." *Proceedings 9 of the British Masonary Society.* International Masonary Society, 2002. 213-216.

Hago, A. W., K. S. Al-Jabri, A. S. Al-Nuaimi, and A. H. Al-Saidy. "Comparison between different lightweight blocks for thermal insulation." *Progress in Structural Engineering, Mechanics and Computation.* Cape Town, South Africa: Taylor & Francis, 2004. 1475-1478.

Haidar, Khalil, and Gilles Pijaudier-Cabot. "Influence of porosity on fracture characteristics in mortar structures." *15th ASCE Engineering Mechanics Conference.* Columbia University, New York, NY: ASCE, 2002. 1-8.

Incropera, Frank P., and David P. DeWitt. *Fundamentals of heat and mass transfer, 4th edition.* New York: John Wiley & Sons, Inc., 1996.

Johnston, Colin D., and Samir G. Mattar. "Ferrocement-behavior in tension and compresion." *Journal of the Structural Division*, 1976: 875-889.

Kan, Abdulkadir, and Ramazan Demirboga. "A new technique of processing for waste-expanded polystyrene foams as aggregates." *journal of materials processing technology*, 2 0 0 9: 2994–3000.

Kannan, Pravin, Joseph J. Biernacki, and Donald P. Visco Jr. "A review of physical and kinetic models of thermal degradation of expanded polystyrene foam and their application to the lost foam casting process." *J. Anal. Appl. Pyrolysis* , 2007 : 162–171 .

Kanos, A., A.E. Giannakopoulos, and P.C. Perdikaris. "Size effect on concrete splitting tesnile strength and modulus of elasticity." *Measuring, Monitoring and Modeling Concrete Properties*, 2006: 239–246.

Karbhari, V. M., K. Murphy, and S. Zhang. "Effect of Concrete Based Alkali Solutions on Short-Term Durability of E-Glass/Vinylester Composites." *Journal of Composite Materials* , 2002 : 2101-2121.

Khatib, Jamal M. *Sustainability of construction materials.* Oxford: Woodhead Publishing Limited, 2009.

Kligys, M., A. Laukaitis, M. Sinica, G. Sezemanas, and N. Dranseika. "Investigations into the fire hazard of a composite made from aerated concrete and crushed expanded polystyrene waste." *Mechanics of Composite Materials*, 2008: 173-180.

Kluge, Ralph W., Morris M. Sparks, and Edward C. Tuma. "Lightweight-Aggregate Concrete." *Journal of the American Institute*, 1949: 625-642.

Koleva, D.A., J. Hu, A.L.A. Fraaij, K. van Breugel, and J.H.W. de Wit. "Microstructural analysis of plain and reinforced mortars under chloride-induced deterioration." *Cement and Concrete Research*, 2007: 604–617.

Kondraivendhan, B., and Bulu Pradhan. "Effect of ferrocement confinement on behavior of concrete." *Construction and Building Materials* , 2009: 1218–1222.

Koniorczyk, Marcin. "Modelling the phase change of salt dissolved in pore water – Equilibrium and non-equilibrium approach." *Construction and Building Materials* , 2010 : 1119–1128.

Koniorczyk, Marcin, and Dariusz Gawin. "Heat and Moisture Transport in Porous Building Materials Containing Salt." *Journal of Building Physics* , 2008 : 279-300.

Kumar, P. Rathish, and C. B. K. Rao. "Constitutive behaviour of high-performance ferrocement under axial compression." *Magazine of concrete research*, 2006: 647-656.

Kumar, P., and V. Eswaran. "A Numerical Simulation of Combined Radiation and Natural Convection in a Differential Heated Cubic Cavity." *Journal of Heat Transfer*, 2010: 1-13.

Laboratories), USACERL (U.S. Army Construction Engineering Research. *Development of high-performance lightweight concrete masonry units.* TR 97/84, Champaign, IL: U.S. Army Corps of Engineers, 1997.

Laukaitis, A., R. Zarauskas, and J. Keriene. "The effect of foam polystyrene granules on cement composite properties." *Cement & Concrete Composits*, 2005: 41-47.

Lubelli, Barbara, and Mario R. de Rooij. "NaCl crystallization in restoration plasters." *Construction and Building Materials*, 2009 : 1736–1742.

Mansur, M. A., Mohamed Maalej, and Mohammad Ismail. "Study on Corrosion Durability of Ferrocement." *ACI MATERIALS JOURNAL*, 2008: 28-34.

Marshall, A. L. "The thermal properties of concrete." *Building Science*, 1972: 167-174.

McNary, Scott, and Daniel P. Abrams. "Mechanics of masonry in compression." *Journal of Structural Engineering*, 1985: 857-870.

Memon, Noor Ahmed, Salihuddin Radin Sumadi, and Mahyuddin Ramli. "Ferrocement encased lightweight aerated concrete: A novel approach to produce sandwich composite." *Materials Letters* , 2007: 4035–4038.

Memon, Noor Ahmed, Salihuddin Radin Sumadi, and Mahyuddin Ramli. "Ferrocement encased lightweight aerated concrete: A novel approach to produce sandwich composite." *Materials Letters* , 2007: 4035–4038.

Memon, Noor Ahmed, Salihuddin Radin Sumadi, and Mahyuddin Ramli. "Strength and behavior of lightweight ferrocement-aerated concrete sandwich blocks." *Malaysian Journal of Civil Engineering* , 2006: 99-108.

Memon, Noor Ahmed, Salihuddin Radin Sumadi, and Mahyuddin Ramli. "Strengthening and behaviour of lightweight ferrocement aerated concrete sandwich blocks." *Malaysian Journal of Civil Engineering* , 2006: 99-108 .

Miled, K., K. Sab, and R. Le Roy. "Particle size effect on EPS lightweight concrete compressive strength: Experimental investigation and modelling." *Mechanics of Materials*, 2007: 222-240.

Miled, R., R. Le Roy, K. Sab, and C. Boulay. "Compressive behavior of an idealized EPS lightweight concrete: size effects and failure mode." *Mechanics of Materials*, 2004: 1031-1046.

Mosalam, K., L. Glascoe, and J. Bernier. *Mechanical properties of unreinforced brick masonry, section 1*. LLNL-417646, Livermore, California: U.S. Department of Energy by Lawrence Livermore National Laboratory, 2009.

Nambiar, E. K. Kunhanandan, and K. Ramamurthy. "Models relating mixture composition to the density and strength of foam concrete using response surface methodology." *Cement & Concrete Composites*, 2006: 752-760.

Neville, M.N. *Properties of Concrete.* London: Pitman Publishing Limited, 1981.

Perry, S. H., P. H. Bischoff, and K. Yamura. "Mix details and material behaviour of polystyrene aggregate concrete." *Magazine of Concrete Research*, 1991: 71-76.

Petter, Jelle Bjørn, Arild Gustavsen, and Ruben Baet. "The path to the high performance thermal building insulation materials and solutions of tomorrow." *Journal of Building Physics*, 2010: 99–123.

Poon, Chi Sun, Lik Lam, and Yuk Lung Wong. "Effects of fly ash and silica fume on interfacial porosity of concrete." *JOURNAL OF MATERIALS IN CIVIL ENGINEERING*, 1999: 197-205.

Portland Cement Association (PCA). *Concrete Masonry Units.* http://www.cement.org/masonry/block.asp (accessed 5 January, 2011).

Ramamurthy, K., E. K. Kunhanandan Nambiar, and G. Indu Siva Ranjani. "A classification of studies of properties of foam concrete." *Cement & Concrete Composites*, 2009: 388-396.

Ravindrarajah, R. Sri, and A. J. Truck. "Properties of Hardened Concrete Containing Treated Expanded Polystyrene Beads." *Cement and Concrete Composites*, 1994: 273-277.

RILEM TC148-SSC. "Strain-softening of concrete in uniaxial compression." *Materials and Structures*, 1997: 195-209.

Sabaa, Ben, and Rasiah Sri Ravindrarajah. "Engineering properties of lightweight concrete containing crushed expanded polystyrene waste." *Symposium MM: Advances in Materials for Cementitious Composites.* Boston, USA: Materials Research Society, 1997 Fall Meeting, 1997. 1-11.

Shannag, M. Jamal. "Bending behavior of ferrocement plates in sodium and magnesium sulfates solutions." *Cement & Concrete Composites* , 2008: 597–602.

Song, Ha-Won, Chang-Hong Lee, and Ki Yong Ann. "Factors influencing chloride transport in concrete structures exposed to marine environments." *Cement & Concrete Composites* , 2008 : 113–121.

Song, Ha-Won, Seung-Woo Pack, Sang-Hyeok Nam, Jong-Chul Jang, and Velu Saraswathy. "Estimation of the permeability of silica fume cement concrete ." *Construction and Building Materials* , 2010 : 315–321.

Spragg, Robert P., Javier Castro, Wenting Li, Mohammad Pour-Ghaz, Pao-Tsung Huang, and Jason Weiss. "Wetting and drying of concrete using aqueous solutions containing deicing salts." *Cement & Concrete Composites*, 2011: 535 - 542.

Sun, Jiapeng, and Liang Fang. "Numerical simulation of concrete hollow bricks by the finite volume method." *International Journal of Heat and Mass Transfer*, 2009: 5598-5607.

Tang, W. C., Y. Lo, and A. Nadeem. "Mechanical and drying shrinkage properties of structural-graded polystyrene aggregate concrete." *Cement & Concrete Composites*, 2008: 403-409.

Trussoni, Matthew. *Fracture properties of concrete mixtures containing expended polystyrene aggregate replacement.* Florida, USA: PhD. Thesis Dissertation, University of University of Miami, 2009.

Valore, Jr., Rudolph C. "Cellular Concretes Part 1: Composition and Methods of Preparation." *American Concrete Institute*, 1954: 773-796.

VanGreen, M. G. "Thermal transmittance of concrete block walls with core insulation." *Journal of Thermal Insulation*, 1986: 187-210.

Vonk, R. A. "A micromechanical investigation of softening of cconcrete loaded in compression." *HERON*, 1993: 1-94.